

Numerical Study on Droplet Evaporation and Combustion Instability

Tomoaki Kitano

Numerical Study on Droplet Evaporation and Combustion Instability

Tomoaki Kitano

A thesis submitted to Kyoto University
for the degree of Doctor of Philosophy in Engineering

2016

Acknowledgments

The research described in this thesis was carried out in the Department of Mechanical Engineering and Science at Kyoto University Graduate School of Engineering, under the supervision of Professor Satoru Komori. The author would like to express his most heartfelt gratitude to the professor for all the helpful suggestions to his study, and constant encouragement.

The author gives his thanks to Professor Takaji Inamuro and Professor Kazuyoshi Nakabe for many valuable and critical comments to his study.

The author shows his appreciation to Professor Ryoichi Kurose from the bottom of his heart for many useful discussions and comments to his research, and for the top-notch education.

The author is deeply grateful to Dr. Masaya Muto for the helpful discussions and suggestions for his study, and encouragement.

The author thanks Dr. Naohisa Takagaki for the many useful comments to his research.

The author is grateful to Dr. Shigeru Tachibana of Japan Aerospace Exploration Agency (JAXA) for many useful discussions.

The author thanks Dr. Akitoshi Fujita, Dr. Keigo Matsuda, Mr. Tomoaki Nakatani, Mr. Yutaka Yano, Mr. Takafumi Tsuji, Mr. Masato Hayashi, Mr. Jun Nishio, Mr. Takumi Hara, Mr. Yu Okuyama, and Mr. Keisuke Kaneko for their help in his research. The author feels gratitude to Dr. Koji Iwano and the past and present members of Environmental Fluids and Thermal Engineering Laboratory.

The author thanks Dr. Huilai Zhang of Numerical Flow Designing Co., Ltd (NuFD)

for his useful advice in developing the computational code.

This study was supported in part by “Strategic Programs for Innovative Research (SPIRE) Field No. 4: Industrial Innovations” from the Ministry of Education, Culture, Sports, Science and Technology (MEXT) using the K computer at RIKEN Advanced Institute for Computational Science (Project ID: hp130018), and Japan Society for the Promotion of Science (JSPS) Grant-in-Aid for JSPS Fellows (Grant No. 26·1137). The author would like to acknowledge the support and the financial aid from JSPS.

Finally, the author would like to express the deepest appreciation to his parents for the infinite support and constant affection.

Contents

1	Introduction	1
1.1	Background and purpose of this study	1
1.2	Thesis outline	5
	References	6
2	DNS of droplet evaporation and combustion	11
2.1	Introduction	11
2.2	Single-component fuel droplet	13
2.2.1	Numerical Simulation	13
2.2.1.1	Governing equations	13
2.2.1.2	Evaporation model	15
2.2.1.3	Saturated vapor pressure	16
2.2.1.4	Reaction model	18
2.2.1.5	Computational details	18
2.2.2	Results and discussion	23
2.2.2.1	Single fuel droplet without combustion	23
2.2.2.2	Multiple fuel droplets without combustion	25
2.2.2.3	Multiple fuel droplets with combustion	35
2.3	Multi-component fuel droplet	46
2.3.1	Numerical Simulation	46
2.3.1.1	Evaporation model	46
2.3.1.2	Reaction model	48

2.3.1.3	Computational details	48
2.3.2	Results and discussion	50
2.3.2.1	Single fuel droplet without combustion	50
2.3.2.2	Multiple fuel droplets without combustion	50
2.3.2.3	Multiple fuel droplets with combustion	54
2.4	Conclusions	59
	References	61
3	LES of combustion instability in a back-step flow	67
3.1	Introduction	67
3.2	Gas combustion	69
3.2.1	Numerical Simulation	69
3.2.1.1	Governing equations	69
3.2.1.2	Reaction model	70
3.2.1.3	Computational details	76
3.2.2	Results and Discussion	76
3.2.2.1	Feature of combustion instability	76
3.2.2.2	Mechanism of combustion instability	77
3.3	Spray combustion	81
3.3.1	Numerical Simulation	81
3.3.1.1	Governing equations	81
3.3.1.2	Reaction model	85
3.3.1.3	Computational details	86
3.3.2	Results and discussion	91
3.3.2.1	Feature of combustion instability	91
3.3.2.2	Mechanism of combustion instability	91
3.3.2.3	Effect of initial droplet diameter	93
3.4	Conclusions	100
	References	101

4	DNS of flashback in a channel flow	105
4.1	Introduction	105
4.2	Numerical simulation	107
4.2.1	Governing equations	107
4.2.2	Reaction model	107
4.2.3	Computational details	107
4.3	Results and discussion	111
4.3.1	Effect of a pressure oscillation	111
4.3.2	Interaction of flame with turbulent flow structure	116
4.4	Conclusions	124
	References	125
5	Conclusions	129
5.1	Summary and conclusions	129
5.2	Suggestions for future research	132

Chapter 1

Introduction

1.1 Background and purpose of this study

Gas turbines are a type of internal combustion engine that are used for power generation and aircraft propulsion. Recently, energy security and environmental protection worries have driven the development of gas turbines with higher efficiencies and lower emissions. Pollution legislation pertaining to emissions from gas turbines, such as NO_x and soot, has tightened year by year. For instance, the International Civil Aviation Organization (ICAO) set a goal of NO_x emissions from jet engines in 2026 to 40% of the amount of NO_x emitted in 2010 [1].

Lean-burning gas turbines have been widely developed to meet such emissions regulations. Lean combustion decreases the emissions of NO_x and soot because of the lower combustion temperature, which simultaneously, increases the risk of combustion instability. Combustion instability is a self-excited, large-amplitude oscillation of a combustor or a flame that is caused by interactions between pressure oscillations, turbulence, and heat release that are caused by the combustion process. The combustion instability enhances the heat flux and thermal stress at the wall of the combustor, and sometimes the oscillation of the combustor causes low- or high-frequency fatigues. Therefore, the precise prediction and control of combustion instability are essential, and a number of studies have been performed. However, many issues remain unresolved and even the

mechanism of the combustion instability has not yet been well clarified [2–4]. In particular, combustion instability in spray combustion, which uses a liquid fuel, is hardly understood [5]. This is because spray combustion is a complex phenomenon that involves the interactions of a number of simultaneous processes, namely, the dispersion, evaporation, and combustion of the liquid fuel with the oxidizer [6–10].

The studies of combustion instability have been mainly performed experimentally [5, 11, 12]. However, because the number of measurable data is limited, it is difficult to investigate the detailed mechanism by experiments alone. Recently, the enhancement of computer performance has meant that numerical simulations have become major tools for studying fluid dynamics. High-performance computers (such as “K” computer) are now able to perform three-dimensional numerical simulations of spray combustion [13–15].

For numerical simulations of flow fields, three types of methods are used: direct numerical simulation (DNS), Reynolds-averaged Navier–Stokes (RANS) simulation, and large-eddy simulation (LES). DNS does not employ a turbulence model and makes it possible to investigate the underlying physics in detail. However, DNS requires huge computational effort to resolve the minimum scale of eddies [16–18]. This large computational cost limits the size of the computational domain and makes it difficult to use DNS for the study of combustion instability, which requires solving for a large domain that includes the inlet duct and exhaust outlet. Conversely, RANS simulations can simulate large domains at low computational cost by using large computational grids. Although widely used to support the development of industrial devices such as gas turbines, the accuracy of RANS simulations strongly depends on the turbulence model and is relatively poor at describing fields with strong recirculating flows. It is difficult to use RANS simulations to investigate combustion instability because investigating the phenomenon involves the precise prediction of flow fields that include recirculation. LES employs a turbulence model that is basically established based on the theory of scaling law of turbulence without fitting parameters and makes it possible to perform simulations for relatively large domains with a higher accuracy than RANS simulations. Therefore LES

have been used in recent studies for combustion instability.

For calculating of chemical reactions, a number of numerical methods have also been proposed. The detailed reaction model is the most accurate of the methods as it solves a large number of elementary reactions including radical reactions. For instance, the combustion of kerosene (which is often used as a fuel in gas turbines) includes over one hundred chemical species and around one thousand elementary reactions. Therefore, the computational cost is extremely high and it is impossible to use the detailed reaction model for the large computational domains. To decrease the computational cost, reduced reaction models, of which the simplest are one- or two-step global reaction models, have been proposed in many researches. These models are often used in DNS, RANS simulations, and LES, and are developed by fitting parameters to predict flame characteristics such as the laminar burning velocity and flame temperature. A turbulent reaction model is also used in LES and RANS simulations to incorporate the effects of sub-grid scale turbulence on reactions. The Flamelet model proposed by Peters [19, 20] is often used for non-premixed combustion, and the validity has been assessed in many previous studies [10, 13, 21, 22]. For premixed combustion, the artificially thickened flame model [23] has been widely used and validated [24–26].

In addition to calculating a flow field and reactions, motion of evaporating fuel droplets needs to be solved in spray combustion. Droplet evaporation is one of the most important factors that affect spray combustion. Miller et al. [27] examined the validity of various evaporation models by comparing their results with those obtained from experimental measurements of the evaporation of a single droplet. Miller and Bellan [28] also performed DNS and discussed the effects of the initial liquid mass loading ratio, the initial Stokes number, and the initial droplet temperature on the evaporation behavior of a droplet in a turbulent mixing layer. However, the evaporation conditions were limited in this study, and the effects of other important conditions such as ambient pressure and a difference in fuel components were not discussed.

Regarding the combustion instability, many numerical studies have been carried out for gas combustion. Sato et al. [29] performed LES of combustion instability caused

by an acoustically forced inlet flow. They compared the LES results with experimentally measured data and showed that the LES was able to predict the flame response to the forcing. Wolf et al. [30] numerically analyzed combustion instability in an annular combustion chamber by using LES and an acoustic solver. They showed that the LES was able to predict an azimuthal mode of the combustion instability. Moreover, it was suggested that a reduction of the time delay of the flame transfer function stabilized the mode. Franzelli et al. [26] developed a two-step global reaction model of methane combustion that precisely predicts the flame temperature and laminar burning velocity under various conditions. By using the reaction model, they performed LES of combustion instability in a laboratory-scale combustor and investigated the effects of mixing of air and fuel on combustion instability. They showed that insufficient mixing was probably the source of the unstable mode observed in the simulation. For combustion instability in spray combustion, in contrast, the number of previous studies is very small. Most recently, Tachibana et al. [15] were the first to perform LES of combustion instability in spray combustion and showed that the LES could accurately reproduce combustion instability observed in the experiment. However, the LES was performed under the single condition, and the effects of differences in the combustion conditions on combustion instability were not discussed.

The purpose of the present study is, therefore, to investigate the mechanism of droplet evaporation and combustion instability by means of numerical simulations. First, DNS of the evaporation and combustion of fuel droplets in a static fluid are performed, and the effects of ambient pressure, initial gas temperature, and differences in fuel components and combustion reaction on the evaporation of single and multiple fuel droplets are investigated. Second, LES of gas and spray combustion in a back-step flow are performed, and the mechanism underlying the combustion instability, and the effect of initial droplet diameter on combustion instability are investigated. In addition, DNS of flashback, which is a transient upstream propagation of a flame often caused by combustion instability, in a channel flow is performed, and the effect of a pressure oscillation on flashback characteristics is investigated.

1.2 Thesis outline

This thesis consists of five chapters.

Chapter 1, the present chapter, describes the background, purpose of the study, and outline of this thesis.

Chapter 2 describes the characteristics of the evaporation and combustion of fuel droplets for single- and multi-component fuels in a static fluid. The effects of ambient pressure, initial gas temperature, and differences in fuel components and combustion reaction on the evaporation characteristics are investigated using DNS for a single and multiple fuel droplets. As the single-component fuels, *n*-heptane and *n*-decane are used, and the one-step global reaction model [31] is used for the calculation of the reaction of *n*-decane. As the multi-component fuels, the surrogate fuels of Jet-A (one-component fuel: *n*-decane, two-component fuel: *n*-decane and 1,2,4-trimethyl-benzene [32], three-component fuel: *n*-dodecane, *iso*-octane, and toluene [33–35]) are used. For the calculations of the reactions, the detailed reaction models that consider 113 chemical species and 891 reactions for the one- and two-component fuels [32], and 273 chemical species and 2322 reactions for the three-component fuel [33–35] are used, respectively.

Chapter 3 describes the characteristics of combustion instability in a back-step flow. LES of gas and spray combustion are performed, and the mechanism underlying the combustion instability and the effect of initial droplet diameter on combustion instability are investigated. Methane and kerosene are used as the fuel for gas and spray combustion, respectively. For the calculations of the reactions, the two-step global reaction models [26, 36] are used with the dynamic thickened flame model [24, 25] to incorporate the effects of SGS turbulence on the reactions.

Chapter 4 describes the characteristics of flashback in a channel flow. The effect of a pressure oscillation that is caused by a virtual combustion instability on the flashback characteristics is investigated using DNS. Hydrogen is used as the fuel, and the detailed reaction model that considers 9 chemical species and 20 reactions [37] is used for the calculation of the reaction.

Chapter 5 summarizes this study and suggests future related areas of researches.

References

- [1] International civil aviation organization. <http://www.icao.int/Pages/default.aspx>.
- [2] F. Culick, M. V. Heitor, and J. H. Whitelaw. *Unsteady combustion*. Springer Science & Business Media, 1996.
- [3] M. Zhu, A. P. Dowling, and K. N. C. Bray. Self-excited oscillations in combustors with spray atomizers. *Journal of Engineering for Gas Turbines and Power*, 123(4):779–786, 2001.
- [4] T. C. Lieuwen and V. Yang. Combustion instabilities in gas turbine engines: Operational experience, fundamental mechanisms and modeling. *Progress in Astronautics and Aeronautics*, 2005.
- [5] M. de la Cruz García, E. Mastorakos, and A. P. Dowling. Investigations on the self-excited oscillations in a kerosene spray flame. *Combustion and Flame*, 156(2):374–384, 2009.
- [6] M. Nakamura, F. Akamatsu, R. Kurose, and M. Katsuki. Combustion mechanism of liquid fuel spray in a gaseous flame. *Physics of Fluids*, 17(12):123301, 2005.
- [7] H. Watanabe, R. Kurose, S.-M. Hwang, and F. Akamatsu. Characteristics of flamelets in spray flames formed in a laminar counterflow. *Combustion and Flame*, 148(4):234–248, 2007.
- [8] H. Watanabe, R. Kurose, S. Komori, and H. Pitsch. Effects of radiation on spray flame characteristics and soot formation. *Combustion and Flame*, 152(1):2–13, 2008.
- [9] Y. Baba and R. Kurose. Analysis and flamelet modelling for spray combustion. *Journal of Fluid Mechanics*, 612:45–79, 2008.
- [10] A. Fujita, H. Watanabe, R. Kurose, and S. Komori. Two-dimensional direct numerical simulation of spray flames—Part 1: Effects of equivalence ratio, fuel droplet size and radiation, and validity of flamelet model. *Fuel*, 104:515–525, 2013.

- [11] T. Sattelmayer, R. von der Bank, and T. Schilling. Forced low-frequency spray characteristics of a generic airblast swirl diffusion burner. *Journal of Engineering for Gas Turbines and Power*, 127(2):301–306, 2005.
- [12] J.-Y. Lee, E. Lubarsky, and B. T. Zinn. “Slow” active control of combustion instabilities by modification of liquid fuel spray properties. *Proceedings of the Combustion Institute*, 30(2):1757–1764, 2005.
- [13] H. Moriai, R. Kurose, H. Watanabe, Y. Yano, F. Akamatsu, and S. Komori. Large-eddy simulation of turbulent spray combustion in a subscale aircraft jet engine combustor—predictions of NO and soot concentrations. *Journal of Engineering for Gas Turbines and Power*, 135(9):091503, 2013.
- [14] W. P. Jones, A. J. Marquis, and K. Vogiatzaki. Large-eddy simulation of spray combustion in a gas turbine combustor. *Combustion and Flame*, 161(1):222–239, 2014.
- [15] S. Tachibana, K. Saito, T. Yamamoto, M. Makida, T. Kitano, and R. Kurose. Experimental and numerical investigation of thermo-acoustic instability in a liquid-fuel aero-engine combustor at elevated pressure: Validity of large-eddy simulation of spray combustion. *Combustion and Flame*, 162(6):2621–2637, 2015.
- [16] B. Yenerdag, N. Fukushima, M. Shimura, M. Tanahashi, and T. Miyauchi. Turbulence–flame interaction and fractal characteristics of H₂–air premixed flame under pressure rising condition. *Proceedings of the Combustion Institute*, 35(2):1277–1285, 2015.
- [17] H. Wang, K. Luo, and J. Fan. Effects of turbulent intensity and droplet diameter on spray combustion using direct numerical simulation. *Fuel*, 121:311–318, 2014.
- [18] J. H. Chen. Petascale direct numerical simulation of turbulent combustion—fundamental insights towards predictive models. *Proceedings of the Combustion Institute*, 33(1):99–123, 2011.

- [19] N. Peters. Laminar diffusion flamelet models in non-premixed turbulent combustion. *Progress in Energy and Combustion Science*, 10(3):319–339, 1984.
- [20] N. Peters. *Turbulent combustion*. Cambridge university press, 2000.
- [21] C. D. Pierce and P. Moin. Progress-variable approach for large-eddy simulation of non-premixed turbulent combustion. *Journal of Fluid Mechanics*, 504:73–97, 2004.
- [22] T. Kitano, T. Nakatani, R. Kurose, and S. Komori. Two-dimensional direct numerical simulation of spray flames—Part 2: Effects of ambient pressure and lift, and validity of flamelet model. *Fuel*, 104:526–535, 2013.
- [23] T. D. Butler and P. J. O’rourke. A numerical method for two dimensional unsteady reacting flows. *Symposium (International) on Combustion*, 16(1):1503–1515, 1977.
- [24] J.-P. L egier, T. Poinso, and D. Veynante. Dynamically thickened flame LES model for premixed and non-premixed turbulent combustion. *Proceedings of the summer program*, 157–168, 2000.
- [25] F. Charlette, C. Meneveau, and D. Veynante. A power-law flame wrinkling model for LES of premixed turbulent combustion Part I: non-dynamic formulation and initial tests. *Combustion and Flame*, 131(1):159–180, 2002.
- [26] B. Franzelli, E. Riber, L. Y. M. Gicquel, and T. Poinso. Large eddy simulation of combustion instabilities in a lean partially premixed swirled flame. *Combustion and Flame*, 159(2):621–637, 2012.
- [27] R. S. Miller, K. Harstad, and J. Bellan. Evaluation of equilibrium and non-equilibrium evaporation models for many-droplet gas-liquid flow simulations. *International Journal of Multiphase Flow*, 24(6):1025–1055, 1998.
- [28] R. S. Miller and J. Bellan. Direct numerical simulation of a confined three-dimensional gas mixing layer with one evaporating hydrocarbon-droplet-laden stream. *Journal of Fluid Mechanics*, 384:293–338, 1999.

- [29] K. Sato, E. Knudsen, and H. Pitsch. Study of combustion instabilities imposed by inlet velocity disturbance in combustor using LES. *ASME Turbo Expo 2009: Power for Land, Sea, and Air*, 87–99, 2009.
- [30] P. Wolf, G. Staffelbach, L. Y. M. Gicquel, J.-D. Müller, and T. Poinsot. Acoustic and large eddy simulation studies of azimuthal modes in annular combustion chambers. *Combustion and Flame*, 159(11):3398–3413, 2012.
- [31] C. K. Westbrook and F. L. Dryer. Chemical kinetic modeling of hydrocarbon combustion. *Progress in Energy and Combustion Science*, 10(1):1–57, 1984.
- [32] S. Honnet, K. Seshadri, U. Niemann, and N. Peters. A surrogate fuel for kerosene. *Proceedings of the Combustion Institute*, 32(1):485–492, 2009.
- [33] G. Blanquart, P. Pepiot-Desjardins, and H. Pitsch. Chemical mechanism for high temperature combustion of engine relevant fuels with emphasis on soot precursors. *Combustion and Flame*, 156(3):588–607, 2009.
- [34] K. Narayanaswamy, G. Blanquart, and H. Pitsch. A consistent chemical mechanism for oxidation of substituted aromatic species. *Combustion and Flame*, 157(10):1879–1898, 2010.
- [35] H. Watanabe, R. Kurose, M. Hayashi, T. Kitano, and S. Komori. Effects of ambient pressure and precursors on soot formation in spray flames. *Advanced Powder Technology*, 25(4):1376–1387, 2014.
- [36] B. Franzelli, E. Riber, M. Sanjosé, and T. Poinsot. A two-step chemical scheme for kerosene–air premixed flames. *Combustion and Flame*, 157(7):1364–1373, 2010.
- [37] J. A. Miller and C. T. Bowman. Mechanism and modeling of nitrogen chemistry in combustion. *Progress in Energy and Combustion Science*, 15(4):287–338, 1989.

Chapter 2

DNS of droplet evaporation and combustion

2.1 Introduction

In this chapter, droplet evaporation and combustion are investigated using DNS. Droplet evaporation is one of the most important factors that changes the spray combustion behavior, and therefore, it has been studied in various conditions previously.

For the droplet evaporation without combustion, Miller and Bellan [1] performed DNS and discussed the effects of the initial liquid mass loading ratio, initial Stokes number, and initial droplet temperature on the droplet evaporation in a turbulent mixing layer. Also, the effects of the ambient pressure have been investigated for a single droplet or an array of droplets. Nomura and Ujiie [2] experimentally studied the evaporation rate of a single droplet at various ambient pressures in the range of 0.1–5.0 MPa and showed the pressure dependence of droplet lifetime. Yang and Wong [3] performed a numerical simulation of a flow around a single evaporating droplet under the same conditions as the Nomura and Ujiie’s experiments and discussed the effects of the heat conduction from a fiber used in the experiment to suspend the droplet and the radiation from the furnace wall. On the other hand, for the droplet evaporation with combustion, Mikami et al. [4] studied the burning lifetime of interacting two droplets at various ambient pressures in

the range of 0.1–6.0 MPa by experiments, and showed that the pressure dependence of the burning lifetime for the interacting droplets is similar to that of a single droplet. In these studies, however, the evaporation characteristics of multiple droplets have not been discussed.

Fuel components are also the important factors that affect the evaporation behavior of fuel droplets. Daïf et al. [5] performed an experiment using a single and a few droplets of a multi-component fuel composed of *n*-decane and *n*-heptane, and compared the evaporation rate and droplet temperature with the results calculated by the evaporation model of Abramzon and Sirignano [6]. They showed that the evaporation model extended to multi-component droplet evaporation in forced convection gave good results on the droplet radius regression and the droplet surface temperature evolution. For multiple droplets, Le Clercq and Bellan [7] performed a direct numerical simulation of a mixing layer laden with evaporating droplets of a multi-component fuel and compared the results with those of the single-component fuel. They pointed out that the single-component fuel was able to be substituted for the multi-component fuel, but it caused the increased evaporation time. However, these studies have not mentioned the droplet evaporation with combustion.

The purpose of this chapter is therefore to investigate the effects of ambient pressure, initial gas temperature, and differences in fuel components and combustion reaction on the evaporation characteristics of a single and multiple fuel droplets using DNS. For the single-component fuels, *n*-heptane and *n*-decane are used, and the one-step global reaction model [8] is used for the calculation of the reaction of *n*-decane. For the multi-component fuels, on the other hand, the surrogate fuels of Jet-A (one-component fuel: *n*-decane, two-component fuel: *n*-decane and 1,2,4-trimethyl-benzene [9], three-component fuel: *n*-dodecane, *iso*-octane, and toluene [10–12]) are used. For the calculations of the reactions, the detailed reaction models that consider 113 chemical species and 891 reactions for the one- and two-component fuels [9], and 273 chemical species and 2322 reactions for the three-component fuel [10–12] are used, respectively.

2.2 Single-component fuel droplet

2.2.1 Numerical Simulation

2.2.1.1 Governing equations

The governing equations for the gas phase are the conservation equations of mass, momentum, energy, and mass of chemical species as

$$\frac{\partial \rho}{\partial t} + \nabla \cdot (\rho \mathbf{u}) = S_\rho, \quad (2.1)$$

$$\frac{\partial \rho \mathbf{u}}{\partial t} + \nabla \cdot (\rho \mathbf{u} \mathbf{u}) = -\nabla P + \nabla \cdot \boldsymbol{\tau} + S_{\rho u}, \quad (2.2)$$

$$\frac{\partial \rho h}{\partial t} + \nabla \cdot (\rho h \mathbf{u}) = \frac{\partial P}{\partial t} + \mathbf{u} \cdot \nabla P + \nabla \cdot (\rho D_h \nabla h) + \boldsymbol{\tau} \cdot \nabla \mathbf{u} + S_{\rho h}, \quad (2.3)$$

$$\frac{\partial \rho Y_k}{\partial t} + \nabla \cdot (\rho Y_k \mathbf{u}) = \nabla \cdot (\rho D_k \nabla Y_k) + S_{comb,k} + S_{\rho Y_k}, \quad (2.4)$$

and the equation of state for ideal gas [13–16]. Here ρ is the density, \mathbf{u} the velocity, P the pressure, $\boldsymbol{\tau}$ the viscous stress tensor, h the enthalpy, and D_h the thermal diffusivity given as $\rho D_h = \lambda/c_p$, respectively. Here λ and c_p are the heat conductivity and the specific heat capacity, respectively. Y_k and D_k are the mass fraction and the mass diffusion coefficient of species k , which is given under the unity Lewis number assumption as $\rho D_k = \lambda/c_p$, respectively.

The phase coupling between the gas and dispersed-droplets phases is calculated using the Particle-Source-In-Cell (PSI-Cell) method [17]. The source terms, S_ρ , $S_{\rho u}$, $S_{\rho h}$, and $S_{\rho Y_k}$, are given as

$$S_\rho = -\frac{1}{\Delta V} \sum_N \frac{dm_d}{dt}, \quad (2.5)$$

$$S_{\rho u} = -\frac{1}{\Delta V} \sum_N \frac{dm_d \mathbf{u}_d}{dt}, \quad (2.6)$$

$$S_{\rho h} = -\frac{1}{\Delta V} \sum_N \frac{dm_d h_d}{dt}, \quad (2.7)$$

$$S_{\rho Y_k} = -\frac{1}{\Delta V} \sum_N \frac{dm_d}{dt} \quad \text{for } Y_k = Y_F. \quad (2.8)$$

Here ΔV is the volume of the computational cell for the gas phase calculation, m_d the droplet mass, \mathbf{u}_d the droplet velocity, h_d the enthalpy of a fuel droplet, and N the

number of fuel droplets in the computational cell. $S_{comb,k}$ is the source term due to the reaction described later.

Concerning the evaporation of fuel droplets, the non-equilibrium Langmuir–Knudsen evaporation model [1, 18, 19] is employed. The governing equations for the droplet position, \mathbf{x}_d , velocity, \mathbf{u}_d , temperature, T_d , and mass, m_d , are given as

$$\frac{d\mathbf{x}_d}{dt} = \mathbf{u}_d, \quad (2.9)$$

$$\frac{d\mathbf{u}_d}{dt} = \frac{f_s}{\tau_d}(\mathbf{u} - \mathbf{u}_d), \quad (2.10)$$

$$\frac{dT_d}{dt} = \frac{Nu}{3Pr} \left(\frac{c_p}{c_{p,d}} \right) \left(\frac{f_t}{\tau_d} \right) (T - T_d) + \frac{\dot{m}_d L_V}{m_d c_{p,d}}, \quad (2.11)$$

$$\frac{dm_d}{dt} = \dot{m}_d. \quad (2.12)$$

Here T is the gas temperature, $c_{p,d}$ the specific heat capacity of the fuel droplet, L_V the latent heat of evaporation at T_d , and τ_d the particle response time defined as

$$\tau_d = \frac{\rho_d d^2}{18\mu}. \quad (2.13)$$

Here ρ_d is the droplet density, μ the viscosity, and d the droplet diameter. The Prandtl and Nusselt numbers in the gas phase are given as

$$Pr = \frac{\mu}{\rho D_h}, \quad Nu = 2 + 0.552 Re_{sl}^{1/2} Pr^{1/3}. \quad (2.14)$$

Here $Re_{sl} = \rho u_{sl} d / \mu$ is the Reynolds number based on the slip velocity, $u_{sl} = |\mathbf{u} - \mathbf{u}_d|$. The corrections of the Stokes drag and heat transfer for the evaporating fuel droplet, f_s and f_t [13, 19, 20], are given as

$$f_s = \frac{1 + 0.0545 Re_{sl} + 0.1 Re_{sl}^{1/2} (1 - 0.03 Re_{sl})}{1 + b Re_b^c}, \quad f_t = \frac{\beta}{e^\beta - 1}, \quad (2.15)$$

$$b = 0.06 + 0.077 \exp(-0.4 Re_{sl}), \quad c = 0.4 + 0.77 \exp(-0.04 Re_{sl}).$$

Here $Re_b = \rho u_b d / \mu$ is the Reynolds number based on the blowing velocity, $u_b = \dot{m}_d / (\pi d^2 \rho)$. β is the non-dimensional evaporation parameter described later.

2.2.1.2 Evaporation model

For the evaporation of the fuel droplet, the non-equilibrium Langmuir–Knudsen evaporation model is used [1, 18, 19]. The effect of the temperature gradient inside the droplet is neglected since the effect is small [19]. As the liquid fuel, n -heptane and n -decane are used. Evaporation rate in Eq. (2.12) is given as

$$\dot{m}_d = -\frac{m_d}{\tau_d} \left(\frac{Sh}{3Sc} \right) \ln(1 + B_M), \quad (2.16)$$

[1, 18, 19], where Sc and Sh are the Schmidt and Sherwood numbers given as

$$Sc = \frac{\mu}{\rho D_k}, \quad Sh = 2 + 0.552 Re_{sl}^{1/2} Sc^{1/3}, \quad (2.17)$$

and B_M is the mass transfer number given as

$$B_M = \frac{Y_{F,s} - Y_F}{1 - Y_{F,s}}. \quad (2.18)$$

Here Y_F is the mass fraction of fuel vapor in the far-field condition for the fuel droplet, which is represented by the value in the cell where the fuel droplet is located (this condition is the same for \mathbf{u} and T), and $Y_{F,s}$ is the vapor surface mass fraction (i.e., saturated vapor mass fraction) given as

$$Y_{F,s} = \frac{X_{F,s}}{X_{F,s} + (1 - X_{F,s})\bar{W}/W_F}, \quad (2.19)$$

$$X_{F,s} = \frac{P_{sat}}{P} - \left(\frac{2L_K}{d} \right) \beta. \quad (2.20)$$

Here $X_{F,s}$ is the mole fraction of fuel vapor at the droplet surface, P_{sat} the saturated vapor pressure discussed later, \bar{W} the averaged molecular weight of the carrier gas, and W_F the molecular weight of the fuel vapor, respectively. In Eq. (2.20), the non-equilibrium effect is considered using the Langmuir–Knudsen evaporation law, in which the non-dimensional evaporation parameter, β , is given as

$$\beta = - \left(\frac{\rho_d Pr}{8\mu} \right) \frac{dd^2}{dt}. \quad (2.21)$$

The Knudsen layer thickness, L_K , is estimated as

$$L_K = \frac{\mu \{2\pi T_d (R/W_F)\}^{1/2}}{ScP}. \quad (2.22)$$

Here R is the universal gas constant.

2.2.1.3 Saturated vapor pressure

In general, the saturated vapor pressure, P_{sat} , in Eq. (2.20) is calculated as

$$P_{sat} = P \exp \left\{ \frac{L_V W_F}{R} \left(\frac{1}{T_B} - \frac{1}{T_d} \right) \right\}, \quad (2.23)$$

where T_B is the boiling temperature. This equation is derived from the Clausius–Clapeyron equation,

$$\frac{dP_{sat}}{dT} = \frac{L_V W_F}{T(v_g - v_l)}, \quad (2.24)$$

under the assumptions of the constant L_V and ideal gas. Here v_g and v_l are the molar volumes of the gas and liquid phases, respectively. However, the validities of these assumptions have not been fully examined.

In order to exactly solve Eq. (2.24), the equation is numerically integrated using the exact values of L_V , v_g , and v_l . L_V is estimated by using the Watson equation [21] as

$$L_V = L_{V,B,atm} \left(\frac{T_c - T_d}{T_c - T_{B,atm}} \right)^{0.38}, \quad (2.25)$$

where $T_{B,atm}$ is the normal boiling temperature, T_c the critical temperature, and $L_{V,B,atm}$ the latent heat at $T_{B,atm}$. On the other hand, v_g and v_l are calculated using the equation of state for real gas and the equation of the corresponding states correlation, respectively. As these equations, Peng-Robinson equation [22] and Gunn-Yamada equation [23] are used, respectively. The Peng-Robinson equation is described as

$$v_g = \frac{RT}{P} z. \quad (2.26)$$

Here z is the compressibility factor given as

$$z^3 - (1 - C_{z,2})z^2 + (C_{z,1} - 3C_{z,2}^2 - 2C_{z,2})z - (C_{z,1}C_{z,2} - C_{z,2}^2 - C_{z,2}^3) = 0, \quad (2.27)$$

$$C_{z,1} = \frac{aP}{R^2T^2}, \quad C_{z,2} = \frac{bP}{RT},$$

where a and b are calculated as

$$a = 0.45724 \frac{R^2 T_c^2}{P_c} \alpha, \quad b = 0.07780 \frac{RT_c}{P_c}, \quad (2.28)$$

$$\alpha^{1/2} = 1 + (0.37464 + 1.54226\omega - 0.26992\omega^2)(1 - T_r^{1/2}).$$

Here P_c is the critical pressure and $T_r = T/T_c$ the reduced temperature. The values of the acentric factor, ω , for n -decane and n -heptane are 0.488 and 0.349, respectively [24]. The Gunn-Yamada equation is described as

$$\begin{aligned} v_l &= v_r^{(0)}(1 - \omega\Gamma)v_{sc}, \\ v_{sc} &= \frac{RT_c}{P_c}(0.2920 - 0.0967\omega), \end{aligned} \quad (2.29)$$

where $v_r^{(0)}$ and Γ are calculated with T_r as

$$v_r^{(0)} = \begin{cases} 0.33593 - 0.33953T_r + 1.51941T_r^2 - 2.02512T_r^3 + 1.11422T_r^4 & (0.2 \leq T_r \leq 0.8) \\ 1.0 + 1.3(1 - T_r)^{1/2} \log_{10}(1 - T_r) - 0.50879(1 - T_r) - 0.91534(1 - T_r)^2 & (0.8 < T_r < 1.0), \end{cases} \quad (2.30)$$

$$\Gamma = 0.29607 - 0.09045T_r - 0.04842T_r^2 \quad (0.2 \leq T_r < 1.0). \quad (2.31)$$

On the other hand, empirical expressions for P_{sat} have been proposed by Antoine [25] and Sato [26] based on the measurements. The Antoine's expression [25] is described as

$$\log_{10} P_{sat} = C_{A,1} - \frac{C_{A,2}}{T + C_{A,3}}, \quad (2.32)$$

where $C_{A,1}$, $C_{A,2}$, and $C_{A,3}$ are the experimental constants. For n -decane, $C_{A,1} = 4.07857$, $C_{A,2} = 1501.268$ and $C_{A,3} = -78.67$ are used, and for n -heptane, $C_{A,1} = 4.02832$, $C_{A,2} = 1268.636$, and $C_{A,3} = -56.199$ are used. It should be noted that the unit of P_{sat} is [bar] in this expression. The Sato's expression for non-polar substance [26] is described as

$$P_{sat}^{0.119} = 11.9T^{0.119} + C_S, \quad (2.33)$$

where C_S is the experimental constant. For n -decane and n -heptane, $C_S = -22.4066$ and $C_S = -21.9011$ are used, respectively. It should be noted that the unit of P_{sat} is [mmHg] in this expression.

Fig. 2.1 shows the comparison of the saturated vapor pressure, P_{sat} , against droplet surface temperature, T_d , calculated by Eqs. (2.23), (2.24), (2.32), and (2.33) for n -decane

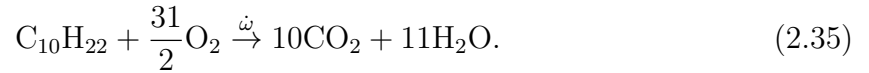
and *n*-heptane. Here T_B in Eq. (2.23) is calculated using Sato's expression (Eq. (2.33)) as

$$T_B = \left(\frac{P^{0.119} - C_S}{11.9} \right)^{1/0.119}. \quad (2.34)$$

The third-order explicit Runge–Kutta method is used for the numerical integration of Eq. (2.24). While the exact prediction of P_{sat} by Eq. (2.24) is in good agreement with the empirical expressions by the Antoine [25] and Sato [26], the assumed prediction by Eq. (2.23) overestimates them. Accordingly, the Sato's expression [26] is employed in the present computations.

2.2.1.4 Reaction model

For the calculation of the reaction of *n*-decane, the following one-step global reaction model [8] is used.



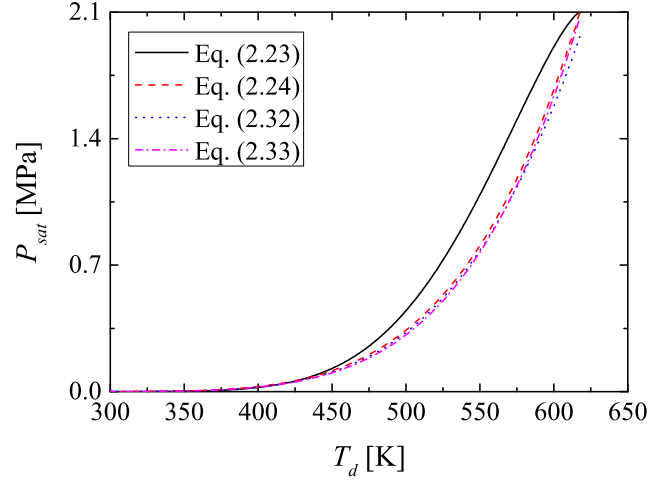
The reaction rate, $\dot{\omega}$, is given as

$$\dot{\omega} = A \exp\left(-\frac{E_a}{RT}\right) [\text{C}_{10}\text{H}_{22}]^{n_{\text{C}_{10}\text{H}_{22}}} [\text{O}_2]^{n_{\text{O}_2}}. \quad (2.36)$$

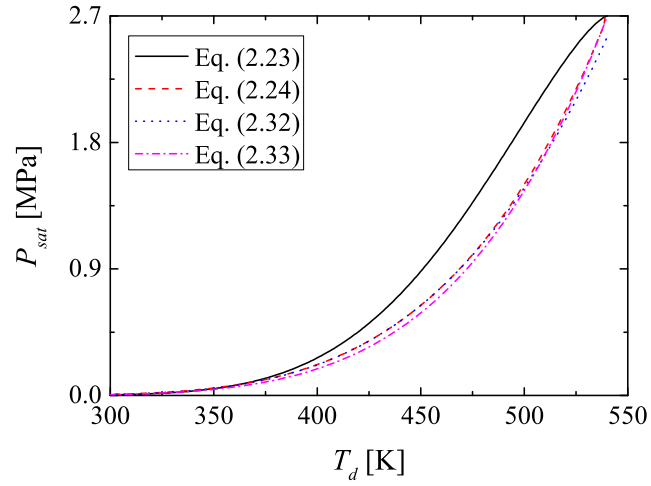
Here [-] represents the mole concentration of chemical species. $A = 3.8 \times 10^{11}$ is the frequency factor, $E_a = 30$ [kcal/mol] the activation energy, and $n_{\text{C}_{10}\text{H}_{22}} = 0.25$ and $n_{\text{O}_2} = 1.5$ the reaction exponents.

2.2.1.5 Computational details

Fig. 2.2 shows the schematic of the computational domain and the initial droplet distributions. The computational domain is a cube 5 mm on a side and is divided into 50 uniform computational grid points in the each direction. The staggered grid is used for the computational grid. The number of grid points was determined by comparing the computational results obtained by computations with 0.125 million ($= 50^3$) and 1 million ($= 100^3$) grid points. The differences in droplet lifetime described later between them were less than 1.3% for all cases. The computations are performed for the evaporation of a single fuel droplet and for the evaporation/combustion reaction of multiple

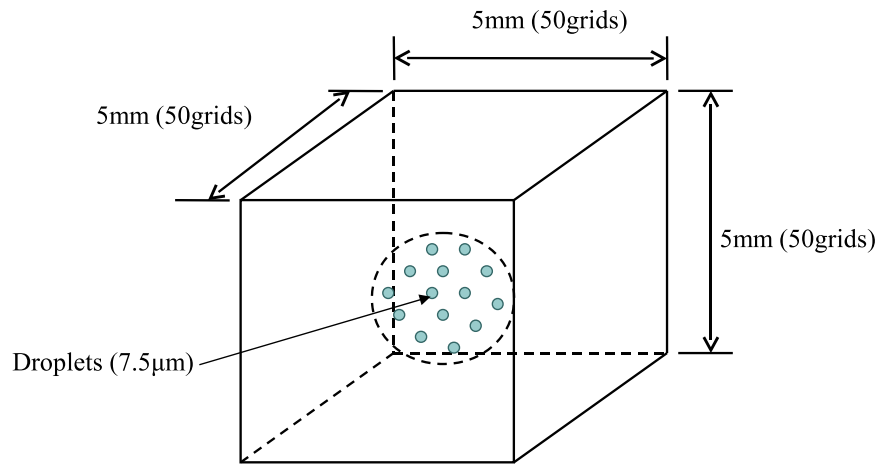


(a) *n*-Decane

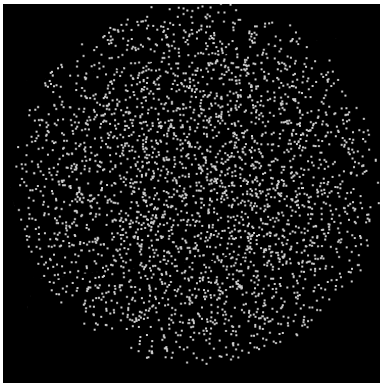


(b) *n*-Heptane

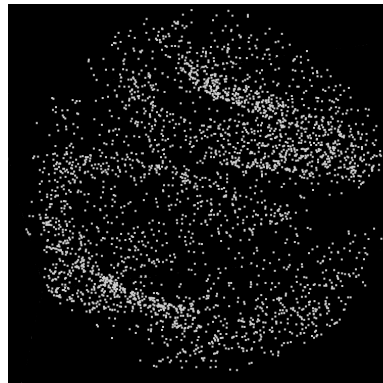
Figure 2.1: Comparison of saturated vapor pressure, P_{sat} , against droplet surface temperature, T_d , calculated by Eqs. (2.23), (2.24), (2.32), and (2.33) for *n*-decane and *n*-heptane.



(a) Computational domain



(b) Random distribution



(c) Inhomogeneous distribution

Figure 2.2: Computational domain and initial droplet distributions.

Table 2.1: Computational conditions.

Cases	T_0 [K]	ML [-] (ϕ [-])	Ambient gas	Droplet distribution	G [-]
1	1000	0.027 (-)	Nitrogen	Random	2.8–61.8
2	1500	0.027 (-)	Nitrogen	Random	2.1–46.4
3	2000	0.027 (-)	Nitrogen	Random	1.4–30.9
4*	2000	0.054 (-)	Nitrogen	Random	2.8–61.8
5	1000	0.12 (-)	Nitrogen	Random	13.6–276.0
6	1500	0.12 (-)	Nitrogen	Random	10.2–207.0
7	2000	0.12 (-)	Nitrogen	Random	6.8–138.0
8	1000	0.027 (0.411)	Air	Random	2.8–61.8
9	1500	0.027 (0.411)	Air	Random	2.1–46.4
10	2000	0.027 (0.411)	Air	Random	1.4–30.9
11*	2000	0.054 (0.822)	Air	Random	2.8–61.8
12	1000	0.12 (1.85)	Air	Random	13.6–276.0
13	1500	0.12 (1.85)	Air	Random	10.2–207.0
14	2000	0.12 (1.85)	Air	Random	6.8–138.0
15	2000	0.36 (5.55)	Air	Random	20.4–414.0
16	2000	0.027 (-)	Nitrogen	Inhomogeneous	1.4–30.9
17*	2000	0.054 (-)	Nitrogen	Inhomogeneous	2.8–61.8
18	2000	0.027 (0.411)	Air	Inhomogeneous	1.4–30.9
19*	2000	0.054 (0.822)	Air	Inhomogeneous	2.8–61.8

* Cases using a parcel model in which one parcel represents two fuel droplets.

All cases are performed under the ambient pressure conditions of 0.1, 0.5, 1.0, 1.5, and 2.0 MPa.

fuel droplets. Initially, the single fuel droplet and multiple fuel droplets are allocated at the center of the computational domain and in the central region as the spherical shape with 2 mm diameter, respectively. The initial droplet diameters are set to 700 μm for the single fuel droplet and 7.5 μm for the multiple fuel droplets. These droplet sizes are decided to compare with the experiments [2] and to meet the requirements associated with the grid size from the point of view of numerical accuracy, respectively (the grid spacing needs to be roughly 10 times larger than the droplet size to get enough accuracy by using the PSI-Cell method [27]). The initial droplet temperature is 300 K. As the fuel, *n*-decane and *n*-heptane are used for the evaporation of the single fuel droplet, whereas *n*-decane is used for the evaporation/combustion reaction of the multiple fuel droplets.

Table 2.1 lists the computational conditions performed for the evaporation/combustion reaction of the multiple fuel droplets. The ambient pressure, P , initial gas temperature, T_0 , and droplet mass loading ratio, ML , are varied in the ranges of 0.1–2.0 MPa, 1000–2000 K, and 0.027–0.36, respectively. Here ML is the ratio of the total mass of fuel droplets to the mass of gas in the spherical region. In order to investigate the effects of combustion reaction and inhomogeneity of droplet distribution, the computations are carried out for different mediums of the ambient gas (i.e., nitrogen and air) and the initial droplet distributions (i.e., random and inhomogeneous). Here the inhomogeneous droplet distribution is obtained by the DNS data for the droplet distributions in an isotropic turbulence in Matsuda et al. [28]. In order to increase ML of inhomogeneous droplet distributions, the parcel model [13] in which one parcel represents two fuel droplets is applied. These cases with the parcel model are indicated using a superscription * as 4*, 11*, 17*, and 19* in Table 2.1. In the table, G is the Group combustion number [29] given as

$$G = \frac{3}{4}Le(2 + 0.552Re_{st}^{1/2}Sc^{1/3})n_T^{2/3}(d/l). \quad (2.37)$$

Here Le is the Lewis number, n_T the total number of the fuel droplets, and l the mean distance between the fuel droplets.

For the numerical approximation of the gas phase, discretization of the nonlinear

terms of the momentum equations is derived from the second-order fully conservative finite difference scheme [30, 31]. For the convection terms of the energy and mass fractions of chemical species, the QUICK scheme [32] is employed. Other differentials are approximated by the second-order finite difference method. The third-order explicit Runge–Kutta method is used for the time advancement calculation of the convective terms. The fractional step method [33] is used as the computational algorithm. On all six boundaries, the free outflow condition is given.

The values of the droplet density, ρ_d , and the specific heat capacity of the droplet, $c_{p,d}$, are calculated by the curve fit data from the NIST web book [24], and other thermo physical properties and transport coefficients under various pressures are obtained from CHEMKIN [34, 35]. Here the reference temperature, T_{ref} , and reference mass fraction, $Y_{k,ref}$, are calculated by “1/3 rule” [19] as

$$T_{ref} = \frac{1}{3}T + \frac{2}{3}T_d, \quad Y_{k,ref} = \frac{1}{3}Y_k + \frac{2}{3}Y_{k,s}. \quad (2.38)$$

Regarding the computations for the evaporation of the single droplet, the droplet diameter of 700 μm is larger than the computational grid, and therefore, PSI-Cell method cannot be used. Therefore, the evaporation rate of the single droplet is calculated under the assumption that the variations of the gas temperature and mass fraction of fuel gas caused by the droplet evaporation are negligibly small.

2.2.2 Results and discussion

2.2.2.1 Single fuel droplet without combustion

In this section, the effects of ambient pressure and initial gas temperature on the evaporation of a single fuel droplet are investigated by comparing with the experiments by Nomura and Ujiie [2]. In the previous numerical study by Yang and Wong [3], they pointed out that radiation from the furnace wall and heat conduction from a fiber used for suspending a fuel droplet may enhance the droplet evaporation in the experiments. In addition, it is speculated that natural convection around the droplet surface affects the droplet evaporation. This is because the gravity fluctuation with 1/100 of normal

gravity was measured in the experiments, although the experiments were reported to be performed in a microgravity condition.

In Fig. 2.3, the comparisons of time variation of the normalized squared droplet diameter, $(d/d_0)^2$, between numerical simulations and experiments [2] with and without radiation and natural convection is shown for *n*-heptane. Here both axes are normalized by the square of the initial droplet diameter. The left-hand side and right-hand side figures show the low-initial-gas-temperature and high-initial-gas-temperature cases, respectively. The radiative heat absorption, Q_{rad} , is calculated as

$$Q_{rad} = \pi d^2 \sigma \alpha (T^4 - T_d^4), \quad (2.39)$$

where σ is the Stephan-Boltzmann coefficient and $\alpha = 0.93$ the surface absorptance [3]. In order to take the effect of the natural convection into account, gravity effect is introduced into the Nusselt and Sherwood numbers as

$$Nu = 2 + 0.6(Gr^{1/2} + Re_{sl})^{1/2} Pr^{1/3}, \quad (2.40)$$

$$Sh = 2 + 0.6(Gr^{1/2} + Re_{sl})^{1/2} Sc^{1/3}. \quad (2.41)$$

Here Gr is Grashof number defined as

$$Gr = \frac{g \rho^2 (T - T_d) d^3}{T \mu^2}, \quad (2.42)$$

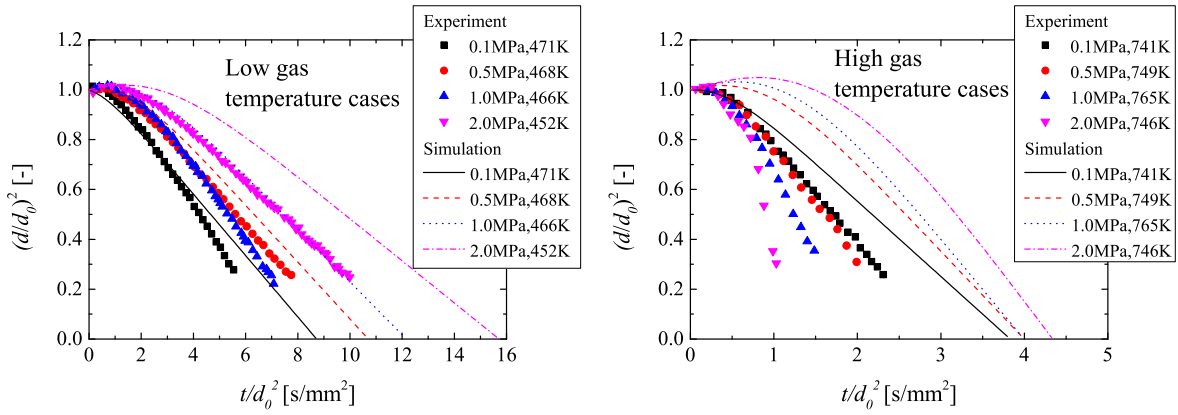
[36, 37], where g is the gravity. The effect of heat conduction of a fiber used for suspending a fuel droplet is neglected here because of the uncertainty of its condition in the experiments [2]. It is observed that the predictions of $(d/d_0)^2$ monotonously decrease with increasing t/d_0^2 and that their slopes become gentle at low-initial-gas-temperature cases and steep at high-initial-gas-temperature cases as the ambient pressure increases, and become steep as the initial gas temperature increases. Also, the predictions become to be in better agreement with the experiments [2] by taking the effects of the radiation and natural convection into account. In the conditions of high ambient pressure and initial gas temperature (see the right-hand side figure in Fig. 2.3(c)), however, the differences between the predictions and the experiments are still marked even if the effects

of the radiation and natural convection are taken into account. In particular, the effect of the ambient pressure is quite different. Compared to the experiments [2], the increase of droplet size due to droplet expansion greatly surpasses the decrease of it due to droplet evaporation in these conditions in the numerical simulations. It is considered that this is due to the fact that the effect of heat conduction from a fiber used for suspending a fuel droplet, which could enhance the droplet evaporation, is neglected in the numerical simulations. In addition, the difficulties in measuring the droplet size in the experiments may deteriorate the accuracies of the experimental data. The time variations of normalized squared droplet diameter, $(d/d_0)^2$, for *n*-decane are also shown in Fig. 2.4. In all conditions, the droplet expansion is more evident and the droplet evaporation proceeds slower for *n*-decane than those for *n*-heptane.

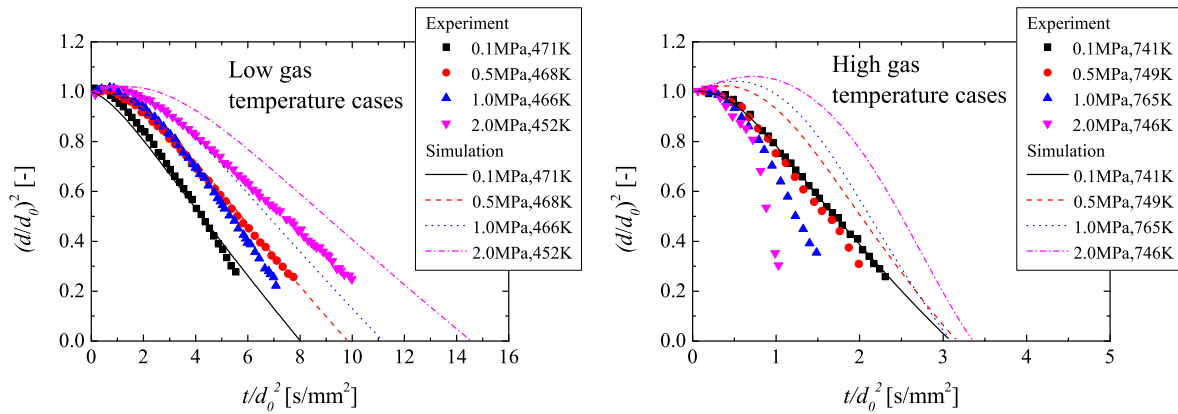
In the computations for the evaporation and combustion reaction of multiple fuel droplets, whose results are shown in the following sections, the effects of radiation and natural convection are neglected. This is because small droplets with diameter of 7.5 μm are used, and therefore, the evaporation time is as short as the order of 10^{-4} s.

2.2.2.2 Multiple fuel droplets without combustion

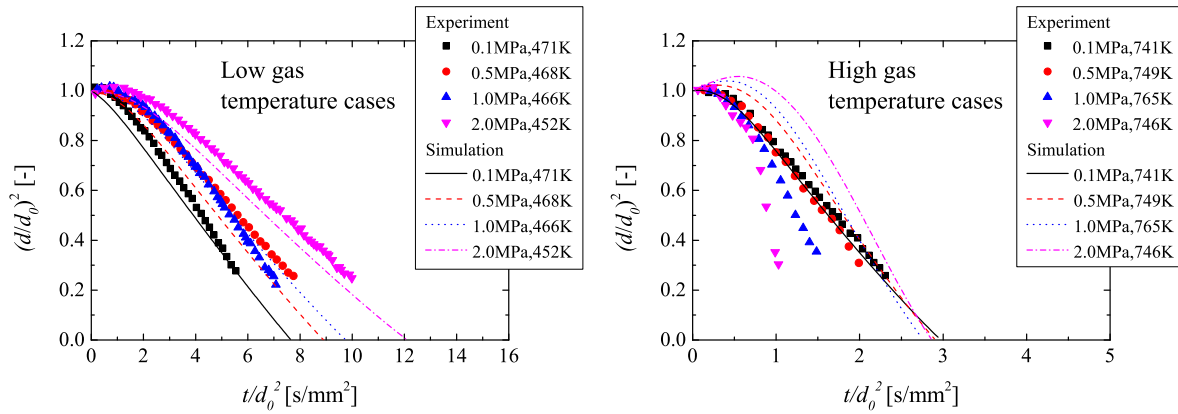
Figs. 2.5 and 2.6 show the time variations of total droplet mass, m/m_0 , in nitrogen at initial gas temperature of $T_0 = 1000, 1500, \text{ and } 2000$ K for $ML = 0.027$ and 0.12 , respectively. As the ambient pressure increases, the start-up of droplet evaporation is delayed and the evaporation rate is enhanced once the evaporation starts. This is because as the ambient pressure increases, droplet evaporation is suppressed by higher boiling temperature because the heat from the ambient gas is used not for the evaporation but for raising the droplet temperature, whereas it is enhanced by lower latent heat (Eq. (2.25)) and larger droplet surface area due to greater liquid expansion (i.e., lower liquid density) caused by the increase of droplet temperature. The former and latter factors affect the droplet evaporation rate in the early and subsequent evaporation periods, respectively. Also, since only the latter factor is influenced by the ambient gas temperature, the slope of m/m_0 becomes steep with increasing the initial gas temperature, T_0 . The comparison



(a) Without radiation and natural convection

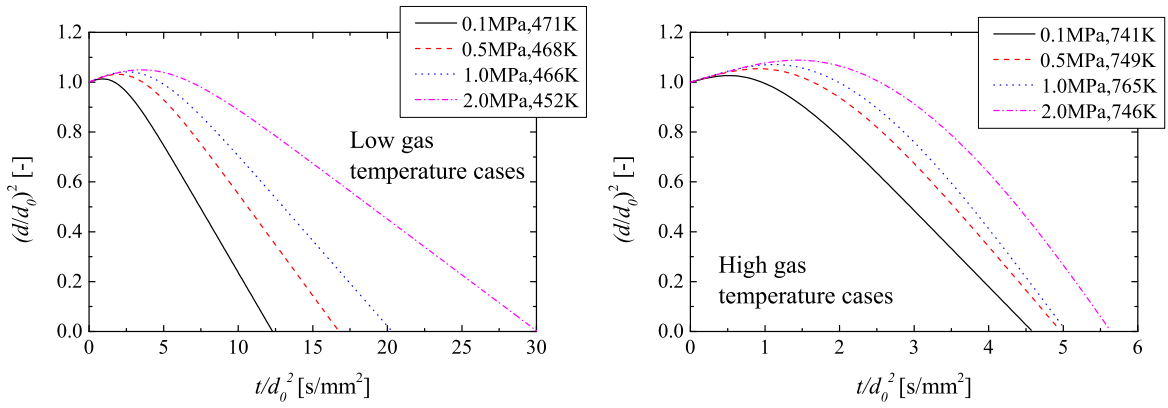


(b) With radiation

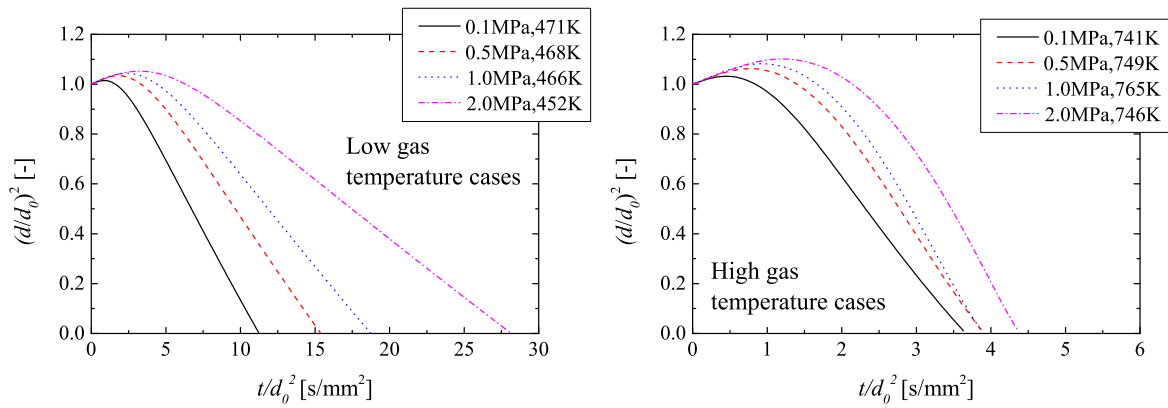


(c) With radiation and natural convection

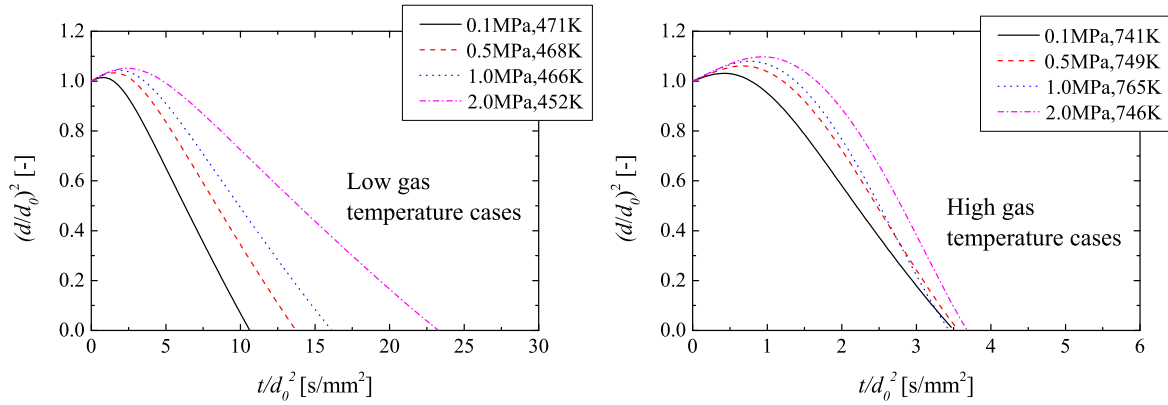
Figure 2.3: Comparisons of time variation of normalized squared droplet diameter, $(d/d_0)^2$, between numerical simulations and experiments [2] with and without radiation and natural convection for *n*-heptane.



(a) Without radiation and natural convection



(b) With radiation



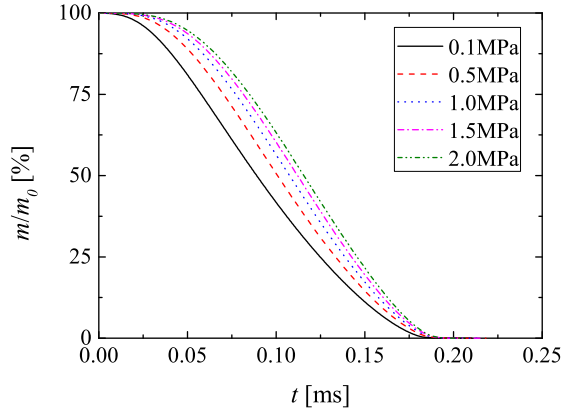
(c) With radiation and natural convection

Figure 2.4: Time variations of normalized squared droplet diameter, $(d/d_0)^2$, with and without radiation and natural convection for *n*-decane.

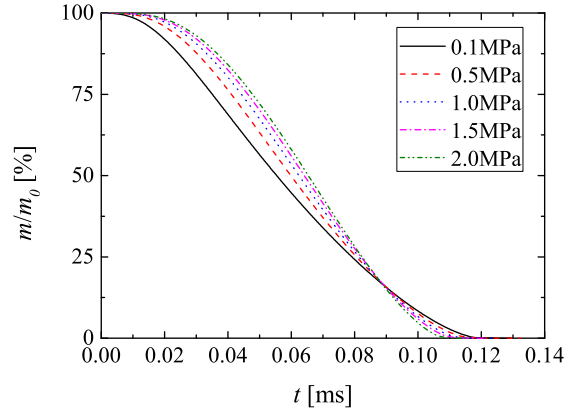
of Figs. 2.5 and 2.6 suggests that this tendency is not influenced by ML .

In order to understand the general effects of the ambient pressure, initial gas temperature, and mass loading ratio, ML , on the droplet evaporation, droplet lifetime, which is defined as the time when m/m_0 becomes 1%, is introduced. Fig. 2.7 shows the effects of ambient pressure, P , and ML on droplet lifetime in nitrogen at initial gas temperature of $T_0 = 1000, 1500, \text{ and } 2000$ K. The droplet lifetime is found to increase with increasing the ambient pressure at lower initial gas temperature of $T_0 = 1000$ K, but decrease at higher initial gas temperature of $T_0 = 1500$ and 2000 K. This is attributed to a balance of the increase and decrease of the droplet evaporation rate in higher ambient pressure conditions, as mentioned earlier on Figs. 2.5 and 2.6. This tendency is not influenced by ML , but the droplet lifetime quantitatively becomes longer with increasing ML . This is explained by Fig. 2.8 in which the time variations of gas temperature, T , and ratio of mass fraction of evaporated fuel to vapor surface mass fraction, $Y_F/Y_{F,s}$, in nitrogen at initial gas temperature of $T_0 = 2000$ K and ambient pressure of $P = 2.0$ MPa (see Fig. 2.7(c)) are shown. Compared to in the case of $ML = 0.027$, the decrease of T and the increase of $Y_F/Y_{F,s}$ with time in the case of $ML = 0.12$ are remarkable, which act to suppress the droplet evaporation, and therefore, enlarge the droplet lifetime.

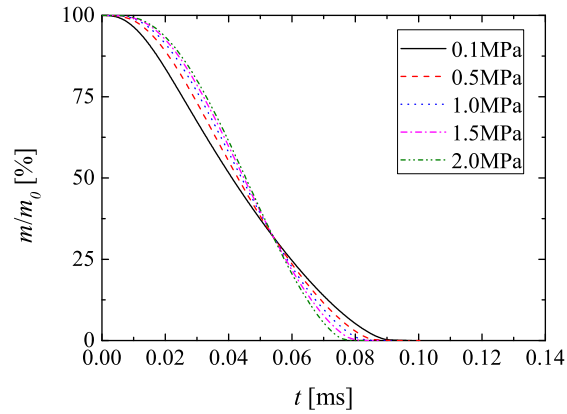
Fig. 2.9 shows the effect of inhomogeneity of the droplet distribution on droplet lifetime in nitrogen at initial gas temperature of $T_0 = 2000$ K for $ML = 0.027$ (without parcel model) and 0.054 (with parcel model). In both cases of $ML = 0.027$ and 0.054 , the inhomogeneity of the droplet distribution is found to make the droplet lifetime longer regardless of the ambient pressure. In order to elucidate the mechanism, probability density function (PDF) of local mass loading ratio, ML_{local} , which is calculated by counting the number of fuel droplets in a cube 0.5 mm on a side, is evaluated at ambient pressure of $P = 2.0$ MPa as shown in Fig. 2.10. Compared to the random droplet distribution, the PDF of the inhomogeneous droplet distribution widely distributes in the higher ML_{local} region, which is considered to contribute to the longer droplet lifetime.



(a) $T_0 = 1000$ K (Case 1)

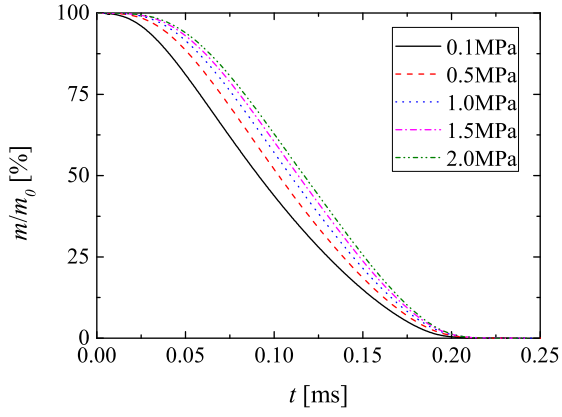


(b) $T_0 = 1500$ K (Case 2)

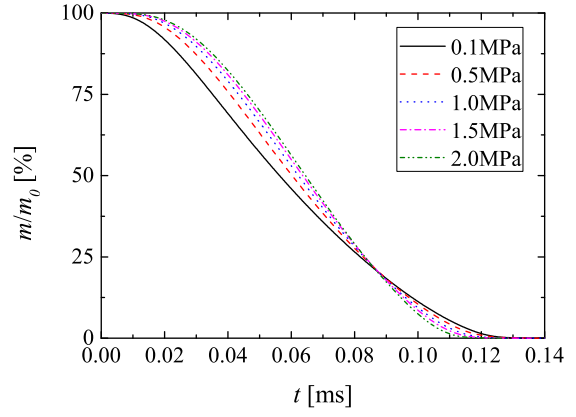


(c) $T_0 = 2000$ K (Case 3)

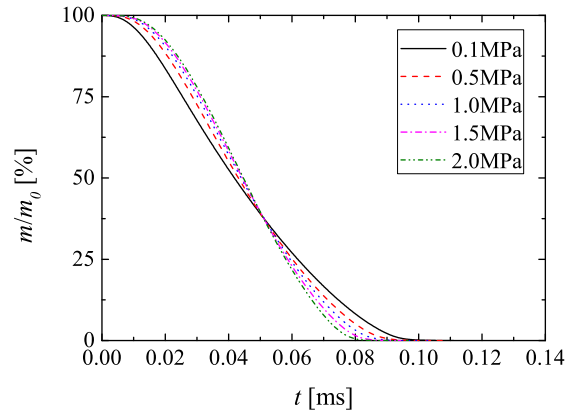
Figure 2.5: Time variations of total droplet mass, m/m_0 , for $ML = 0.027$ in nitrogen at initial gas temperature of $T_0 = 1000$, 1500 , and 2000 K.



(a) $T_0 = 1000$ K (Case 5)

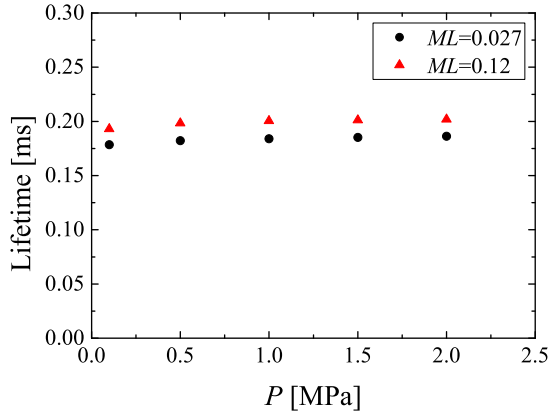


(b) $T_0 = 1500$ K (Case 6)

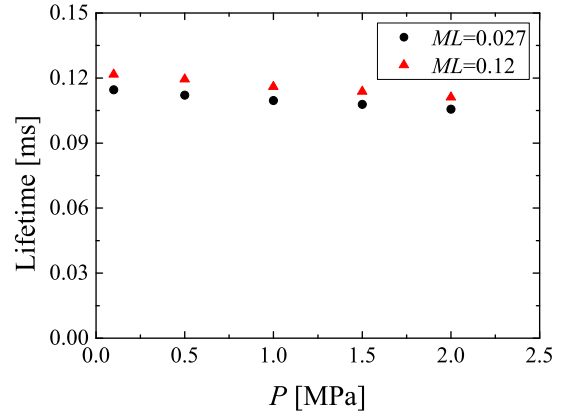


(c) $T_0 = 2000$ K (Case 7)

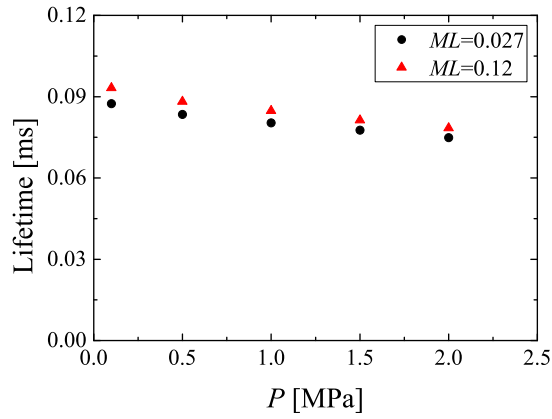
Figure 2.6: Time variations of total droplet mass, m/m_0 , for $ML = 0.12$ in nitrogen at initial gas temperature of $T_0 = 1000, 1500,$ and 2000 K.



(a) $T_0 = 1000$ K (Cases 1 and 5)

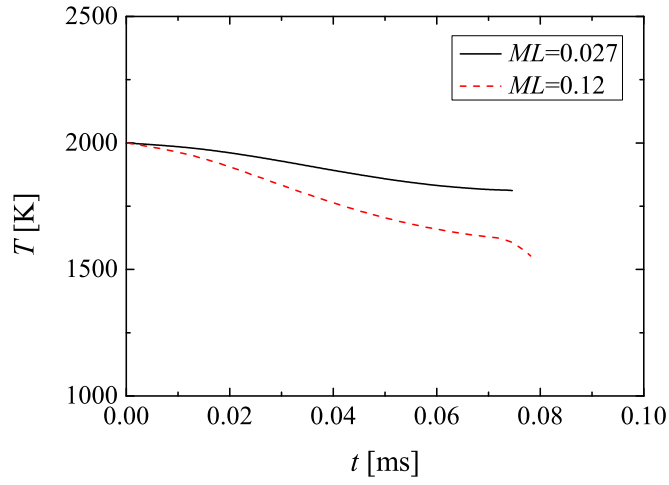


(b) $T_0 = 1500$ K (Cases 2 and 6)

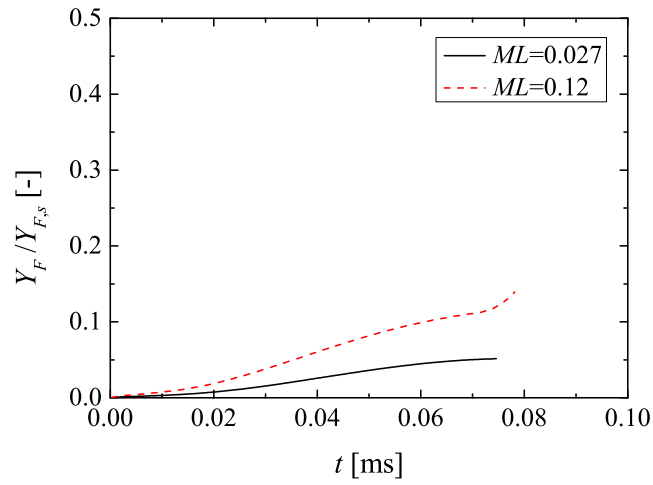


(c) $T_0 = 2000$ K (Cases 3 and 7)

Figure 2.7: Effects of ambient pressure, P , and ML on droplet lifetime in nitrogen at initial gas temperature of $T_0 = 1000$, 1500 , and 2000 K.

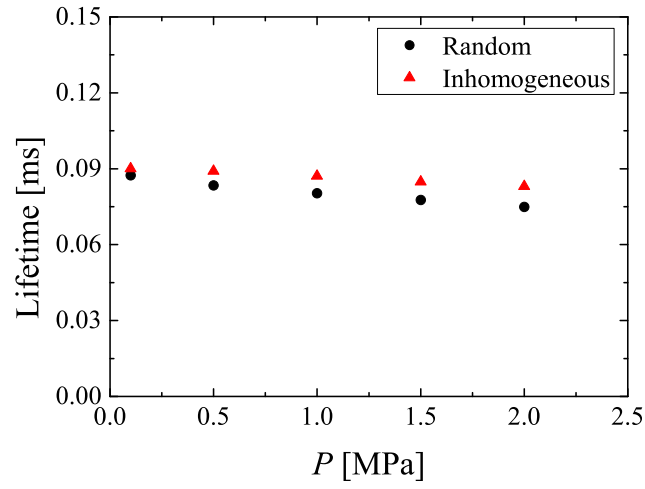


(a) T

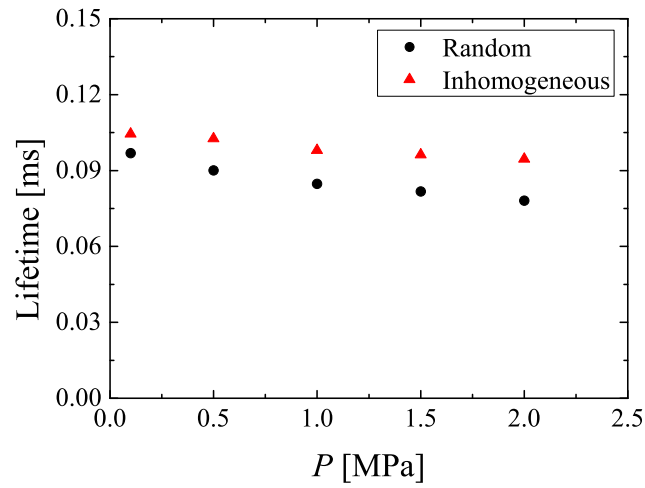


(b) $Y_F/Y_{F,s}$

Figure 2.8: Time variations of gas temperature, T , and ratio of mass fraction of evaporated fuel to vapor surface mass fraction, $Y_F/Y_{F,s}$, in nitrogen at initial gas temperature of $T_0 = 2000$ K and ambient pressure of $P = 2.0$ MPa (see Fig. 2.7(c)).

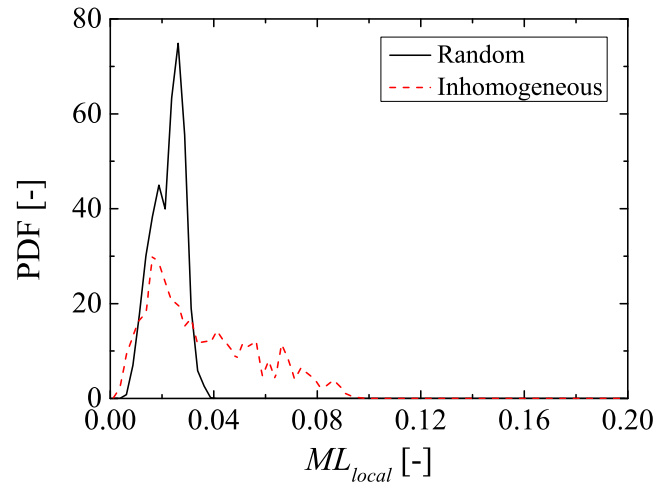


(a) $ML = 0.027$ (without parcel model, Cases 3 and 16)

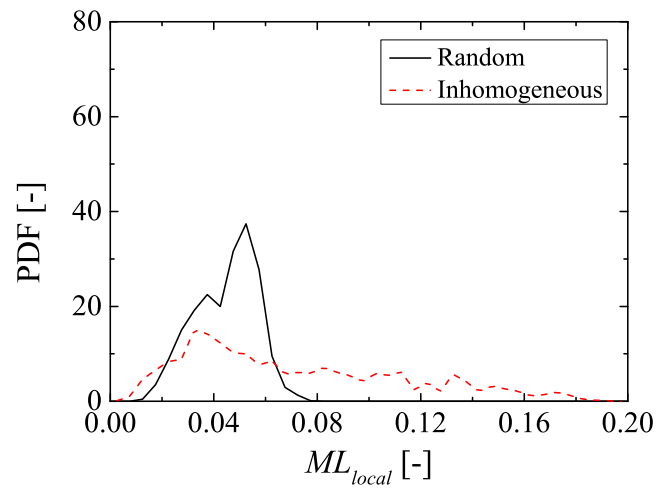


(b) $ML = 0.054$ (with parcel model, Cases 4 and 17)

Figure 2.9: Effect of inhomogeneity of droplet distribution on droplet lifetime in nitrogen at initial gas temperature of $T_0 = 2000$ K for $ML = 0.027$ (without parcel model) and 0.054 (with parcel model).



(a) $ML = 0.027$ (without parcel model, Cases 3 and 16)



(b) $ML = 0.054$ (with parcel model, Cases 4 and 17)

Figure 2.10: Effect of inhomogeneity of droplet distribution on PDF of local mass loading ratio, ML_{local} , in nitrogen at initial gas temperature of $T_0 = 2000$ K and ambient pressure of $P = 2.0$ MPa for $ML = 0.027$ (without parcel model) and 0.054 (with parcel model).

2.2.2.3 Multiple fuel droplets with combustion

Figs. 2.11 and 2.12 show the time variations of the distributions of instantaneous gas temperature, T , mass fraction of O_2 , Y_{O_2} , and mass fraction of fuel gas, Y_F , in air at initial gas temperature of $T_0 = 2000$ K, ambient pressure of $P = 0.1$ MPa, and $ML = 0.12$ and 0.36 , respectively. These conditions are ones in Cases 14 and 15, and indicate the Group combustion number (Eq. (2.37)) of $G = 6.8$ and 20.4 , respectively. It is observed that although the tendencies that Y_{O_2} and Y_F decreases and increases, respectively, in the central region with time are similar between the cases of $ML = 0.12$ and 0.36 , the distributions of T are considerably different. This difference is considered to be in the combustion form, as known as “droplet group combustion”. According to Chiu and Liu [38], and Chiu et al. [39], there are four modes in the droplet group combustion of spray flames: (1) single droplet combustion mode in which all droplets burn with envelope flames, (2) internal group combustion mode in which the group flame appears inside the droplet group (droplets inside the group flame only just evaporate and droplets outside the group flame burn with envelope flames), (3) external group combustion mode in which the group flame encloses the whole droplet group, and (4) external sheath combustion mode in which the nonevaporation region (low-temperature region) is found inside the evaporation region in the droplet group. These modes change from the single droplet combustion mode to the external sheath combustion mode, as the group combustion number, G , increases. Judging from this concept, the combustion behaviors in both cases of $ML = 0.12$ and 0.36 for $P = 0.1$ MPa are considered to be classified into the mode (3), but they seem to be classified into the modes (2) and (3), respectively, from the viewpoint of the physical phenomena. The similar discrepancies were observed in higher ambient pressure conditions, namely the Chiu’s criterion overestimates the group combustion behavior. This is attributed to the fact that the Chiu’s criterion does not consider the effect of the initial oxygen concentration in the droplet group [13, 40].

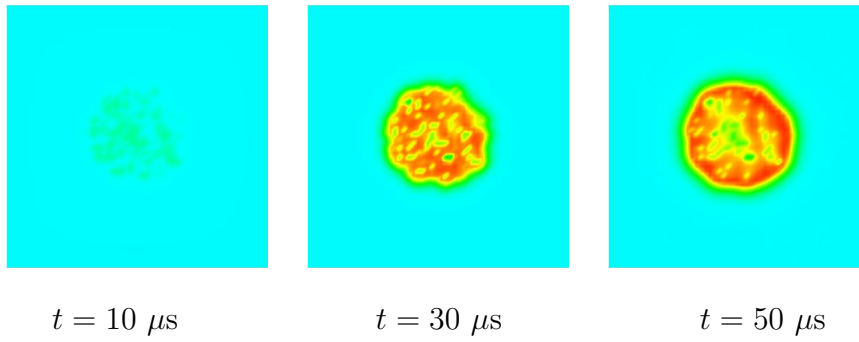
Figs. 2.13, 2.14, and 2.15 show the time variations of total droplet mass, m/m_0 , in air at initial gas temperature of $T_0 = 1000, 1500,$ and 2000 K for $ML = 0.027, 0.12,$ and 0.36 , respectively. Regarding the case of $ML = 0.36$, only the results at $T_0 = 2000$ K

are shown because the combustion reaction did not take place at $T_0 = 1000$ and 1500 K. It is observed that the general tendencies of droplet evaporation are the same as the cases without combustion reaction, namely the start-up of droplet evaporation is delayed and the evaporation rate is enhanced once the evaporation starts as the ambient pressure increases, regardless of the value of ML . However, the droplet evaporation with combustion reaction is faster than that without it. In particular, the droplet evaporation in the cases of higher ambient pressure of $P > 0.1$ MPa are much faster than that in the case of $P = 0.1$ MPa. This is because the increase of the combustion reaction rate with the ambient pressure raises the gas temperature, which enhances the droplet evaporation.

Like the cases without combustion reaction, the effects of ambient pressure, P , and ML on the droplet lifetime in air at initial gas temperature of $T_0 = 1000, 1500,$ and 2000 K are presented in Fig. 2.16. It is verified that the effects of initial gas temperature and ambient pressure on the droplet lifetime are similar to those without combustion reaction, such that the droplet lifetime increases with increasing the ambient pressure at lower initial gas temperature of 1000 K, but decreases at higher initial gas temperature of 1500 and 2000 K. On the other hand, the effect of ML on the droplet lifetime is somewhat complicated. That is, the increase of ML increases the droplet lifetime at $T_0 = 1000$ K, decreases it at $T_0 = 1500$ K, and changes the effect depending on ML (i.e., decreases the droplet lifetime at moderately high ML and conversely increases it at higher ML) at $T_0 = 2000$ K. This is explained by Fig. 2.17 in which the time variations of gas temperature, T , and ratio of mass fraction of evaporated fuel to vapor surface mass fraction, $Y_F/Y_{F,s}$, in air at initial gas temperature of $T_0 = 2000$ K and ambient pressure of $P = 2.0$ MPa (see Fig. 2.16(c)) are shown. It is found that as ML increases, T becomes to rise quickly and $Y_F/Y_{F,s}$ monotonously increases. The trend of T , which is caused by the enhancement of the combustion reaction, is quite different between the cases with and without combustion reaction while that of $Y_F/Y_{F,s}$ is similar. Here the increases of T and $Y_F/Y_{F,s}$ act to enhance and suppress the droplet evaporation, namely shorten and enlarge the droplet lifetime, respectively. Accordingly, it can be said that

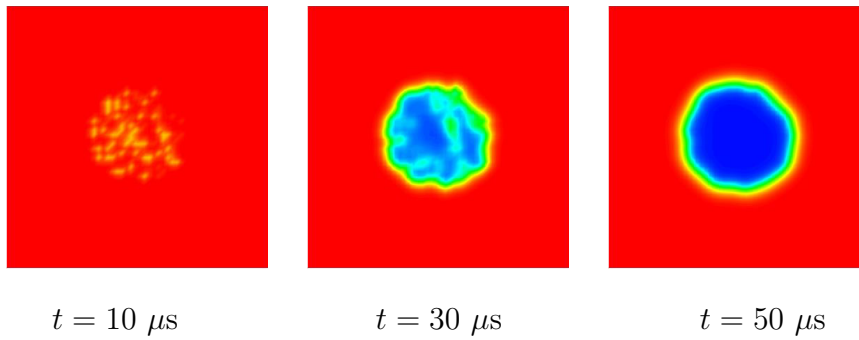
the effect of ML on the droplet lifetime is determined by a balance of the increases of T and $Y_F/Y_{F,s}$. Generally speaking, the droplet lifetime tends to be lengthened by the increase of ML even under the conditions with combustion reaction, but often shortened at moderately high ML at high ambient pressure.

Fig. 2.18 shows the effect of inhomogeneity of the droplet distribution on droplet lifetime in air at initial gas temperature of $T_0 = 2000$ K for $ML = 0.027$ (without parcel model) and 0.054 (with parcel model). In the cases of $ML = 0.054$, the inhomogeneity of the droplet distribution is found to make the droplet lifetime longer regardless of the ambient pressure. In the cases of $ML = 0.027$, on the other hand, the inhomogeneity of the droplet distribution does not always make the droplet lifetime longer. This is due to the same reasons, as mentioned above, that is, the droplet lifetime is shortened by moderately high ML .



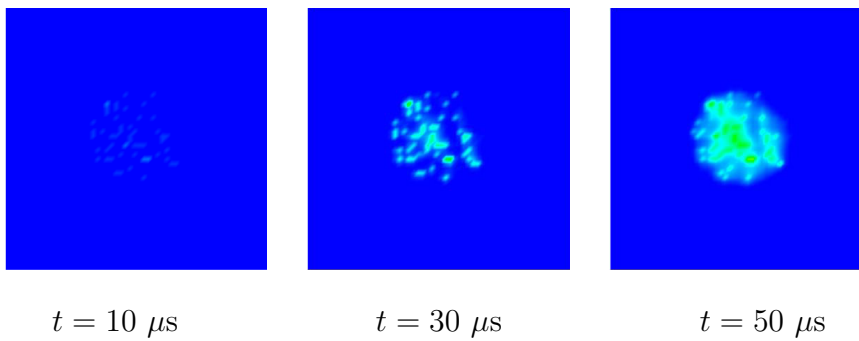
1500 K  3500 K

(a) Gas temperature



0  0.23

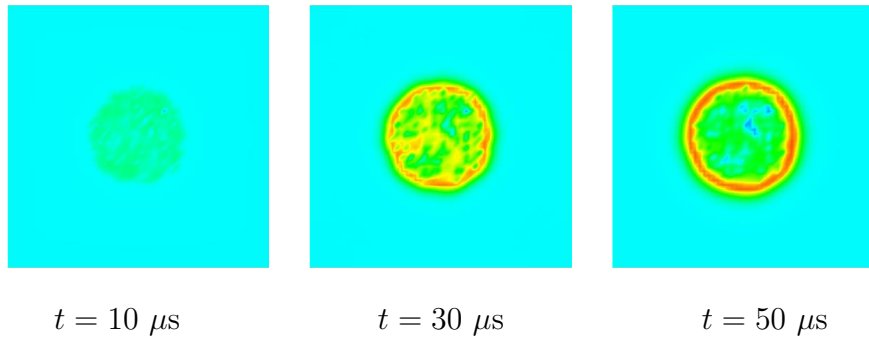
(b) Mass fraction of O_2



0  0.30

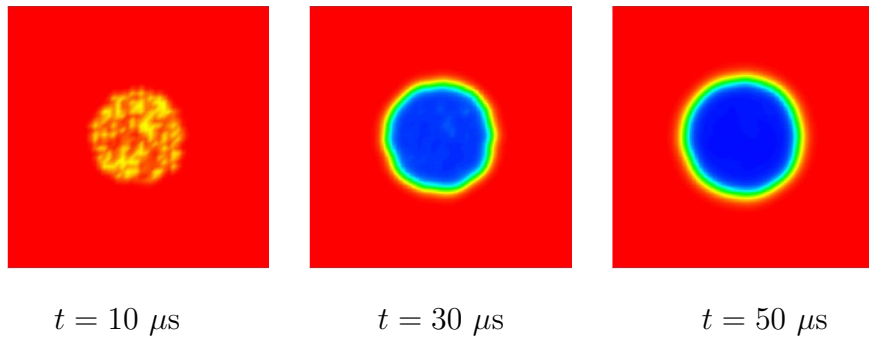
(c) Mass fraction of fuel gas

Figure 2.11: Time variations of distributions of instantaneous gas temperature, T , mass fraction of O_2 , Y_{O_2} , and mass fraction of fuel gas, Y_F , in air at initial gas temperature of $T_0 = 2000$ K, ambient pressure of $P = 0.1$ MPa, and $ML = 0.12$ in Case 14.



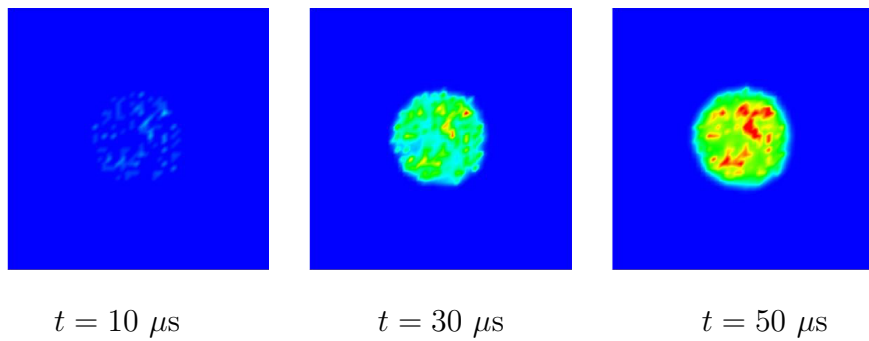
1500 K  3500 K

(a) Gas temperature



0  0.23

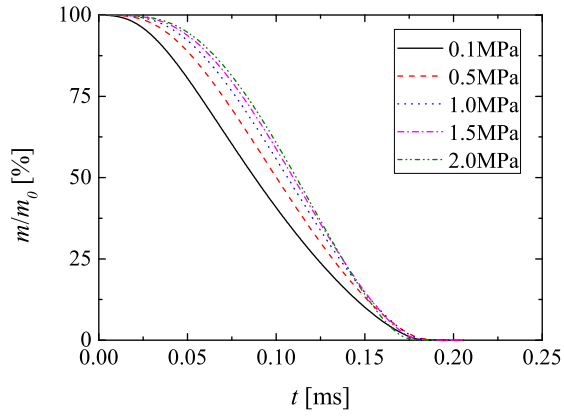
(b) Mass fraction of O_2



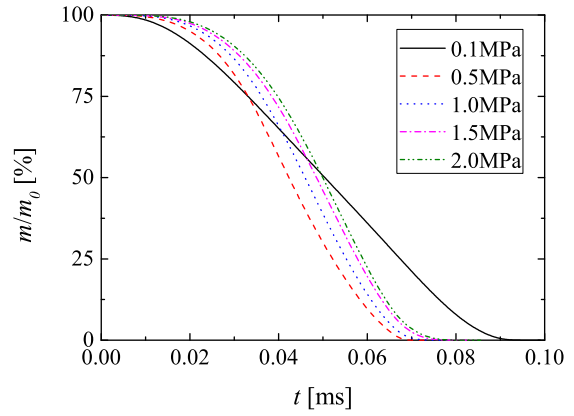
0  0.30

(c) Mass fraction of fuel gas

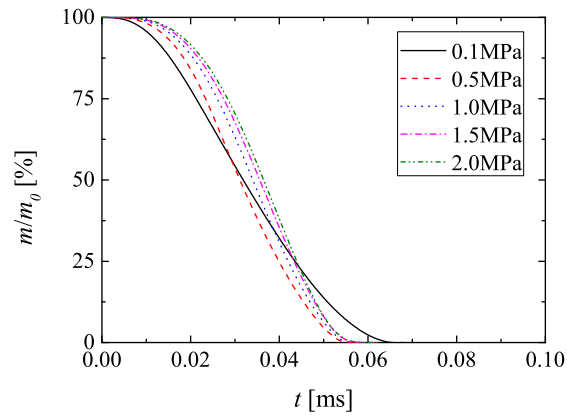
Figure 2.12: Time variations of distributions of instantaneous gas temperature, T , mass fraction of O_2 , Y_{O_2} , and mass fraction of fuel gas, Y_F , in air at initial gas temperature of $T_0 = 2000$ K, ambient pressure of $P = 0.1$ MPa, and $ML = 0.36$ in Case 15.



(a) $T_0 = 1000$ K (Case 8)

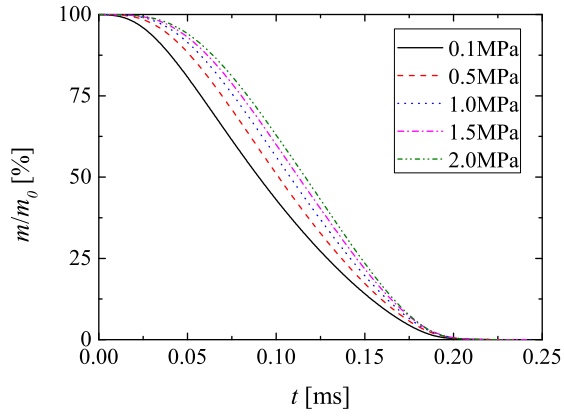


(b) $T_0 = 1500$ K (Case 9)

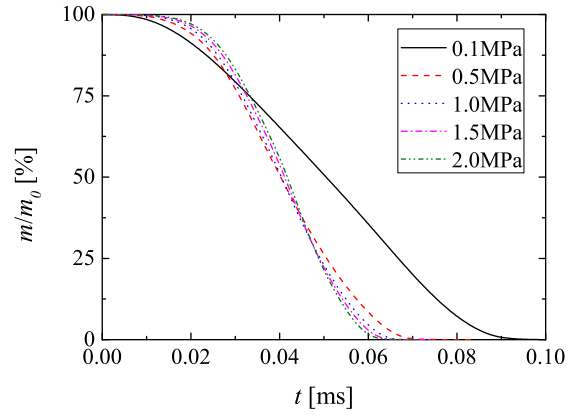


(c) $T_0 = 2000$ K (Case 10)

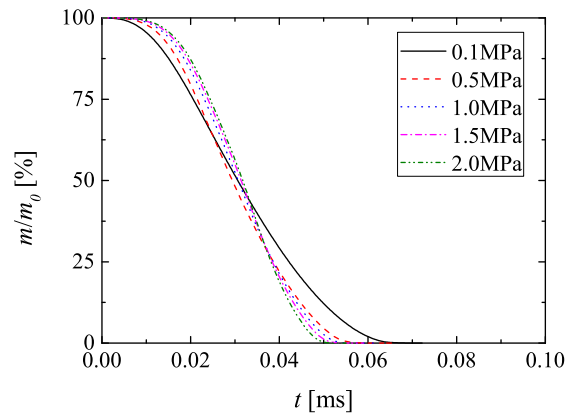
Figure 2.13: Time variations of total droplet mass, m/m_0 , for $ML = 0.027$ in air at initial gas temperature of $T_0 = 1000, 1500,$ and 2000 K.



(a) $T_0 = 1000$ K (Case 12)



(b) $T_0 = 1500$ K (Case 13)



(c) $T_0 = 2000$ K (Case 14)

Figure 2.14: Time variations of total droplet mass, m/m_0 , for $ML = 0.12$ in air at initial gas temperature of $T_0 = 1000, 1500,$ and 2000 K.

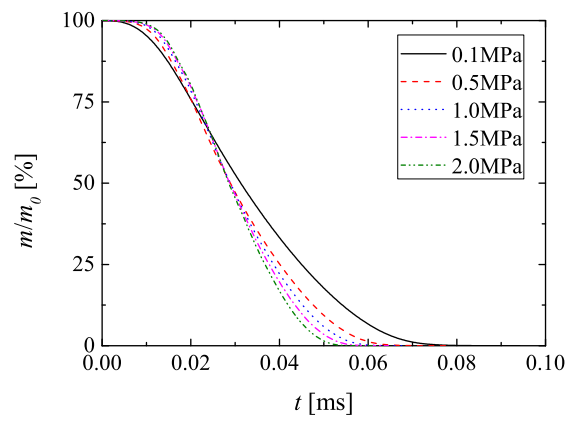
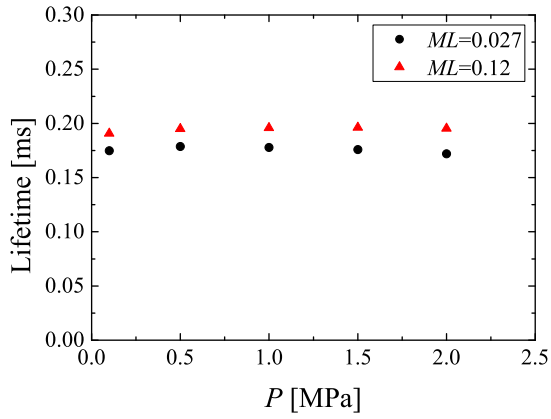
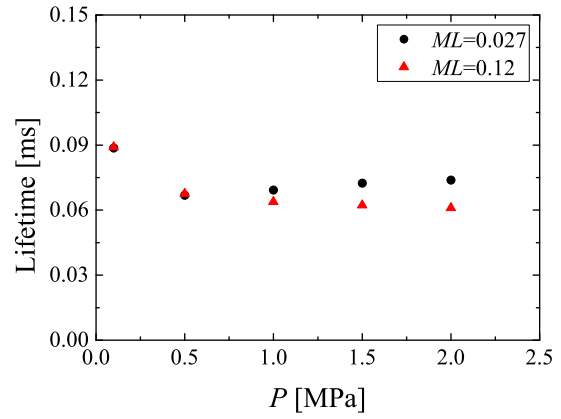


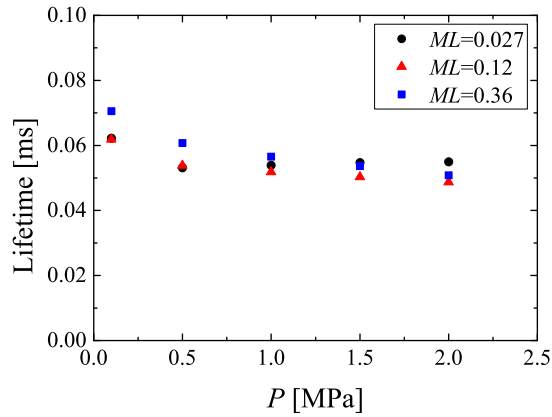
Figure 2.15: Time variations of total droplet mass, m/m_0 , for $ML = 0.36$ in air at initial gas temperature of $T_0 = 2000$ K.



(a) $T_0 = 1000$ K (Cases 8 and 12)

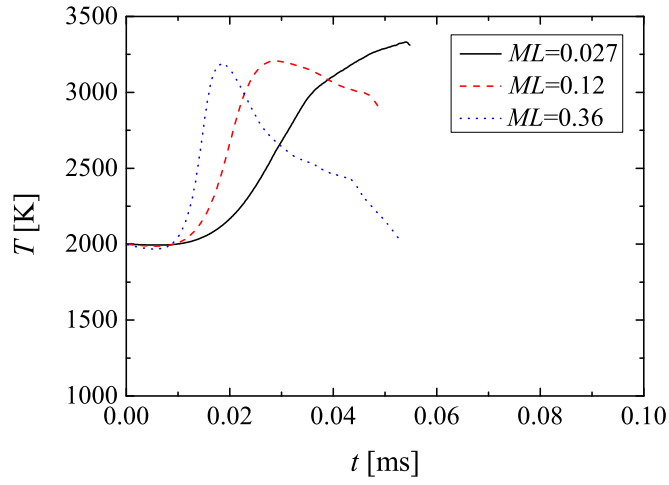


(b) $T_0 = 1500$ K (Cases 9 and 13)

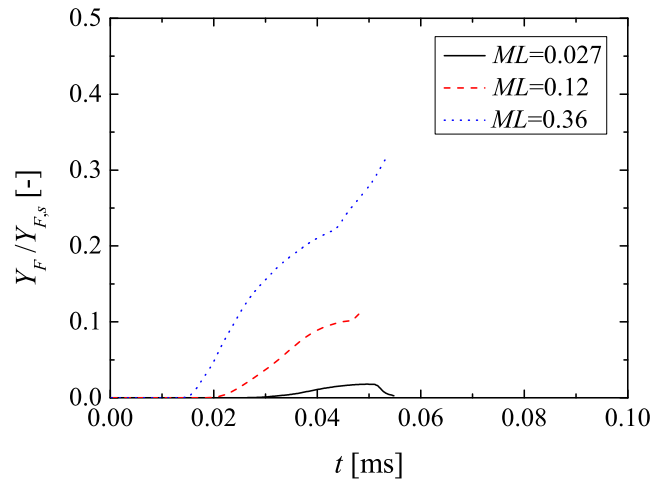


(c) $T_0 = 2000$ K (Cases 10, 14 and 15)

Figure 2.16: Effects of ambient pressure, P , and ML on droplet lifetime in air at initial gas temperature of $T_0 = 1000$, 1500 , and 2000 K.

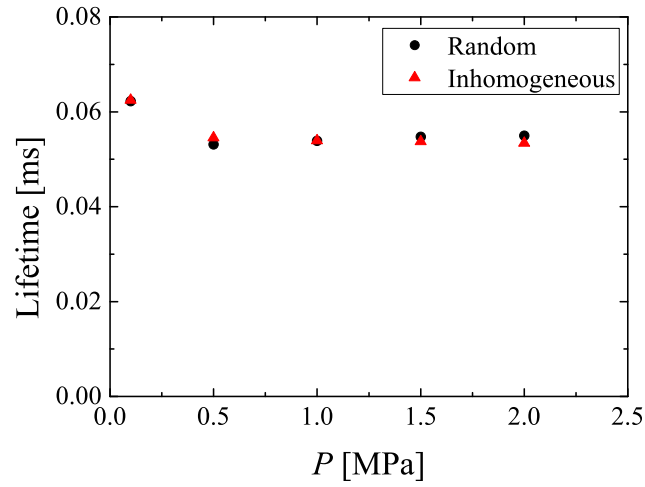


(a) T

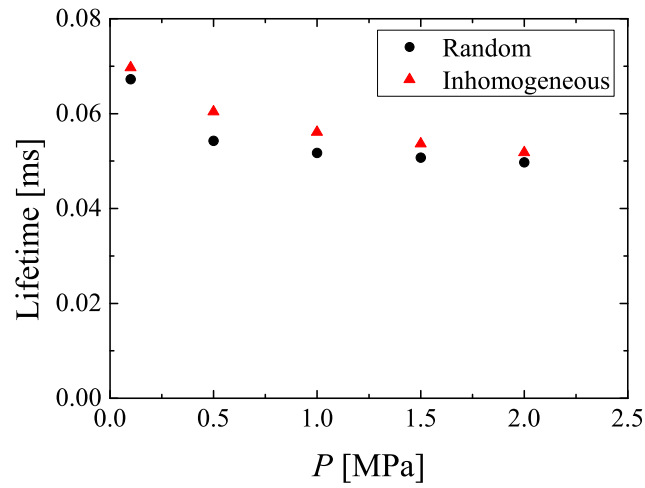


(b) $Y_F/Y_{F,s}$

Figure 2.17: Time variations of gas temperature, T , and ratio of mass fraction of evaporated fuel to vapor surface mass fraction, $Y_F/Y_{F,s}$, in air at initial gas temperature of $T_0 = 2000$ K and ambient pressure of $P = 2.0$ MPa (see Fig. 2.16(c)).



(a) $ML = 0.027$ (without parcel model, Cases 10 and 18)



(b) $ML = 0.054$ (with parcel model, Cases 11 and 19)

Figure 2.18: Effect of inhomogeneity of droplet distribution on droplet lifetime in air at initial gas temperature of $T_0 = 2000$ K for $ML = 0.027$ (without parcel model) and 0.054 (with parcel model).

2.3 Multi-component fuel droplet

2.3.1 Numerical Simulation

2.3.1.1 Evaporation model

The governing equations for the gas and dispersed-droplets phases, and the numerical procedure are the same as those for the single-component fuel droplet described in the previous section. Multi-component evaporation is taken into account using the discrete multi-component method [41, 42], in which each component individually evaporates according to its volatility. It is assumed that the entire evaporation rate of a multi-component fuel is calculated in an analogous way to that of a single-component fuel.

The entire evaporation rate of a multi-component fuel, \dot{m}_d , is expressed as

$$\dot{m}_d = -\frac{m_d}{\tau_d} \left(\frac{Sh}{3Sc} \right) \ln(1 + B_M), \quad (2.43)$$

$$B_M = \frac{\sum_k Y_{V,s,k} - \sum_k Y_{V,k}}{1 - \sum_k Y_{V,s,k}}, \quad (2.44)$$

$$\tau_d = \frac{\rho_d d^2}{18\mu}, \quad (2.45)$$

$$Sc = \frac{\mu}{\rho \sum_k Y_{V,k} D_k}, \quad Sh = 2 + 0.552 Re_{sl}^{1/2} Sc^{1/3}. \quad (2.46)$$

Here Sc is the averaged Schmidt number, Sh the averaged Sherwood number, B_M the mass transfer number, τ_d the particle response time, $Y_{V,k}$ the vapor mass fraction of species k , ρ_d the density of a liquid fuel, d the droplet diameter, and μ the viscosity of gas, respectively. $Re_{sl} = \rho u_{sl} d / \mu$ is the Reynolds number based on the slip velocity.

$Y_{V,s,k}$ is the surface vapor mass fraction of species k calculated as

$$Y_{V,s,k} = \frac{X_{V,s,k}}{X_{V,s,k} + (1 - X_{V,s,k}) \bar{W} / W_{V,k}}, \quad (2.47)$$

$$X_{V,s,k} = X_{k,d} \frac{P_{sat,k}}{P} - \left(\frac{2L_K}{d} \right) \beta. \quad (2.48)$$

Here $X_{V,s,k}$ is the surface vapor mole fraction of species k , $X_{k,d}$ the mole fraction of the fuel in the liquid phase, P the ambient pressure, \bar{W} the averaged mole weight, and

$W_{V,k}$ the mole weight of species k , respectively. $P_{sat,k}$ is the saturated vapor pressure calculated using Sato's empirical equation (Eq. (2.33)) [26]. L_K and β are the Knudsen layer thickness of species k and the non-dimensional constant calculated as

$$L_K = \frac{\mu \{2\pi T_d (R/W_{V,k})\}^{1/2}}{ScP}, \quad (2.49)$$

$$\beta = - \left(\frac{\rho_d Pr}{8\mu} \right) \frac{dd^2}{dt}, \quad (2.50)$$

respectively. Here T_d is the droplet temperature, Pr the Prandtl number and R the universal gas constant, respectively.

The evaporation rate of species k , $\dot{m}_{d,k}$, is calculated as

$$\dot{m}_{d,k} = \varepsilon_k \dot{m}_d. \quad (2.51)$$

Here ε_k is the non-dimensional partial evaporation rate calculated as follows [41, 42]. The conservation equation of each component around the droplet leads another form of \dot{m}_d , which is expressed by using properties of species k as

$$\dot{m}_d = - \frac{m_d}{\tau_d} \left(\frac{Sh_k}{3Sc_k} \right) \ln(1 + B_{M,k}), \quad (2.52)$$

$$B_{M,k} = \frac{Y_{V,s,k} - Y_{V,k}}{\varepsilon_k - Y_{V,s,k}}, \quad (2.53)$$

$$Sc_k = \frac{\mu}{\rho D_k}, \quad Sh_k = 2 + 0.552 Re_{sl}^{1/2} Sc_k^{1/3}. \quad (2.54)$$

Here $B_{M,k}$ is the mass transfer number of species k , Sh_k the Sherwood number of species k , and Sc_k the Schmidt number of species k . From Eqs. (2.43) and (2.52), the relationship between B_M and $B_{M,k}$ is written as

$$B_{M,k} = (1 + B_M)^{\eta_k} - 1, \quad \eta_k = \frac{Sh Sc_k}{Sh_k Sc}. \quad (2.55)$$

From Eqs. (2.44), (2.53), and (2.55) with the assumption of $\eta_k = 1$ (unity Lewis number assumption), ε_k is calculated as

$$\varepsilon_k = Y_{V,s,k} + (Y_{V,s,k} - Y_{V,k}) \frac{1 - \sum_k Y_{V,s,k}}{\sum_k Y_{V,s,k} - \sum_k Y_{V,k}}. \quad (2.56)$$

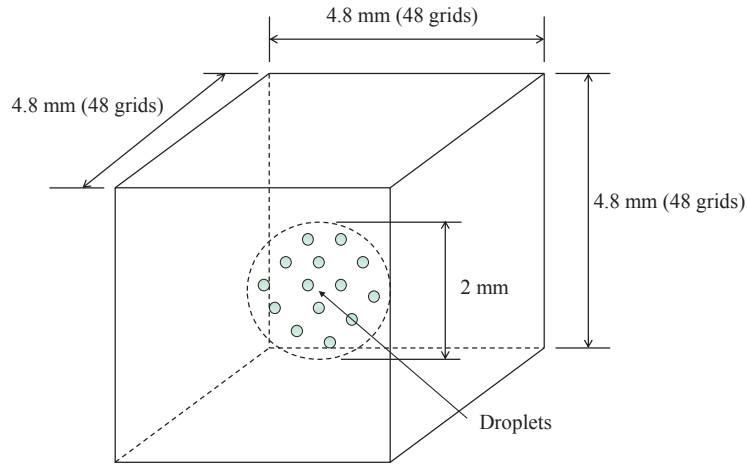


Figure 2.19: Computational domain.

2.3.1.2 Reaction model

As the fuels, the surrogate fuels of Jet-A (one-component fuel: *n*-decane, two-component fuel: *n*-decane and 1,2,4-trimethyl-benzene [9], three-component fuel: *n*-dodecane, *iso*-octane, and toluene [10–12]) are used. For the calculations of the reactions, the detailed reaction models that consider 113 chemical species and 891 reactions for the one- and two-component fuels [9], and 273 chemical species and 2322 reactions for the three-component fuel [10–12] are used, respectively.

2.3.1.3 Computational details

Fig. 2.19 shows the schematic of the computational domain. The computational domain is a cube 4.8 mm on a side and divided into 48 uniform computational grid points in the each direction. The staggered grid is used for the computational grid. To remove grid resolution dependence, source terms for gas phase are calculated for cells surrounding an each droplet by using a distance function from the droplet position [43].

The computations are performed for the evaporation of the single fuel droplet and for the evaporation/combustion reaction of multiple fuel droplets. Initially, the single

fuel droplet and multiple fuel droplets are allocated at the center of the computational domain and in the central region as the spherical shape with 2 mm diameter, respectively. The equivalence ratio in the central region is 2.0 for multiple fuel droplets. The initial droplet diameters are set to 1.33 mm for the single fuel droplet, and 7.5 and 15 μm for the multiple fuel droplets. These droplet sizes are decided to compare with the experiments [5] and to meet the requirement associate with the grid size from the point of view of numerical accuracy, respectively (the grid spacing needs to be roughly 10 times larger than the droplet size [27]). The initial gas and droplet temperature are 1500 and 300 K, respectively.

Table 2.2 lists the computational conditions performed for the evaporation and combustion reaction of the multiple fuel droplets. The ambient pressure, P , is set to 0.1 MPa and 1.0 MPa. In order to investigate the effects of the combustion reaction, the computations are carried out for different mediums of the ambient gas (i.e., nitrogen and air). Physical properties of each component are listed in Table 2.3. In this table, the latent heat, L_V , is the value at the normal boiling point and the specific heat capacity, c_p , and density, ρ , are the values in the standard condition.

For a numerical approximation of the gas phase, discretization of the nonlinear terms of the momentum equations is derived from the second-order fully conservative finite difference scheme [30, 31]. For the convection terms of the energy and mass fractions of chemical species, the QUICK scheme [32] is employed. Other differentials are approximated by the second-order finite difference method. The third-order explicit Runge–Kutta method is used for the time advancement calculation of the convective terms. The fractional step method [33] is used as the computational algorithm. The Variable-coefficient ODE solver (VODE) [44] is applied to the calculation of the chemical reactions described above. On all six boundaries, the free outflow condition is given.

The values of the droplet density, ρ_d , and the specific heat capacity of the droplet, $c_{p,d}$, are calculated by the curve fit data from the NIST web book [24], and the other thermophysical properties and transport coefficients under various pressures are obtained from CHEMKIN [34, 35].

The CPU time for the heaviest case (Case 9) is about 6400 h (100 h on the wall-clock time) on SGI Altix ICE (Intel Xeon X5560 processor, 64 cores).

2.3.2 Results and discussion

2.3.2.1 Single fuel droplet without combustion

In this section, the present evaporation model is validated by comparing with the experiment by Daïf et al. [5]. In this experiment [5], an *n*-decane ($C_{10}H_{22}$)/*n*-heptane (C_7H_{16}) multi-component droplet is suspended in a hot air flow whose average velocity is 3.1 m/s and the temperature is 348 K. The initial droplet diameter is 1.33 mm and the initial droplet temperature is equal to the room temperature. In the calculation, the composition of the droplet is changed. Namely, the compositions of the droplets of Cases A and D, Case B, and Case C are *n*-decane/*n*-heptane (26%/74%), *n*-heptane (100%) and *n*-decane (100%), respectively. In addition, the physical properties of individual components are considered in Case A, whereas the droplet is treated as a one-component fuel in which averaged physical properties are used in Case D.

Fig. 2.20 shows the comparison of the predicted time variations of the squared droplet diameter, d^2 , with the experiment [5]. It is shown that the decreasing rate in the experiment [5] changes at around $t = 7.0$ s. This is because *n*-heptane mainly evaporates before at around $t = 7.0$ s and *n*-decane mainly evaporates after that. It is found that Case A correctly predicts this change of the decreasing rate, and the curve trend agrees well with the experiment [5]. On the other hand, Case D cannot predict this change of the decreasing rate especially after at around $t = 7.0$ s, and Cases B and C fail to predict the experiment [5]. Therefore, the model in Case A is employed for the computations in the following sections.

2.3.2.2 Multiple fuel droplets without combustion

Fig. 2.21 shows the time variations of the normalized masses of gas and liquid fuels, m_g/m_0 and m_l/m_0 , in nitrogen for $P = 0.1$ MPa and $d_0 = 15.0$ μm for the one-, two-,

Table 2.2: Computational conditions.

Cases	P [MPa]	d_0 [μm]	Ambient gas	Fuel
1	0.1	15.0	Nitrogen	One-component fuel
2	0.1	15.0	Nitrogen	Two-component fuel
3	0.1	15.0	Nitrogen	Three-component fuel
4	0.1	15.0	Air	One-component fuel
5	0.1	15.0	Air	Two-component fuel
6	0.1	15.0	Air	Three-component fuel
7	1.0	15.0	Air	One-component fuel
8	1.0	15.0	Air	Two-component fuel
9	1.0	15.0	Air	Three-component fuel
10	0.1	7.5	Air	One-component fuel
11	0.1	7.5	Air	Two-component fuel
12	0.1	7.5	Air	Three-component fuel

Table 2.3: Physical properties.

Components	T_c [K]	T_{nb} [K]	$L_{V,nb}$ [kJ/kg]	c_p [J/(K kg)]	ρ [kg/m ³]	W [g/mol]
<i>n</i> -Decane	619.0	447.3	279.7	2199.8	724.7	142.3
<i>n</i> -Heptane	540.0	371.6	317.1	2232.5	679.4	100.2
1,2,4-Trimethyl-benzene	654.7	442.6	398.8	1773.0	872.2	120.2
<i>n</i> -Dodecane	658.2	489.0	256.5	2218.3	744.4	170.3
<i>iso</i> -Octane	543.9	372.4	269.5	2045.9	690.0	114.2
Toluene	593.0	383.8	360.1	1707.0	860.51	92.1

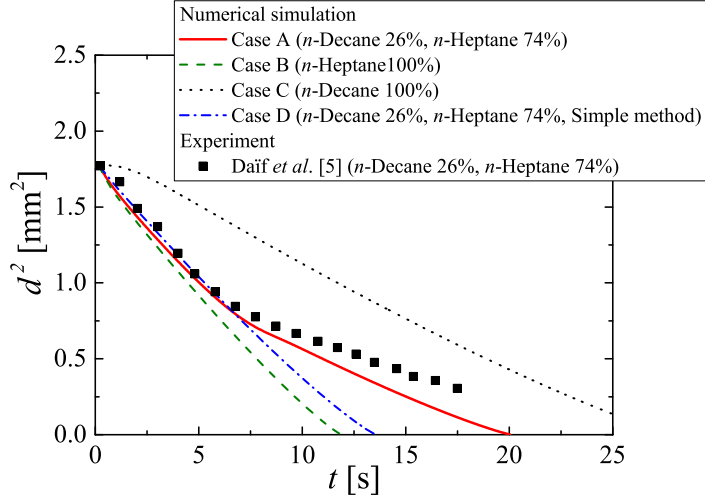


Figure 2.20: Comparison of predicted time variations of squared droplet diameter, d^2 , with experiment.

and three-component fuels (Cases 1–3). In these cases, the evaporation and pyrolysis occur without combustion reaction. It is found that the evaporation rate in Case 3 (three-component fuel) is higher and lower than those in the other cases before and after at $t = 0.1$ ms, respectively. This is due to the fact that compared to *n*-decane and 1,2,4-trimethyl-benzene, *iso*-octane and toluene included in the three-component fuel have higher volatilities, whereas *n*-dodecane included in the three-component fuel has lower volatility. In all cases, the amount of gas fuel decreases after around 0.5 ms. This is because the pyrolysis rate overcomes the evaporation rate. Fig. 2.22 shows the radial distributions of the space-averaged gas temperature, T , in nitrogen for $P = 0.1$ MPa and $d_0 = 15.0$ μm for the one-, two-, and three-component fuels (Cases 1–3). In all cases, the gas temperature decrease with time due to the latent heat of evaporation and heat transferred into the droplets. The gas temperature in Case 3 (three-component fuel) is found to be lower than those in the other cases at earlier periods of $t = 0.125$ and 0.200 ms. This is due to the facts that evaporation in Case 3 (three-component fuel) is faster than those in the other cases as shown in Fig. 2.21, and that *iso*-octane and toluene of the three-component fuel have larger latent heat than that of *n*-decane.

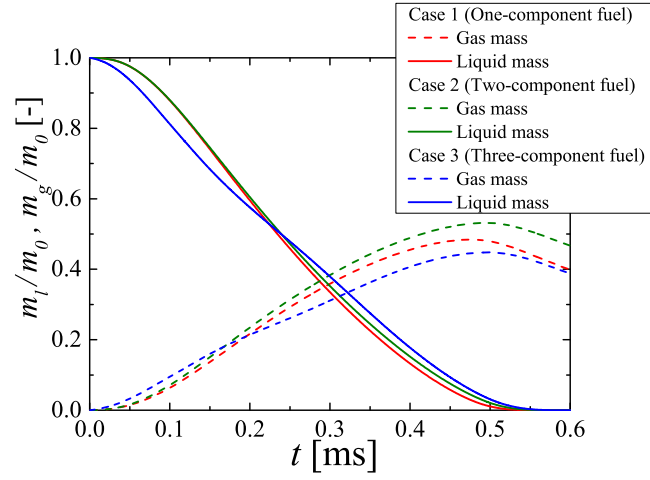


Figure 2.21: Time variations of normalized masses of gas and liquid fuels, m_g/m_0 and m_l/m_0 , in nitrogen for $P = 0.1$ MPa and $d_0 = 15.0$ μm for one-, two-, and three-component fuels (Cases 1–3).

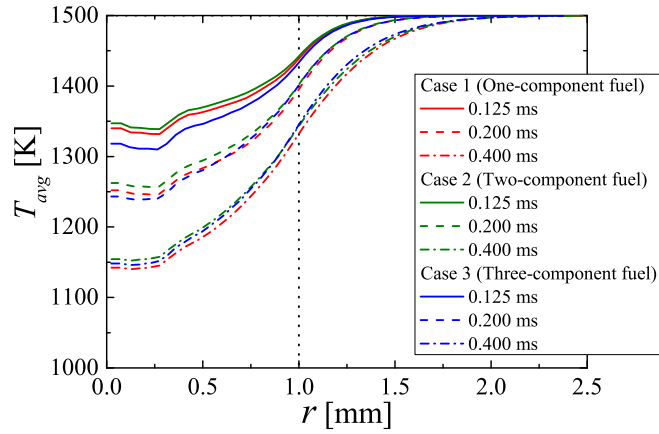


Figure 2.22: Radial distributions of space-averaged gas temperature, T , in nitrogen for $P = 0.1$ MPa and $d_0 = 15.0$ μm for one-, two-, and three-component fuels (Cases 1–3).

2.3.2.3 Multiple fuel droplets with combustion

Fig. 2.23 shows the typical behavior of the droplet evaporation and combustion, namely, the instantaneous distributions of gas temperature, T , and mass fractions of chemical species, Y_{O_2} , Y_{CO} , Y_{CO_2} , and Y_{OH} , in air for $P = 0.1$ MPa and $d_0 = 15.0$ μm at $t = 0.125$, 0.200 , and 0.400 ms for the one-component fuel (Case 4). It is observed that the gas temperature increases with time by combustion and O_2 is consumed, and that the combustion products and radicals such as CO , CO_2 , and OH are generated.

Fig. 2.24 shows the time variations of the normalized masses of gas and liquid fuels, m_g/m_0 and m_l/m_0 , in air for the one-, two-, and three-component fuels for $P = 0.1$ MPa and $d_0 = 15.0$ μm (Cases 4–6), $P = 1.0$ MPa and $d_0 = 15.0$ μm (Cases 7–9), and $P = 0.1$ MPa and $d_0 = 7.5$ μm (Cases 10–12). In Fig. 2.24(a), it is found that the evaporation rate in Case 6 (three-component fuel) is higher and lower than those in Cases 4 (one-component fuel) and 5 (two-component fuel) before and after at $t = 0.1$ ms, respectively. This is due to the same reason as mentioned earlier. Namely, compared to *n*-decane and 1,2,4-trimethyl-benzene, *iso*-octane, and toluene included in the three-component fuel have higher volatilities, whereas *n*-dodecane included in the three-component fuel has lower volatility.

The comparisons of Fig. 2.24(a) with (b) and (c) show that the differences in the evaporation rate observed between the three-component fuel, and the one- and two-component fuels for $P = 0.1$ MPa and $d_0 = 15.0$ μm still exist for $P = 1.0$ MPa, but disappear for $d_0 = 7.5$ μm . This suggests that the effects of the droplet composition on the evaporation rate do not depend on the ambient pressure very much, but the effects become remarkable with increasing the droplet size.

Fig. 2.25 shows the radial distributions of the space-averaged gas temperature, T , in air for the one-, two-, and three-component fuels for $P = 0.1$ MPa and $d_0 = 15.0$ μm (Cases 4–6), $P = 1.0$ MPa and $d_0 = 15.0$ μm (Cases 7–9), and $P = 0.1$ MPa and $d_0 = 7.5$ μm (Cases 10–12). For all pressure and initial-droplet-diameter conditions, the differences in the gas temperature among the one-, two-, and three-component fuels are observed to be marked initially and become small with time. Also, the trends of the

differences in the gas temperature among the one-, two-, and three-component fuels are found to be different for the each pressure and initial-droplet-diameter condition. In Fig. 2.25(b), the gas temperature in Case 9 (three-component fuel) is higher than those in Cases 7 (one-component fuel) and 8 (two-component fuel) at $t = 0.125$ ms. This is due to the fact that the evaporation rate in Case 9 (three-component fuel) is higher than those in Cases 7 (one-component fuel) and 8 (two-component fuel) as shown in Fig. 2.24(b), and therefore, the higher concentration of the evaporated fuel accelerates the combustion reaction.

On the other hand, in Fig. 2.25(a), the gas temperature not only in Case 6 (three-component fuel) but also in Case 4 (one-component fuel) indicates the higher value than that in Case 5 (two-component fuel) at $t = 0.125$ ms. This is because the ignition delay time of the one-component fuel is shorter than that of the two-component fuel. The reason why the gas temperature of the one-component fuel is not higher than that of the two-component fuel in the case of $P = 1.0$ MPa (Fig. 2.25(b)) is considered to be that since the ignition delay time becomes much shorter due to the higher combustion reaction rate, the difference in the ignition delay time does not affect the difference in the time variation of the gas temperature very much.

It is found in Fig. 2.25(c) that the trend of the differences in the gas temperature among the one-, two-, and three-component fuels is different from those in the other pressure and initial-droplet-diameter conditions. Namely, the gas temperature in Case 10 (one-component fuel) and Case 12 (three-component fuel) are highest and lowest at $t = 0.125$ ms, respectively. This is due to the fact that in the cases of small droplets, the time variation of the gas temperature mainly depends on the ignition delay time because the evaporation of the small droplets is fast and the difference in the evaporation rate is small as shown in Fig. 2.24(c).

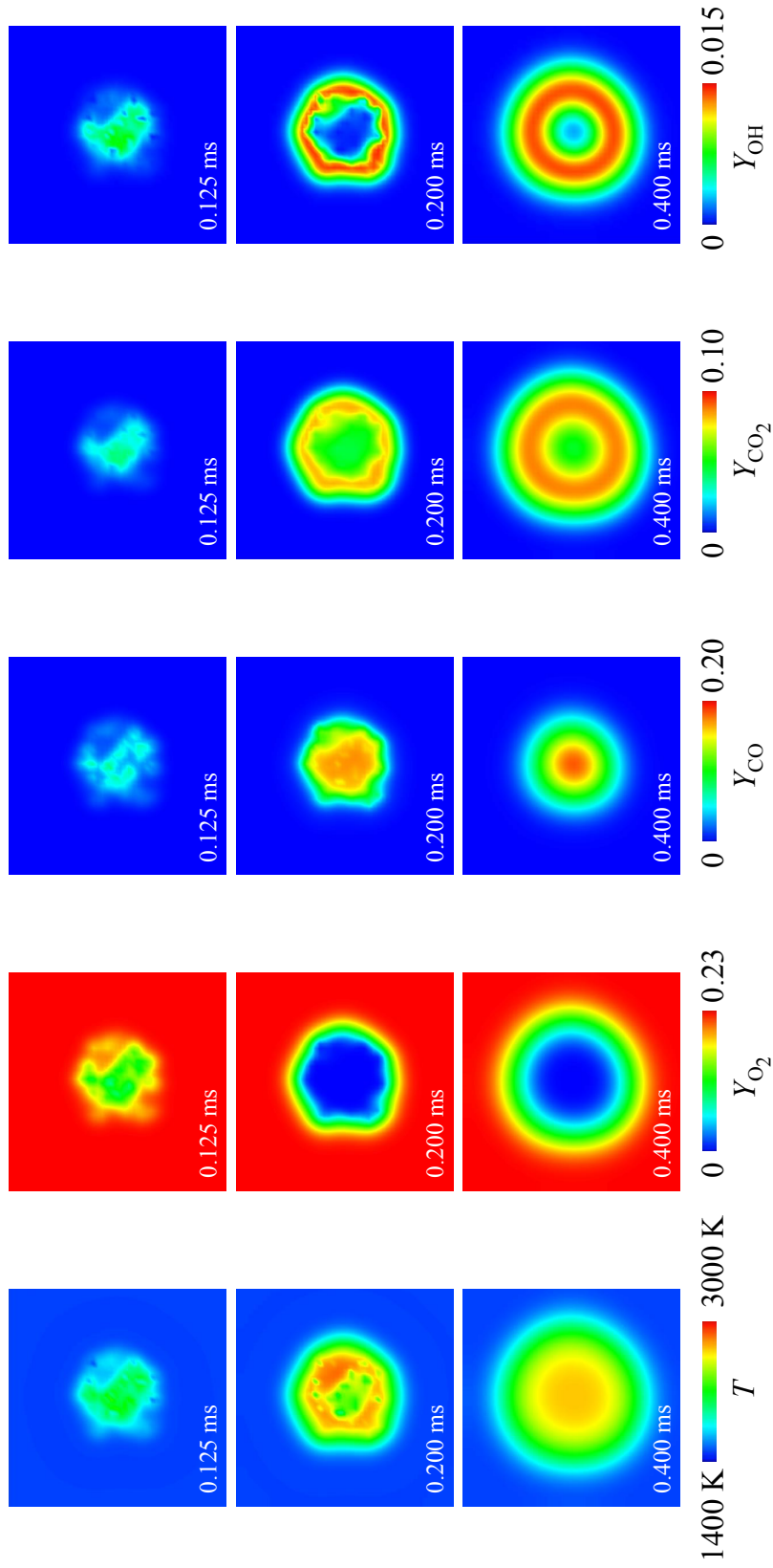
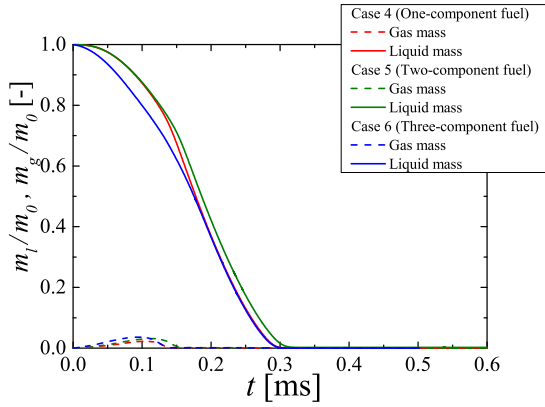
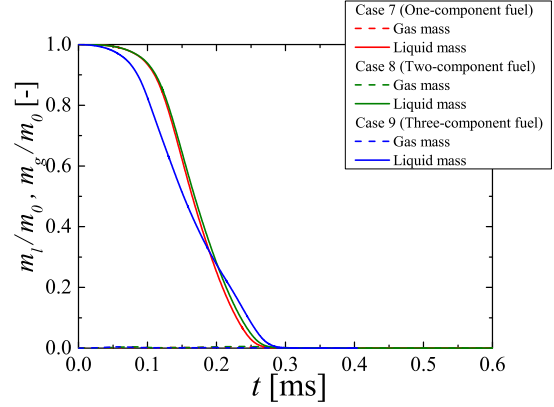


Figure 2.23: Instantaneous distributions of gas temperature, T , and mass fractions of chemical species, Y_{O_2} , Y_{CO} , Y_{CO_2} , and Y_{OH} , in air for $P = 0.1$ MPa and $d_0 = 15.0 \mu\text{m}$ at $t = 0.125$, 0.200 , and 0.400 ms for a one-component fuel (Case 4).



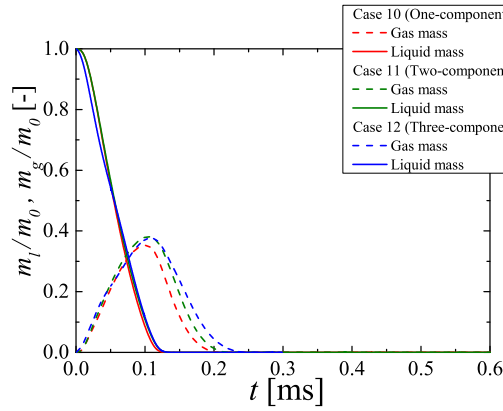
(a) $P = 0.1$ MPa, $d_0 = 15.0 \mu\text{m}$

(Cases 4–6)



(b) $P = 1.0$ MPa, $d_0 = 15.0 \mu\text{m}$

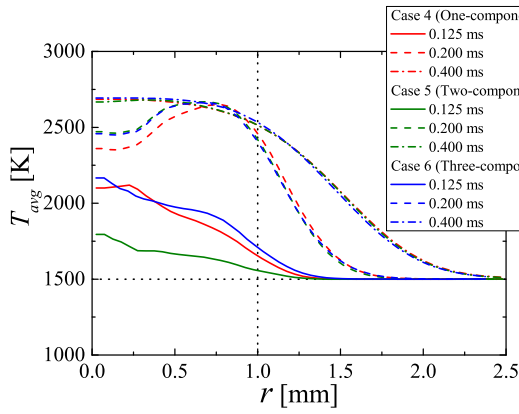
(Cases 7–9)



(c) $P = 0.1$ MPa, $d_0 = 7.5 \mu\text{m}$

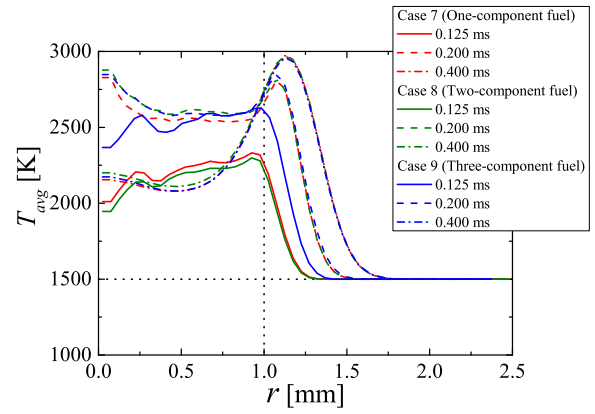
(Cases 10–12)

Figure 2.24: Time variations of normalized masses of gas and liquid fuels, m_g/m_0 and m_l/m_0 , in air for one-, two-, and three-component fuels for $P = 0.1$ MPa and $d_0 = 15.0 \mu\text{m}$ (Cases 4–6), $P = 1.0$ MPa and $d_0 = 15.0 \mu\text{m}$ (Cases 7–9), and $P = 0.1$ MPa and $d_0 = 7.5 \mu\text{m}$ (Cases 10–12).



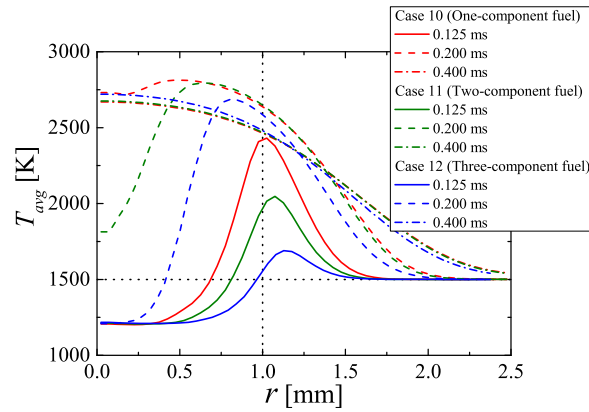
(a) $P = 0.1$ MPa, $d_0 = 15.0$ μm

(Cases 4–6)



(b) $P = 1.0$ MPa, $d_0 = 15.0$ μm

(Cases 7–9)



(c) $P = 0.1$ MPa, $d_0 = 7.5$ μm

(Cases 10–12)

Figure 2.25: Radial distributions of space-averaged gas temperature, T , in air for one-, two-, and three-component fuels for $P = 0.1$ MPa and $d_0 = 15.0$ μm (Cases 4–6), $P = 1.0$ MPa and $d_0 = 15.0$ μm (Cases 7–9), and $P = 0.1$ MPa and $d_0 = 7.5$ μm (Cases 10–12).

2.4 Conclusions

In this study, the effects of ambient pressure, initial gas temperature, and differences in fuel components and combustion reaction on the evaporation of a single and multiple fuel droplets were investigated using DNS. The main results obtained in this study can be summarized as follows.

1. Natural convection accelerates droplet evaporation, and the effect becomes remarkable with increasing the ambient pressure.
2. Under the conditions without combustion reaction, droplet lifetime increases with increasing the ambient pressure at lower initial gas temperature but decreases at higher initial gas temperature. This is attributed to a balance of the increase and decrease of droplet evaporation rate in higher ambient pressure conditions. Namely, as the ambient pressure increases, droplet evaporation is suppressed by higher boiling temperature, whereas it is enhanced by lower latent heat and larger droplet surface due to greater liquid expansion caused by the increase of droplet temperature. This tendency is not influenced by ML , but the droplet lifetime quantitatively becomes longer with increasing ML because of the decrease of gas temperature and the increase of the evaporated fuel mass fraction toward the vapor surface mass fraction.
3. The effects of ambient pressure, initial gas temperature, and ML on the droplet lifetime under the condition with combustion reaction are similar to those under the conditions without combustion reaction, although the droplet lifetime becomes shorter due to the combustion reaction. However, the droplet lifetime is often shortened by enhanced combustion reaction in the conditions of high ambient pressure and moderately high ML .
4. Both for the conditions with and without combustion reaction, inhomogeneity of droplet distribution caused by turbulence makes the droplet lifetime longer because local ML increases in some locations.

5. The multi-component droplet evaporation model which considers each component's physical properties such as the boiling point and saturated vapor pressure individually precisely predicts the change in the decreasing rate of droplet diameter, compared to the evaporation model that uses the averaged values of the components.

6. Evaporation of the three-component surrogate fuel of Jet-A becomes faster and slower than those of the one- and two-component surrogate fuels in the initial and subsequent evaporating periods, respectively. This is due to the fact that compared to *n*-decane and 1,2,4-trimethyl-benzene, *iso*-octane and toluene included in the three-component surrogate fuel have higher volatilities, whereas *n*-dodecane included in the three-component fuel has lower volatility. Differences in the gas temperature evolution among three different surrogate fuels are remarkable right after the ignition, but they become small with time.

References

- [1] R. S. Miller and J. Bellan. Direct numerical simulation of a confined three-dimensional gas mixing layer with one evaporating hydrocarbon-droplet-laden stream. *Journal of Fluid Mechanics*, 384:293–338, 1999.
- [2] H. Nomura, Y. Ujiie, H. J. Rath, J. Sato, and M. Kono. Experimental study on high-pressure droplet evaporation using microgravity conditions. *Symposium (International) on Combustion*, 26(1):1267–1273, 1996.
- [3] J.-R. Yang and S.-C. Wong. On the discrepancies between theoretical and experimental results for microgravity droplet evaporation. *International Journal of Heat and Mass Transfer*, 44(23):4433–4443, 2001.
- [4] M. Mikami, M. Kono, J. Sato, and D. L. Dietrich. Interactive effects in two-droplet combustion of miscible binary fuels at high pressure. *Symposium (International) on Combustion*, 27(2):2643–2649, 1998.
- [5] A. Daïf, M. Bouaziz, X. Chesneau, and A. A. Cherif. Comparison of multicomponent fuel droplet vaporization experiments in forced convection with the sirignano model. *Experimental Thermal and Fluid Science*, 18(4):282–290, 1998.
- [6] B. Abramzon and W. A. Sirignano. Droplet vaporization model for spray combustion calculations. *International Journal of Heat and Mass Transfer*, 32(9):1605–1618, 1989.
- [7] P. Le Clercq and J. Bellan. Direct numerical simulation of a transitional temporal mixing layer laden with multicomponent-fuel evaporating drops using continuous thermodynamics. *Physics of Fluids*, 16(6):1884–1907, 2004.
- [8] C. K. Westbrook and F. L. Dryer. Chemical kinetic modeling of hydrocarbon combustion. *Progress in Energy and Combustion Science*, 10(1):1–57, 1984.
- [9] S. Honnet, K. Seshadri, U. Niemann, and N. Peters. A surrogate fuel for kerosene. *Proceedings of the Combustion Institute*, 32(1):485–492, 2009.

- [10] G. Blanquart, P. Pepiot-Desjardins, and H. Pitsch. Chemical mechanism for high temperature combustion of engine relevant fuels with emphasis on soot precursors. *Combustion and Flame*, 156(3):588–607, 2009.
- [11] K. Narayanaswamy, G. Blanquart, and H. Pitsch. A consistent chemical mechanism for oxidation of substituted aromatic species. *Combustion and Flame*, 157(10):1879–1898, 2010.
- [12] H. Watanabe, R. Kurose, M. Hayashi, T. Kitano, and S. Komori. Effects of ambient pressure and precursors on soot formation in spray flames. *Advanced Powder Technology*, 25(4):1376–1387, 2014.
- [13] M. Nakamura, F. Akamatsu, R. Kurose, and M. Katsuki. Combustion mechanism of liquid fuel spray in a gaseous flame. *Physics of Fluids*, 17(12):123301, 2005.
- [14] H. Watanabe, R. Kurose, S.-M. Hwang, and F. Akamatsu. Characteristics of flamelets in spray flames formed in a laminar counterflow. *Combustion and Flame*, 148(4):234–248, 2007.
- [15] H. Watanabe, R. Kurose, S. Komori, and H. Pitsch. Effects of radiation on spray flame characteristics and soot formation. *Combustion and Flame*, 152(1):2–13, 2008.
- [16] Y. Baba and R. Kurose. Analysis and flamelet modelling for spray combustion. *Journal of Fluid Mechanics*, 612:45–79, 2008.
- [17] C. T. Crowe, M. P. Sharma, and D. E. Stock. The particle-source-in cell (PSI-CELL) model for gas-droplet flows. *Journal of Fluids Engineering*, 99(2):325–332, 1977.
- [18] J. Bellan and K. Harstad. Analysis of the convective evaporation of nondilute clusters of drops. *International Journal of Heat and Mass Transfer*, 30(1):125–136, 1987.

- [19] R. S. Miller, K. Harstad, and J. Bellan. Evaluation of equilibrium and non-equilibrium evaporation models for many-droplet gas-liquid flow simulations. *International Journal of Multiphase Flow*, 24(6):1025–1055, 1998.
- [20] R. Kurose, H. Makino, S. Komori, M. Nakamura, F. Akamatsu, and M. Katsuki. Effects of outflow from the surface of a sphere on drag, shear lift, and scalar diffusion. *Physics of Fluids*, 15(8):2338–2351, 2003.
- [21] K. M. Watson. Thermodynamics of the liquid state. *Industrial & Engineering Chemistry*, 35(4):398–406, 1943.
- [22] D.-Y. Peng and D. B. Robinson. A new two-constant equation of state. *Industrial & Engineering Chemistry Fundamentals*, 15(1):59–64, 1976.
- [23] R. D. Gunn and T. Yamada. A corresponding states correlation of saturated liquid volumes. *AIChE Journal*, 17(6):1341–1345, 1971.
- [24] NIST Chemistry webbook, NIST Standard reference database. <http://webbook.nist.gov/chemistry>.
- [25] C. B. Willingham, W. J. Taylor, J. M. Pignocco, and F. D. Rossini. Vapor pressures and boiling points of some paraffin, alkylcyclopentane, alkylcyclohexane, and alkylbenzene hydrocarbons. *Journal of Research of the National Bureau of Standards*, 35(3):219–244, 1945.
- [26] K. Sato. *Estimation of physical property coefficients (In Japanese)*. Maruzen Publishing Co., Ltd, 1954.
- [27] K. Luo, H. Pitsch, M. G. Pai, and O. Desjardins. Direct numerical simulations and analysis of three-dimensional *n*-heptane spray flames in a model swirl combustor. *Proceedings of the Combustion Institute*, 33(2):2143–2152, 2011.
- [28] K. Matsuda, R. Onishi, R. Kurose, and S. Komori. Turbulence effect on cloud radiation. *Physical Review Letters*, 108(22):224502, 2012.

- [29] F. Akamatsu, Y. Miutani, M. Katsuki, S. Tsushima, and Y. D. Cho. Measurement of the local group combustion number of droplet clusters in a premixed spray stream. *Symposium (International) on Combustion*, 26(1):1723–1729, 1996.
- [30] Y. Morinishi, T. S. Lund, O. V. Vasilyev, and P. Moin. Fully conservative higher order finite difference schemes for incompressible flow. *Journal of Computational Physics*, 143(1):90–124, 1998.
- [31] F. Nicoud. Conservative high-order finite-difference schemes for low-mach number flows. *Journal of Computational Physics*, 158(1):71–97, 2000.
- [32] B. P. Leonard. A stable and accurate convective modelling procedure based on quadratic upstream interpolation. *Computer Methods in Applied Mechanics and Engineering*, 19(1):59–98, 1979.
- [33] V. Moureau, C. Bérat, and H. Pitsch. An efficient semi-implicit compressible solver for large-eddy simulations. *Journal of Computational Physics*, 226(2):1256–1270, 2007.
- [34] R. J. Kee, G. Dixon-Lewis, J. Warnatz, M. E. Coltrin, J. A. Miller, and H. K. Moffat. A fortran computer code package for evaluation of gas-phase multi-component transport properties. *Sandia Report*, SAND86:8246, 1986.
- [35] R. J. Kee, G. Dixon-Lewis, J. Warnatz, M. E. Coltrin, J. A. Miller, and H. K. Moffat. A fortran chemical kinetic package for the analysis of gas phase chemical kinetic. *Sandia Report*, SAND89:8009B, 1989.
- [36] E. W. Curtis and P. V. Farrell. A numerical study of high-pressure droplet vaporization. *Combustion and Flame*, 90(2):85–102, 1992.
- [37] W. E. Ranz and W. R. Marshall. Evaporation from drops Part 1. *Chemical Engineering Progress*, 48(3):141–146, 1952.
- [38] H. H. Chiu and T. M. Liu. Group combustion of liquid droplets. *Combustion Science and Technology*, 17(3-4):127–142, 1977.

- [39] H. H. Chiu, H. Y. Kim, and E. J. Croke. Internal group combustion of liquid droplets. *Symposium (International) on Combustion*, 19(1):971–980, 1982.
- [40] K. Hagihara, H. Yamashita, and K. Yamamoto. Numerical study on influence of size and number density of droplet on spray combustion mode. *Journal of the Combustion Society of Japan (In Japanese)*, 51(158):343–353, 2009.
- [41] C. Wang, A. M. Dean, H. Zhu, and R. J. Kee. The effects of multicomponent fuel droplet evaporation on the kinetics of strained opposed-flow diffusion flames. *Combustion and Flame*, 160(2):265–275, 2013.
- [42] H. Watanabe, Y. Matsushita, H. Aoki, and T. Miura. Numerical simulation of emulsified fuel spray combustion with puffing and micro-explosion. *Combustion and Flame*, 157(5):839–852, 2010.
- [43] G. Borghesi, E. Mastorakos, and R. S. Cant. Complex chemistry DNS of *n*-heptane spray autoignition at high pressure and intermediate temperature conditions. *Combustion and Flame*, 160(7):1254–1275, 2013.
- [44] P. N. Brown, G. D. Byrne, and A. C. Hindmarsh. VODE: A variable-coefficient ODE solver. *SIAM Journal on Scientific and Statistical Computing*, 10(5):1038–1051, 1989.

Nomenclature

<p>A : Pre-exponential factor</p> <p>B_M : Mass transfer number [-]</p> <p>c_p : Specific heat capacity [J/(K kg)]</p> <p>D : Diffusion coefficient [m²/s]</p> <p>d : Droplet diameter [m]</p> <p>E_a : Activation energy [J/mol]</p> <p>f_s : Correction of Stokes drag [-]</p> <p>f_t : Correction of heat transfer [-]</p> <p>G : Group combustion number [-]</p> <p>Gr : Grashof number [-]</p> <p>h : Enthalpy [J/kg]</p> <p>L_K : Knudsen layer thickness [m]</p> <p>L_V : Latent heat [J/kg]</p> <p>m : Mass [kg]</p> <p>n : Reaction exponent [-]</p> <p>Nu : Nusselt number [-]</p> <p>P : Pressure [Pa]</p> <p>Pr : Prandtl number [-]</p> <p>R : Gas constant [J/(K mol)]</p> <p>S : Source term</p> <p>Sc : Schmidt number [-]</p> <p>Sh : Sherwood number [-]</p> <p>T : Temperature [K]</p> <p>\mathbf{u} : Velocity [m/s]</p> <p>v : Molar volume [m³/mol]</p> <p>W : Mole weight [kg/mol]</p> <p>X : Mole fraction [-]</p> <p>\mathbf{x} : Position [m]</p> <p>Y : Mass fraction [-]</p>	<p>β : Evaporation parameter [-]</p> <p>ε : Partial evaporation rate [-]</p> <p>λ : Thermal conductivity [W/(m K)]</p> <p>μ : Viscosity [Pa s]</p> <p>ρ : Density [kg/m³]</p> <p>τ : Response time [s]</p> <p>$\boldsymbol{\tau}$: Stress tensor [N/m²]</p> <p>$\dot{\omega}$: Reaction rate [mol/s]</p>
	<p>Subscripts</p> <p>0 : Initial value</p> <p><i>avg</i> : Averaged value</p> <p><i>c</i> : Critical point</p> <p><i>comb</i> : Combustion</p> <p><i>d</i> : Droplet's value</p> <p><i>F</i> : Fuel</p> <p><i>k</i> : Species <i>k</i></p> <p><i>nb</i> : Normal boiling point</p> <p><i>ref</i> : Reference value</p> <p><i>s</i> : Droplet surface</p> <p><i>sat</i> : Saturated value</p> <p><i>V</i> : Vapor's value</p>

Chapter 3

LES of combustion instability in a back-step flow

3.1 Introduction

In this chapter, effects of combustion conditions on combustion instability in a back-step flow are investigated using LES for gas and spray combustion. For the LES of spray combustion, the droplet evaporation model proposed in the previous chapter is employed.

Combustion instability in gas combustion has been studied for many types of combustors [1–5]. A back-step flow combustor is one of the simplest combustors and has been used in many previous studies. Altay et al. [6] performed experiments of combustion instability in a back-step flow and investigated the effects of equivalence ratio, inlet temperature, and fuel composition on the combustion instability. They showed that the consumption rate of strained flames can be used for determination of transitions of dynamic mode. Hong et al. [7] also performed experiments of combustion instability in a back-step flow and reported that the dynamic mode transition was observed by changing the equivalent ratio. In addition, it was found that the phase difference between the oscillations of pressure and heat release rate becomes almost zero at the onset of a dynamic mode, they mentioned that the critical value of the phase can be predicted based

on a linear acoustic energy balance analysis. Manoharan and Hemchandra [8] performed a stability analysis of absolute/convective instability transition in a back-step flow, and found that the interaction between the flow vorticity and density gradients affects the hydrodynamic instability characteristics when the flow velocity and density gradients are collocated. However, since they treated the flow as an inviscid and incompressible flow, it is difficult to apply the same discussions to real combustors directly.

In contrast to gas combustion, the number of previous studies on the combustion instability in spray combustion is very limited [9, 10]. Most recently, Tachibana et al. [10] performed LES of combustion instability in spray combustion and showed the feasibility of LES. However, the effects of differences in the combustion conditions on combustion instability were not discussed.

In this chapter, LES of combustion instability in a back-step flow are performed for gas and spray combustion, and the mechanism underlying combustion instability and the effect of initial droplet diameter distributions on combustion instability are investigated. Methane and kerosene are used as the fuel for gas and spray combustion, respectively. For the calculations of the reactions, the two-step global reaction models [3, 11] are used, and the dynamic thickened flame model [12–14] is used to incorporate the effects of SGS turbulence on the reactions.

3.2 Gas combustion

3.2.1 Numerical Simulation

3.2.1.1 Governing equations

The governing equations are the conservation equations of mass, momentum, energy, and mass of chemical species as

$$\frac{\partial \bar{\rho}}{\partial t} + \nabla \cdot (\bar{\rho} \tilde{\mathbf{u}}) = 0, \quad (3.1)$$

$$\frac{\partial \bar{\rho} \tilde{\mathbf{u}}}{\partial t} + \nabla \cdot (\bar{\rho} \tilde{\mathbf{u}} \tilde{\mathbf{u}}) = -\nabla \bar{P} + \nabla \cdot \mathbf{t}, \quad (3.2)$$

$$\frac{\partial \bar{\rho} \tilde{h}}{\partial t} + \nabla \cdot (\bar{\rho} \tilde{h} \tilde{\mathbf{u}}) = \frac{\partial \bar{P}}{\partial t} + \tilde{\mathbf{u}} \cdot \nabla \bar{P} + \nabla \cdot \left[\bar{\rho} \{EF D_h + (1 - \Omega) D_t\} \nabla \tilde{h} \right] + \mathbf{t} \cdot \nabla \tilde{\mathbf{u}}, \quad (3.3)$$

$$\frac{\partial \bar{\rho} \tilde{Y}_k}{\partial t} + \nabla \cdot (\bar{\rho} \tilde{Y}_k \tilde{\mathbf{u}}) = \nabla \cdot \left[\bar{\rho} \{EF D_k + (1 - \Omega) D_t\} \nabla \tilde{Y}_k \right] + \frac{E}{F} S_{comb,k}, \quad (3.4)$$

and the equation of state for ideal gas. Here the overbar, $\bar{\cdot}$, donates the filtered mean value of the physical quantity in GS for LES, and the tilde, $\tilde{\cdot}$, donates the Favre-averaged value. ρ is the density, P the pressure, h the enthalpy, Y_k the mass fraction of species k , and \mathbf{u} the velocity. \mathbf{t} is the stress tensor including SGS stress. D_h is the thermal diffusivity given as $\rho D_h = \lambda/c_p$. Here λ and c_p are the heat conductivity and the specific heat capacity, respectively. D_k is the mass diffusion coefficient of species k which is given under the unity Lewis number assumption as $\rho D_k = \lambda/c_p$. D_t is the turbulent diffusion coefficient. These SGS terms are calculated using the dynamic Smagorinsky model [15, 16]. $S_{comb,k}$ is the source term due to the reaction described later. Ω is the flame sensor [12–14] defined as

$$\Omega = \tanh \left(\alpha \frac{q}{q_{max}} \right). \quad (3.5)$$

Here q is the local heat release rate, and q_{max} is the maximum heat release rate calculated with the one-dimensional laminar flame simulation. $\alpha = 10$ is the parameter controlling the thickness of the transition layer between reacting and non-reacting zones. E is the Efficiency function which represents the effects of SGS turbulence on the reaction, and F

the Flame thickening factor which thickens the flame to resolve it by the computational grids of LES [12–14, 17, 18]. The E and F are calculated as below.

$$F = (F_{max} - 1)\Omega + 1, \quad (3.6)$$

$$E = (E_{max} - 1)\Omega + 1, \quad (3.7)$$

$$E_{max} = \left\{ 1 + \min \left(\frac{\Delta}{\delta_l^0} - 1, \Gamma \frac{u'_\Delta}{s_l^0} \right) \right\}, \quad (3.8)$$

$$\Gamma = \left[\left\{ (f_u^{-a} + f_\Delta^{-a})^{-1/a} \right\}^{-b} + f_{Re}^{-b} \right]^{-1/b}, \quad (3.9)$$

$$f_u = 4 \left(\frac{27C_k}{110} \right)^{1/2} \left(\frac{18C_k}{55} \right) \left(\frac{u'_\Delta}{s_l^0} \right)^2, \quad (3.10)$$

$$f_\Delta = \left[\frac{27C_k\pi^{4/3}}{110} \left\{ \left(\frac{\Delta}{\delta_l^0} \right)^{4/3} - 1 \right\} \right]^{1/2}, \quad (3.11)$$

$$f_{Re} = \left\{ \frac{9}{55} \exp \left(-\frac{3}{2} C_k \pi^{4/3} Re_\Delta^{-1} \right) \right\}^{1/2} Re_\Delta^{1/2}, \quad (3.12)$$

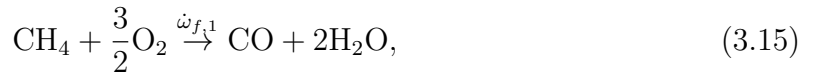
$$a = 0.60 + 0.20 \exp \left\{ -0.1 \left(\frac{u'_\Delta}{s_l^0} \right) \right\} - 0.20 \exp \left\{ -0.01 \left(\frac{\Delta}{\delta_l^0} \right) \right\}, \quad (3.13)$$

$$b = 1.4. \quad (3.14)$$

Here $F_{max} = 12$ is the maximum flame thickening coefficient. Δ is the filter size. δ_l^0 and s_l^0 are the laminar flame thickness and the laminar flame speed, respectively. u'_Δ and Re_Δ are the SGS turbulent velocity and SGS Reynolds number, respectively. C_k is the Kolmogorov constant [12–14, 17, 18].

3.2.1.2 Reaction model

Methane (CH_4) is used as the fuel, and for the calculation of the reaction, the following two-step global reaction model [3] is used.



Here the forward reaction rates, $\dot{\omega}_{f,1}$ and $\dot{\omega}_{f,2}$, are calculated as

$$\dot{\omega}_{f,1} = A_1 f_1(\phi) T^{\beta_1} \exp\left(-\frac{E_{a,1}}{RT}\right) [\text{CH}_4]^{n_{\text{CH}_4}} [\text{O}_2]^{n_{\text{O}_2,1}}, \quad (3.17)$$

$$\dot{\omega}_{f,2} = A_2 f_2(\phi) T^{\beta_2} \exp\left(-\frac{E_{a,2}}{RT}\right) [\text{CO}]^{n_{\text{CO}}} [\text{O}_2]^{n_{\text{O}_2,2}}. \quad (3.18)$$

Here [-] represents the mole concentration of chemical species. A is the pre-exponential factor, E_a the activation energy, β the temperature exponent, and n the reaction exponent. The values of these constants are shown in Table 3.1. $f(\phi)$ is the correction function depending on the local equivalence ratio, ϕ . $f_1(\phi)$ and $f_2(\phi)$ are given as

$$f_1(\phi) = \frac{2}{\left\{1 + \tanh\left(\frac{\phi_{0,1} - \phi}{\sigma_{0,1}}\right)\right\} + B_1 \left\{1 + \tanh\left(\frac{\phi - \phi_{1,1}}{\sigma_{1,1}}\right)\right\} + C_1 \left\{1 + \tanh\left(\frac{\phi - \phi_{2,1}}{\sigma_{2,1}}\right)\right\}}, \quad (3.19)$$

$$f_2(\phi) = \frac{1}{2} \left\{1 + \tanh\left(\frac{\phi_{0,2} - \phi}{\sigma_{0,2}}\right)\right\} + \frac{B_2}{2} \left\{1 + \tanh\left(\frac{\phi - \phi_{1,2}}{\sigma_{1,2}}\right)\right\} + \frac{C_2}{2} \left\{1 + \tanh\left(\frac{\phi - \phi_{2,2}}{\sigma_{2,2}}\right)\right\} \left\{1 + \tanh\left(\frac{\phi_{3,2} - \phi}{\sigma_{3,2}}\right)\right\}. \quad (3.20)$$

The values of the coefficients are shown in Table 3.2.

The reverse reaction rate, $\dot{\omega}_{r,2}$, is calculated using the equilibrium constant, K_c , as

$$\begin{aligned} \dot{\omega}_{2,r} &= A_2 f_2(\phi) T^{\beta_2} \exp\left(-\frac{E_{a,2}}{RT}\right) \frac{1}{K_c} [\text{CO}_2] \\ &= A_2 f_2(\phi) T^{\beta_2} \exp\left(-\frac{E_{a,2}}{RT}\right) C^{-\Delta\nu} \exp\left(\frac{\Delta G^\circ}{RT}\right) [\text{CO}_2], \end{aligned} \quad (3.21)$$

Here C is the total mole concentration and $\Delta\nu = 1/2$ the mole number change. ΔG° the change in the Gibbs free energy in the reaction calculated as

$$\Delta G^\circ = \Delta H - T \Delta S. \quad (3.22)$$

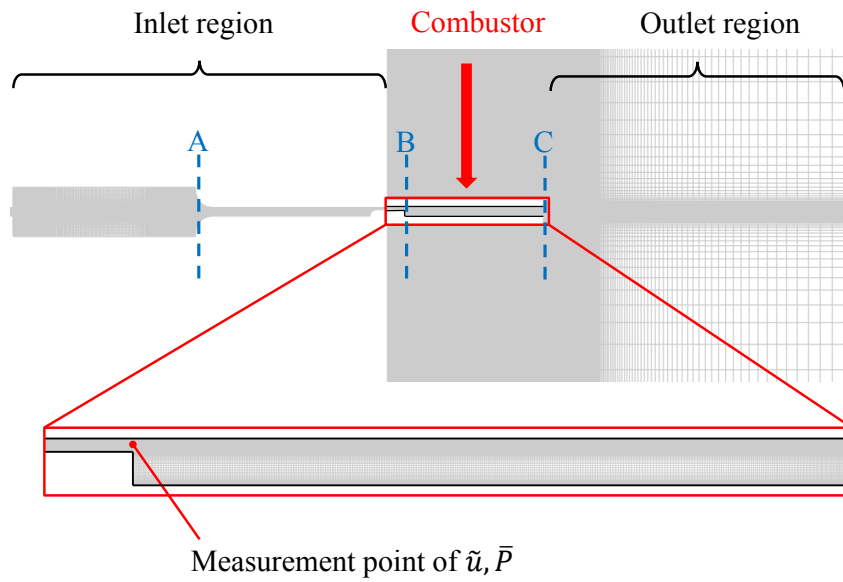
Here, ΔH and ΔS are the changes in the enthalpy and the entropy in the reaction, respectively.

Table 3.1: Pre-exponential factor, A_i , activation energy, $E_{a,i}$, temperature exponent, β_i , and reaction exponent, n , in Eqs. (3.17) and (3.18).

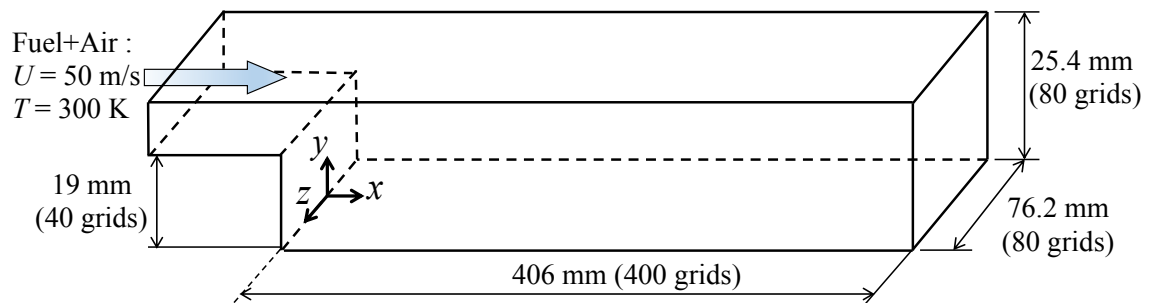
	$i = 1$	$i = 2$
A_i	4.9×10^9	2.0×10^8
$E_{a,i}$	3.55×10^4	1.20×10^4
β_i	0.0	0.8
n	$n_{\text{CH}_4} = 0.50$	$n_{\text{CO}} = 1.00$
	$n_{\text{O}_2,1} = 0.65$	$n_{\text{O}_2,2} = 0.50$

Table 3.2: Coefficients for correction functions of f_1 and f_2 in Eqs. (3.19) and (3.20).

	$\phi_{0,j}$	$\sigma_{0,j}$	B_j	$\phi_{1,j}$	$\sigma_{1,j}$	C_j	$\phi_{2,j}$	$\sigma_{2,j}$	$\phi_{3,j}$	$\sigma_{3,j}$
$j = 1$	1.1	0.09	0.37	1.13	0.03	6.7	1.6	0.22	-	-
$j = 2$	0.95	0.08	2.5×10^{-5}	1.3	0.04	0.0087	1.2	0.04	1.2	0.05



(a) Computational grid



(b) Computational conditions (Combustor)

Figure 3.1: Computational grid and conditions (Gas combustion).

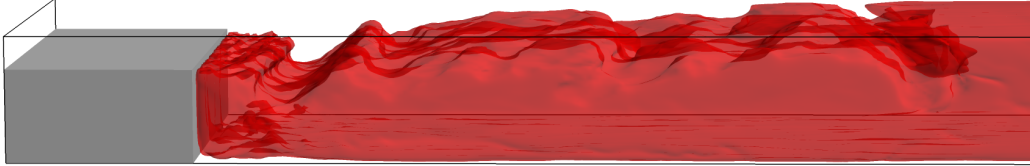


Figure 3.2: Instantaneous isosurface of gas temperature at 1400 K (Gas combustion).

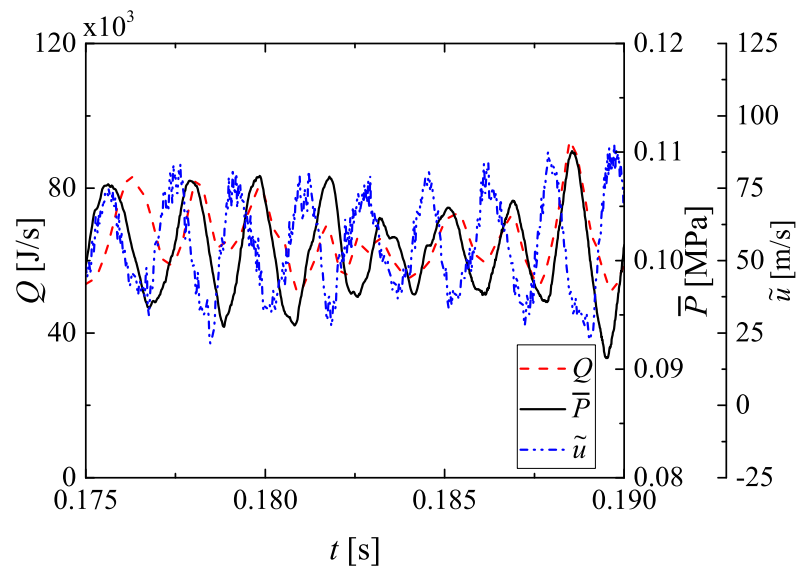


Figure 3.3: Time variations of pressure, \bar{P} , heat release rate, Q , and streamwise velocity, \tilde{u} (Gas combustion).

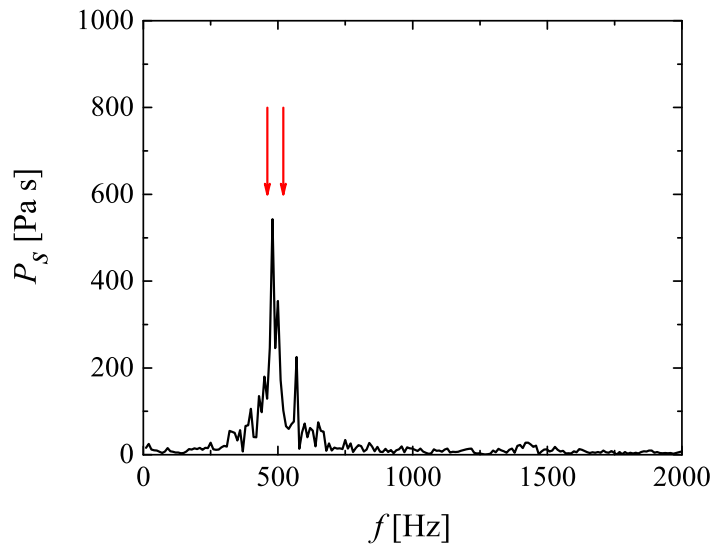


Figure 3.4: Spectrum of pressure oscillation (Gas combustion). Arrows indicate the peak frequencies obtained in a previous experiment by Smith and Zukoski [19].

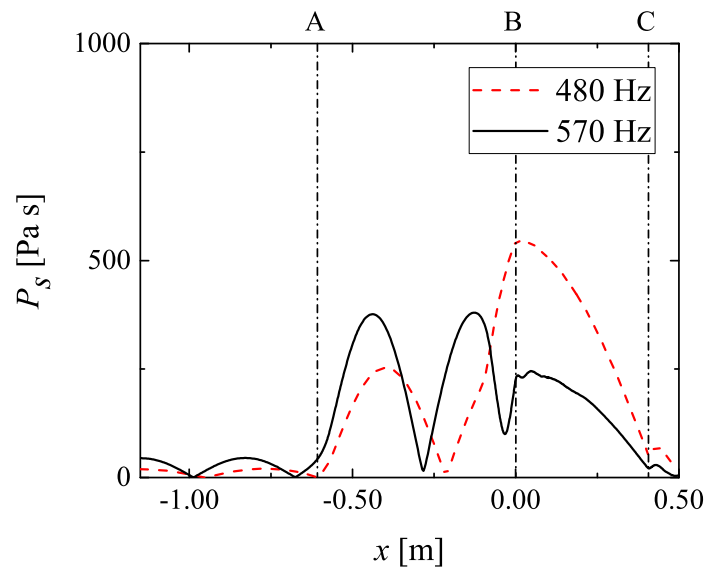


Figure 3.5: Streamwise profiles of amplitude of peak frequency components of pressure oscillation (Gas combustion). A, B, and C correspond to those indicated in Fig. 3.1(a), respectively.

3.2.1.3 Computational details

Fig. 3.1 shows the computational grid and conditions for gas combustion. Premixed gas of air and fuel (methane) is injected. The initial temperature of the gas mixture is 300 K and the equivalence ratio is 1.0. The domain and conditions for gas combustion are the same as those in the previous experimental study by Smith and Zukoski [19]. The temperature of the combustor wall touched by the flame is set to 1000 K.

The staggered grid is used for the computation, and the grid spacing is stretched to make the grid fine near the wall. The number of the total computational grids is 21.5 million. The pressure perturbation is captured by employing the pressure-based semi-implicit algorithm for compressible flows [20]. For the calculations of the convection terms of the energy and mass fractions of chemical species, the WENO scheme [21] is employed. The second-order accurate central difference scheme is used for the other terms. The third-order explicit Runge–Kutta method is used for the time advancement computation of the convection terms. The thermo physical properties and transport coefficients are obtained from CHEMKIN [22, 23].

The CPU time is about 1.3 million h (1270 h on the wall-clock time) on SGI ICE X (Intel Xeon E5-2670 processor, 1024 cores).

3.2.2 Results and Discussion

3.2.2.1 Feature of combustion instability

Figs. 3.2 and 3.3 show the instantaneous isosurface of gas temperature at 1400 K, and the time variations of pressure, \bar{P} , heat release rate, Q , and streamwise velocity, \tilde{u} , respectively. Here \bar{P} and \tilde{u} are the values at the point on the dump plane (i.e., the interface between the inlet duct and combustor), and Q is the total value calculated in the whole combustor. The injected premixed gas is found to react, and a flame is formed behind the dump plane (Fig. 3.2), and oscillations in \bar{P} , Q , and \tilde{u} are observed (Fig. 3.3). This signals that combustion instability is excited explicitly in the combustor.

Fig. 3.4 shows the spectrum of the pressure oscillation. The sampling time and

period are about 0.1 s and 0.02 ms, respectively. The same sampling time is used for other statistics of gas combustion to be discussed below. In this figure, the arrows mark the peak frequencies (460 and 520 Hz) obtained in the previous experiment [19]. The predicted spectrum has two peaks at around 500 Hz (480 and 570 Hz), and these frequencies agree well with those of the previous experiment [19]. This confirms that the LES is capable of capturing precisely the characteristics of combustion instability. Fig. 3.5 shows the streamwise profiles of the amplitude of the peak frequency components of the pressure oscillation. Here A, B, and C in the figure correspond to those indicated in Fig. 3.1(a), respectively. The two frequency components are found to have different oscillation modes, namely, the higher frequency mode is the first harmonic mode (1/4-wave mode) of the combustor which has an antinode and node at B and C, respectively, and the other is the second harmonic mode of the domain including the inlet duct which has nodes at A and C.

3.2.2.2 Mechanism of combustion instability

Fig. 3.6 shows the time variations of pressure, \bar{P} , heat release rate, Q , and streamwise velocity, \tilde{u} , which are rescaled from Fig. 3.3, and the instantaneous distributions of gas temperature and integrand of local Rayleigh Index, ri , on the x - y plane at the center ($z = 0$) at each time step of $t = t_1$ - t_7 . Here, the local Rayleigh Index, RI , and integrand of RI are defined as

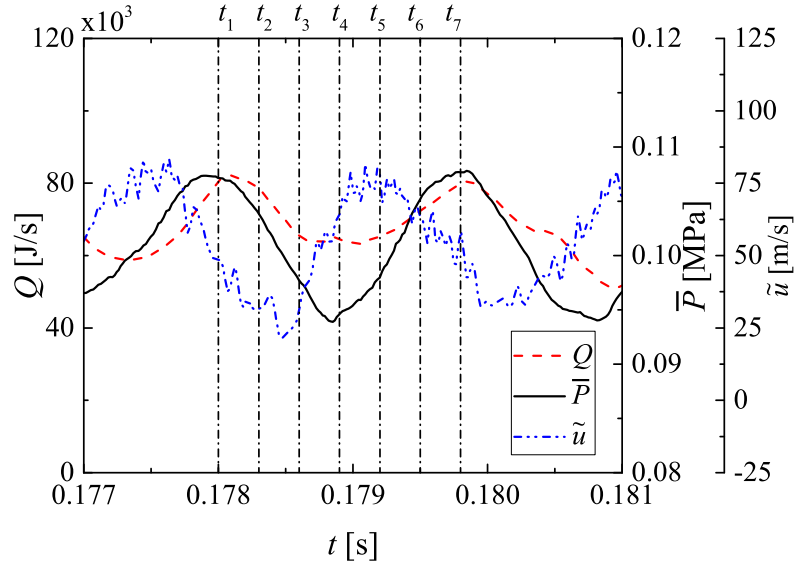
$$RI = \frac{1}{t_s} \int ri \, dt, \quad ri = \frac{(\bar{P} - P_{avg})q}{P_0 Q_{avg}}, \quad (3.23)$$

where t_s is the sampling time, P_{avg} the time-averaged local pressure, q the local heat release rate, P_0 the ambient pressure, Q_{avg} the time-averaged total heat release rate on the x - y plane at the center ($z = 0$). The positive and negative values of ri indicate that the heat release drives and damps the pressure oscillation, respectively. It is observed in Fig. 3.6(a) that there exist phase differences between the oscillations of \bar{P} , \tilde{u} , and Q . The phase of \tilde{u} leads that of \bar{P} by $\pi/2$. This phase difference is also seen in a previous experiment [24], and is caused by a similar mechanism typical of air-column vibrations,

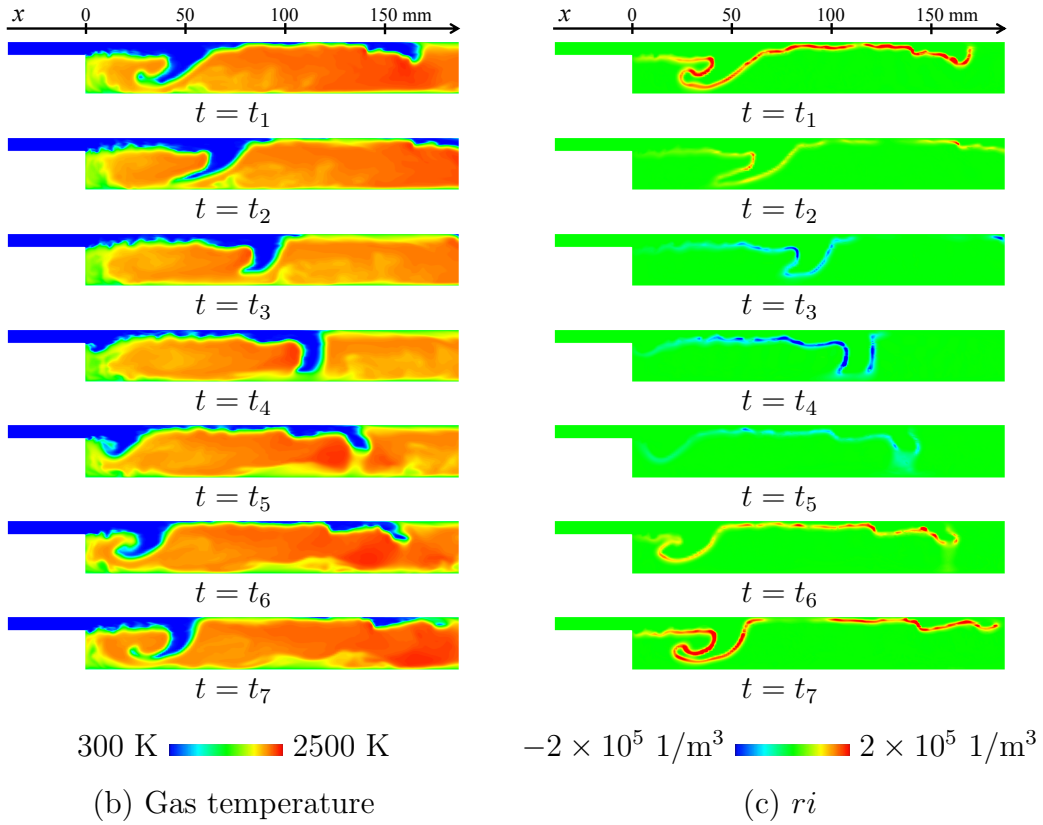
in which a pressure gradient controls a velocity acceleration. In contrast, the phase of Q lags that of \tilde{u} . This is because there exists a time lag between the increase in mass flow rate of mixture gas and the reaction. Consequently, the phase difference between \bar{P} and Q becomes small, and the combustion instability is excited.

It is found in Figs. 3.6(b) and (c) that the oscillation of \tilde{u} periodically generates a large vortex near the dump plane and conveys it downstream, and that when the large vortex exists near the dump plane, \bar{P} and Q become large ($t = t_1-t_2$ and t_6-t_7) (Fig. 3.6(a)), and ri becomes positive. Further, the values of ri in these periods ($t = t_1-t_2$ and t_6-t_7) are larger than the absolute values of the negative ri in the other periods ($t = t_3-t_5$). As results, RI becomes large near the dump plane of $x < 50$ mm, as shown in Figs. 3.7 and 3.8, which show the distribution of spanwise-averaged RI in the x - y plane and the streamwise distribution of cross-sectional (y - z)-averaged RI , RI_x , respectively. These results suggest that the large vortex near the dump plane drives combustion instability.

The reason why RI attains large values near the dump plane can be explained also using Fig. 3.9, which shows the streamwise distributions of phase- and cross-sectional (y - z)-averaged heat release rate, Q_x , at the phases of $\theta = 0$ ($\bar{P} = P_{max}$) and $\theta = \pi$ ($\bar{P} = P_{min}$). When pressure is at the maximum ($\theta = 0$), Q_x near the dump plane at around $x < 50$ mm becomes large, whereas when pressure is at the minimum ($\theta = \pi$), Q_x near the dump plane at around $x < 50$ mm becomes small.



(a) Time variations of \bar{P} , Q , and \tilde{u}



(b) Gas temperature

(c) ri

Figure 3.6: Time variations of pressure, \bar{P} , heat release rate, Q , and streamwise velocity, \tilde{u} , and instantaneous distributions of gas temperature and integrand of local Rayleigh Index, ri , on the x - y plane at the center ($z = 0$) at each time step (Gas combustion).

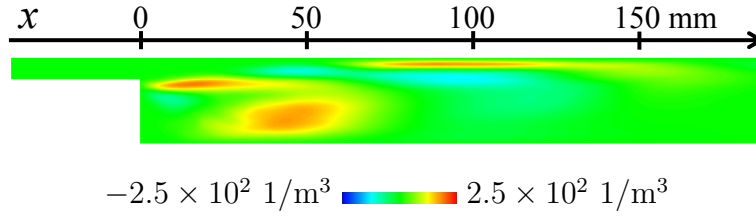


Figure 3.7: Distribution of spanwise-averaged local Rayleigh Index on the x - y plane (Gas combustion).

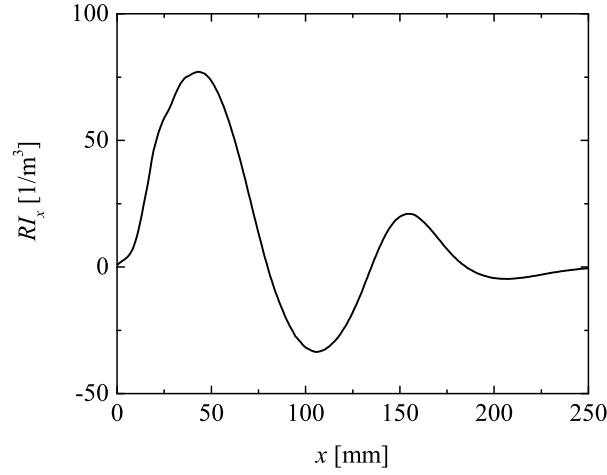


Figure 3.8: Streamwise distribution of cross-sectional (y - z)-averaged local Rayleigh Index, RI_x (Gas combustion).

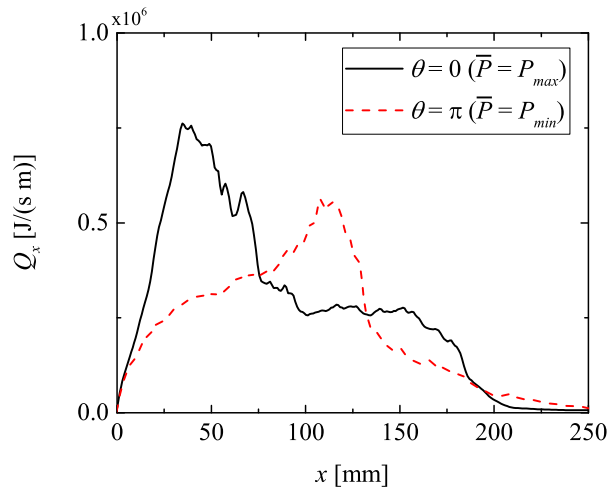


Figure 3.9: Streamwise distributions of phase- and cross-sectional (y - z)-averaged heat release rate, Q_x , at phases of $\theta = 0$ ($\bar{P} = P_{max}$) and $\theta = \pi$ ($\bar{P} = P_{min}$) (Gas combustion).

3.3 Spray combustion

3.3.1 Numerical Simulation

3.3.1.1 Governing equations

The governing equations for the gas phase are the conservation equations of mass, momentum, energy, and mass of chemical species as

$$\frac{\partial \bar{\rho}}{\partial t} + \nabla \cdot (\bar{\rho} \tilde{\mathbf{u}}) = S_\rho, \quad (3.24)$$

$$\frac{\partial \bar{\rho} \tilde{\mathbf{u}}}{\partial t} + \nabla \cdot (\bar{\rho} \tilde{\mathbf{u}} \tilde{\mathbf{u}}) = -\nabla \bar{P} + \nabla \cdot \mathbf{t} + S_{\rho u}, \quad (3.25)$$

$$\frac{\partial \bar{\rho} \tilde{h}}{\partial t} + \nabla \cdot (\bar{\rho} \tilde{h} \tilde{\mathbf{u}}) = \frac{\partial \bar{P}}{\partial t} + \tilde{\mathbf{u}} \cdot \nabla \bar{P} + \nabla \cdot \left[\bar{\rho} \{EFD_h + (1 - \Omega)D_t\} \nabla \tilde{h} \right] + \mathbf{t} \cdot \nabla \tilde{\mathbf{u}} + S_{\rho h}, \quad (3.26)$$

$$\frac{\partial \bar{\rho} \tilde{Y}_k}{\partial t} + \nabla \cdot (\bar{\rho} \tilde{Y}_k \tilde{\mathbf{u}}) = \nabla \cdot \left[\bar{\rho} \{EFD_k + (1 - \Omega)D_t\} \nabla \tilde{Y}_k \right] + \frac{E}{F} S_{comb,k} + S_{\rho Y_k}, \quad (3.27)$$

and the equation of state for ideal gas. Here the overbar, $\bar{\cdot}$, donates the filtered mean value of the physical quantity in GS for LES, and the tilde, $\tilde{\cdot}$, donates the Favre-averaged value. ρ is the density, P the pressure, h the enthalpy, Y_k the mass fraction of species k , and \mathbf{u} the velocity. \mathbf{t} is the stress tensor including SGS stress. D_h is the thermal diffusivity given as $\rho D_h = \lambda/c_p$. Here λ and c_p are the heat conductivity and the specific heat capacity, respectively. D_k is the mass diffusion coefficient of species k which is given under the unity Lewis number assumption as $\rho D_k = \lambda/c_p$. D_t is the turbulent diffusion coefficient. These SGS terms are calculated using the dynamic Smagorinsky model [15, 16]. $S_{comb,k}$ is the source term due to the reaction described later. E is the Efficiency function which represents the effects of SGS turbulence on the reaction, and F the Flame thickening factor which thickens the flame to resolve it by the computational grids of LES [12–14]. The Ω , E , and F are calculated using the method described in the previous section with $\alpha = 5$ and $F_{max} = 12$ in Eqs. (3.5) and (3.6).

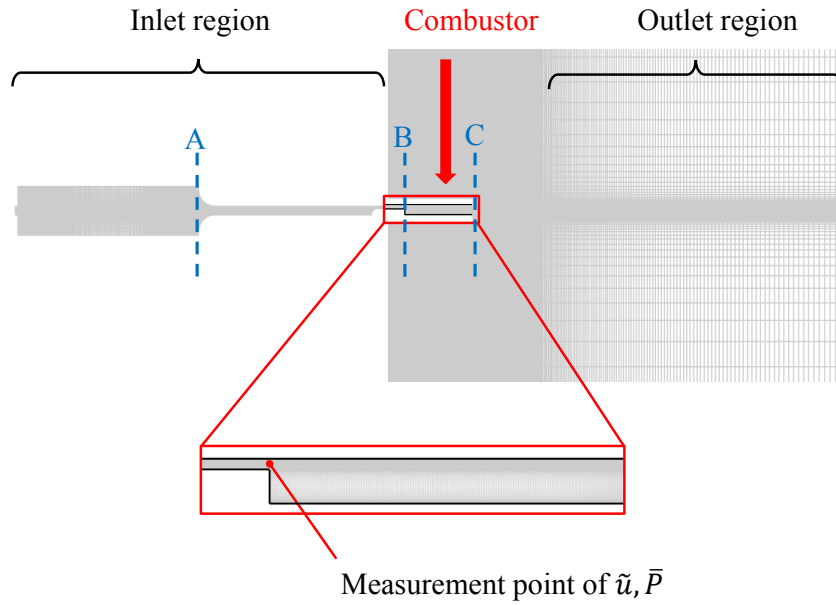
The source terms for the phase coupling between the gas and dispersed-droplets phases, S_ρ , $S_{\rho u}$, $S_{\rho h}$, and $S_{\rho Y_k}$, are calculated using the Particle-Source-In-Cell (PSI-Cell) method [25] as described in Chapter 2.

Table 3.3: Pre-exponential factor, A_i , activation energy, $E_{a,i}$, temperature exponent, β_i , and reaction exponent, n , in Eqs. (3.30) and (3.31).

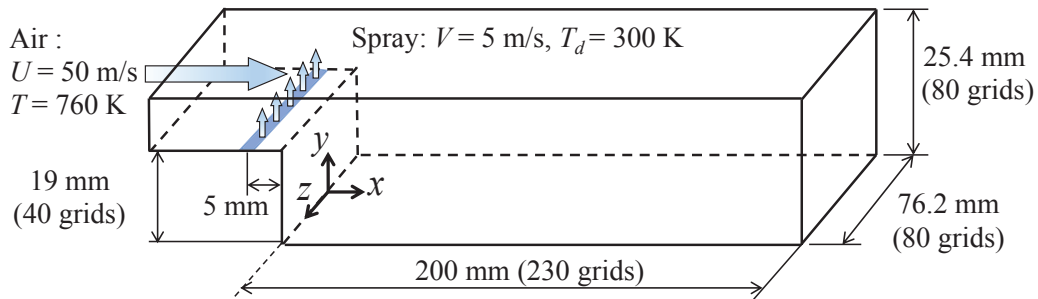
	$i = 1$	$i = 2$
A_i	4.15×10^4	2.0×10^4
$E_{a,i}$	8.0×10^{11}	4.5×10^{10}
β_i	0.0	0.0
n	$n_{\text{KERO}} = 0.55$	$n_{\text{CO}} = 1.00$
	$n_{\text{O}_2,1} = 0.90$	$n_{\text{O}_2,2} = 0.50$

Table 3.4: Coefficients for correction functions of f_1 and f_2 in Eqs. (3.32) and (3.33).

	$\phi_{0,j}$	$\sigma_{0,j}$	B_j	$\phi_{1,j}$	$\sigma_{1,j}$	C_j	$\phi_{2,j}$	$\sigma_{2,j}$	$\phi_{3,j}$	$\sigma_{3,j}$
$j = 1$	1.173	0.04	0.29	1.2	0.02	7.1	1.8	0.18	-	-
$j = 2$	1.146	0.045	1.5×10^{-4}	1.2	0.04	0.035	1.215	0.03	1.32	0.09



(a) Computational grid



(b) Computational conditions (Combustor)

Figure 3.10: Computational grid and conditions (Spray combustion).

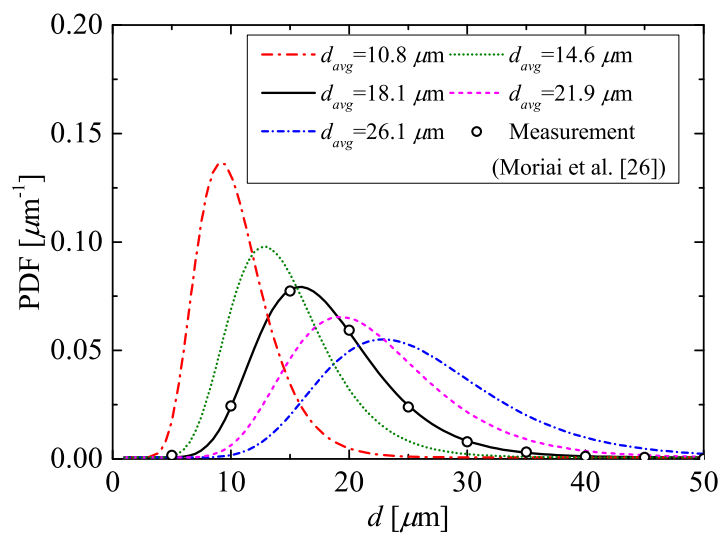
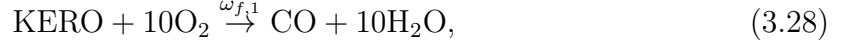


Figure 3.11: PDF distributions of initial droplet diameter (Spray combustion).

3.3.1.2 Reaction model

Kerosene (KERO) that is composed of $C_{10}H_{22}$ (76.7 wt%), C_9H_{12} (13.2 wt%), and C_9H_{18} (10.1 wt%) is used as the fuel, and for the calculation of the reaction, the following two-step global reaction model [11] is used.



Here the forward reaction rates, $\dot{\omega}_{f,1}$ and $\dot{\omega}_{f,2}$, are calculated as

$$\dot{\omega}_{f,1} = A_1 f_1(\phi) T^{\beta_1} \exp\left(-\frac{E_{a,1}}{RT}\right) [\text{KERO}]^{n_{\text{KERO}}} [\text{O}_2]^{n_{\text{O}_2,1}}, \quad (3.30)$$

$$\dot{\omega}_{f,2} = A_2 f_2(\phi) T^{\beta_2} \exp\left(-\frac{E_{a,2}}{RT}\right) [\text{CO}]^{n_{\text{CO}}} [\text{O}_2]^{n_{\text{O}_2,2}}. \quad (3.31)$$

Here [-] represents the mole concentration of chemical species. A is the pre-exponential factor, E_a the activation energy, β the temperature exponent, and n the reaction exponent. The values of these constants are shown in Table 3.3. $f(\phi)$ is the correction function depending on the local equivalence ratio, ϕ . $f_1(\phi)$ and $f_2(\phi)$ are given as

$$f_1(\phi) = \frac{2}{\left\{1 + \tanh\left(\frac{\phi_{0,1} - \phi}{\sigma_{0,1}}\right)\right\} + B_1 \left\{1 + \tanh\left(\frac{\phi - \phi_{1,1}}{\sigma_{1,1}}\right)\right\} + C_1 \left\{1 + \tanh\left(\frac{\phi - \phi_{2,1}}{\sigma_{2,1}}\right)\right\}}, \quad (3.32)$$

$$f_2(\phi) = \frac{1}{2} \left\{1 + \tanh\left(\frac{\phi_{0,2} - \phi}{\sigma_{0,2}}\right)\right\} + \frac{B_2}{2} \left\{1 + \tanh\left(\frac{\phi - \phi_{1,2}}{\sigma_{1,2}}\right)\right\} + \frac{C_2}{2} \left\{1 + \tanh\left(\frac{\phi - \phi_{2,2}}{\sigma_{2,2}}\right)\right\} \left\{1 + \tanh\left(\frac{\phi_{3,2} - \phi}{\sigma_{3,2}}\right)\right\}. \quad (3.33)$$

The values of the coefficients are shown in Table 3.4.

The reverse reaction rate, $\dot{\omega}_{r,2}$, is calculated using the equilibrium constant, K_c , as

$$\begin{aligned} \dot{\omega}_{2,r} &= A_2 f_2(\phi) T^{\beta_2} \exp\left(-\frac{E_{a,2}}{RT}\right) \frac{1}{K_c} [\text{CO}_2] \\ &= A_2 f_2(\phi) T^{\beta_2} \exp\left(-\frac{E_{a,2}}{RT}\right) C^{-\Delta\nu} \exp\left(\frac{\Delta G^\circ}{RT}\right) [\text{CO}_2], \end{aligned} \quad (3.34)$$

Here C is the total mole concentration and $\Delta\nu = 1/2$ the mole number change. ΔG° the change in the Gibbs free energy in the reaction calculated as

$$\Delta G^\circ = \Delta H - T \Delta S. \quad (3.35)$$

Here, ΔH and ΔS are the changes in the enthalpy and the entropy in the reaction, respectively.

3.3.1.3 Computational details

Fig. 3.10 shows the computational grid and conditions for spray combustion. The domain is the same as those in gas combustion, except for the combustor length, which is about half that for gas combustion. Air is injected from the inlet, and fuel droplets (kerosene) are injected with vertical velocity from 5 mm just before the step. The initial air temperature is 760 K and the equivalence ratio is 1.0. Fig. 3.11 shows the initial droplet diameter distributions. The averaged diameters, d_{avg} , are 10.8, 14.6, 18.1, 21.9, and 26.1 μm , and the probability density function (PDF) of the droplet diameter, $f(d)$, is given by a log-normal function,

$$f(d) = \frac{1}{\sqrt{2\pi}\sigma d} \exp \left\{ -\frac{\ln(d/d_0)^2}{2\sigma^2} \right\}. \quad (3.36)$$

Here d is the droplet diameter, and σ and d_0 the parameters of the function. The values of σ and d_0 for $d_{avg} = 18.1 \mu\text{m}$ are determined by fitting the curve to previous measurements obtained by Moriai et al. [26]. For the other droplet diameter conditions, the PDF are given using the same value of σ and changing the value of d_0 . The temperature of the combustor wall touched by the flame is set to 1000 K.

The staggered grid is used for the computation, and the grid spacing is stretched to make the grid fine near the wall. The number of the total computational grids is 21.5 million. The pressure perturbation is captured by employing the pressure-based semi-implicit algorithm for compressible flows [20]. For the calculations of the convection terms of the energy and mass fractions of chemical species, the WENO scheme [21] is employed. The second-order accurate central difference scheme is used for the other terms. The third-order explicit Runge–Kutta method is used for the time advancement computation of the convection terms. The thermo physical properties and transport coefficients are obtained from CHEMKIN [22, 23].

The CPU time is about 0.48 million h (470 h on the wall-clock time) on SGI ICE X (Intel Xeon E5-2670 processor, 1024 cores).

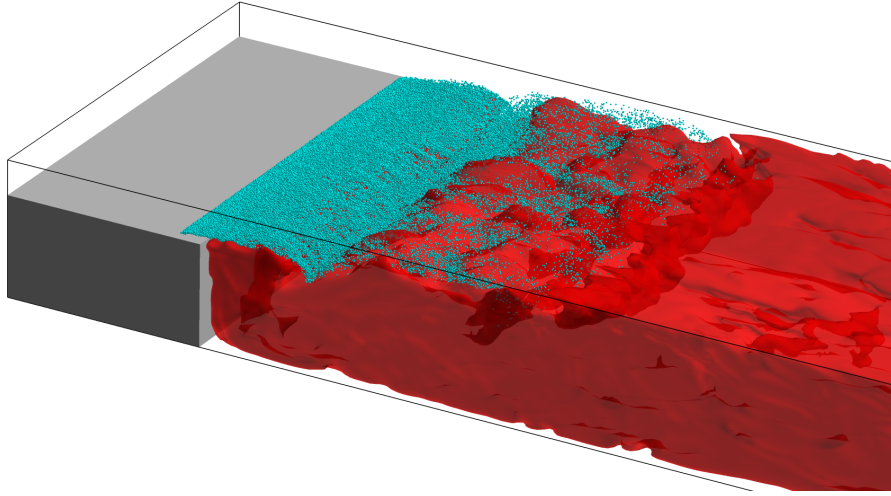


Figure 3.12: Instantaneous isosurface of gas temperature at 1600 K and fuel droplets (Spray combustion, $d_{avg} = 18.1 \mu\text{m}$).

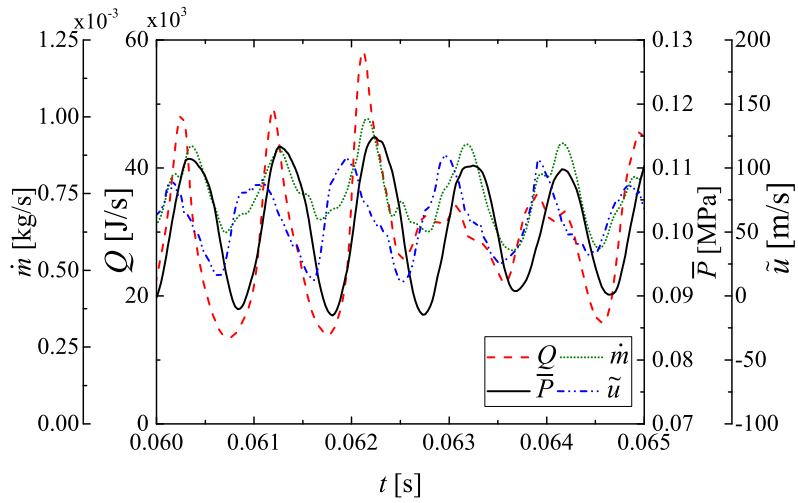


Figure 3.13: Time variations of pressure, \bar{P} , heat release rate, Q , streamwise velocity, \tilde{u} , and droplet evaporation rate, \dot{m} (Spray combustion, $d_{avg} = 18.1 \mu\text{m}$).

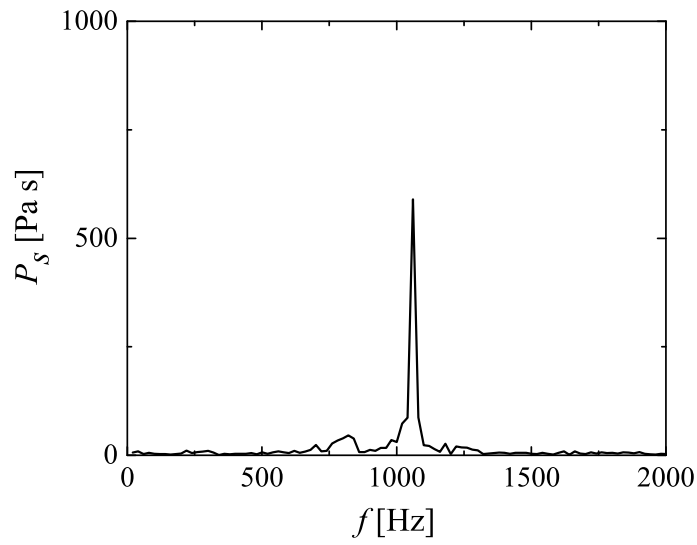


Figure 3.14: Spectrum of pressure oscillation (Spray combustion, $d_{avg} = 18.1 \mu\text{m}$).

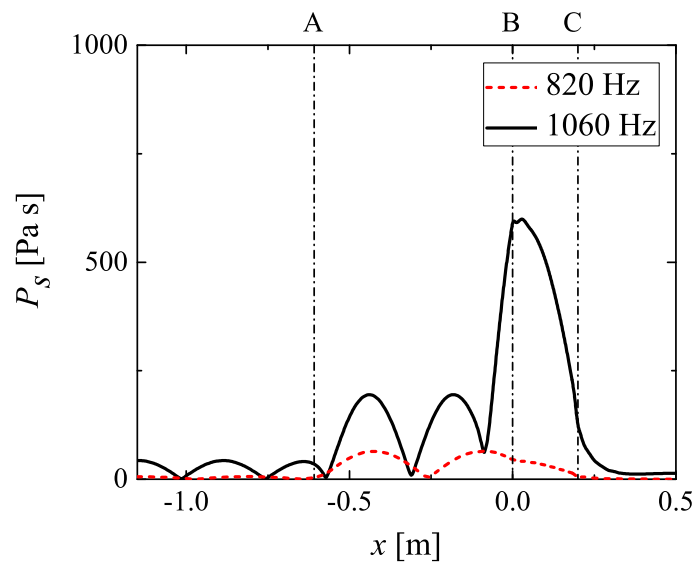
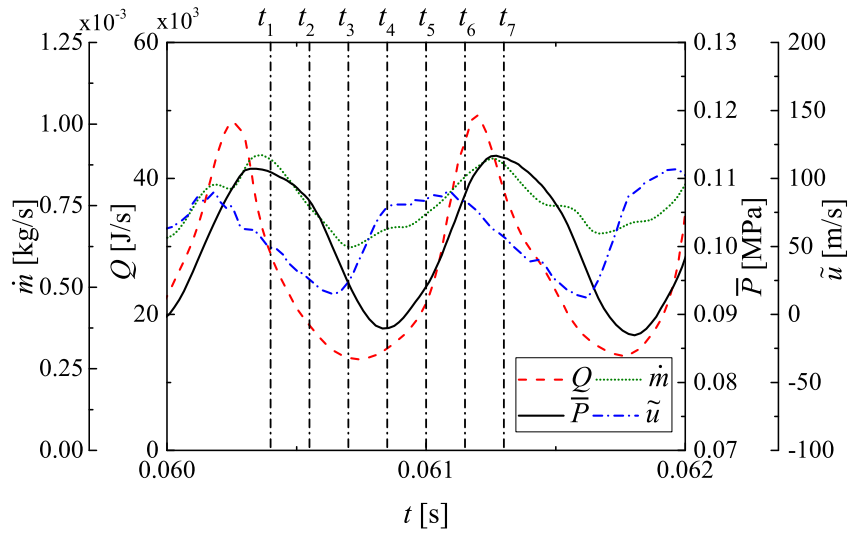
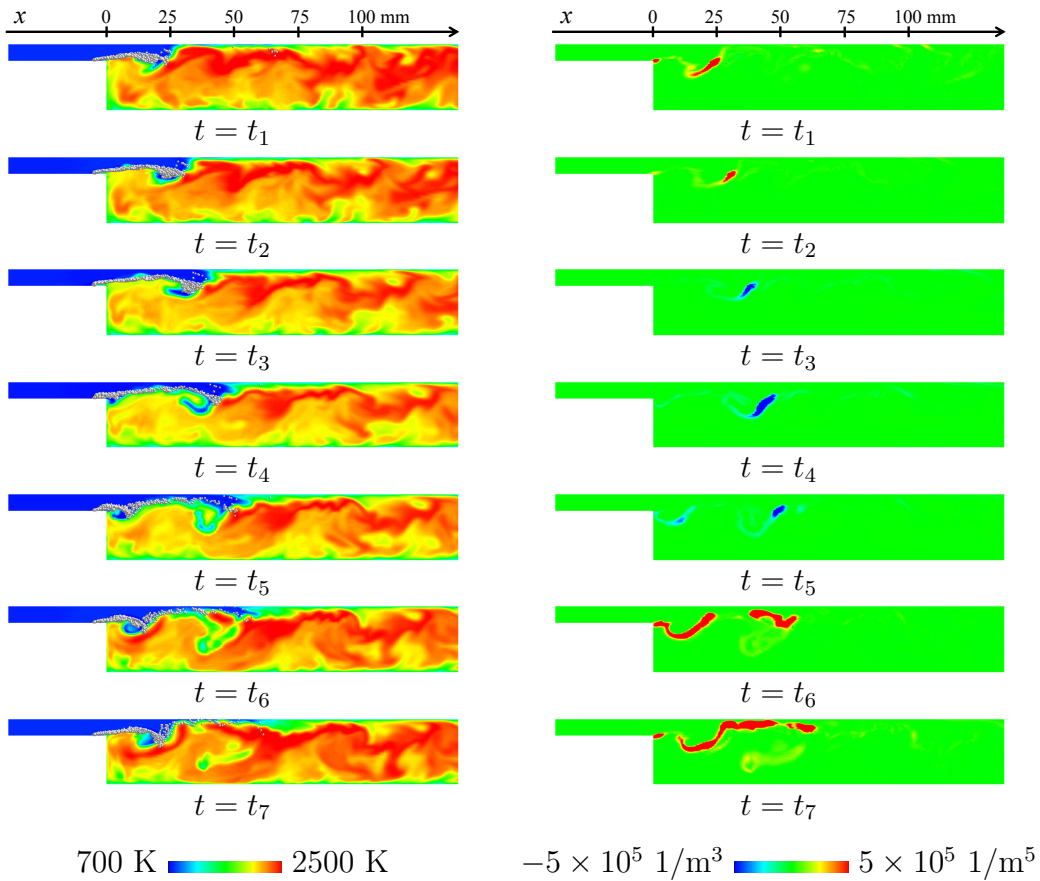


Figure 3.15: Streamwise profiles of amplitude of peak frequency components of pressure oscillation (Spray combustion, $d_{avg} = 18.1 \mu\text{m}$). A, B, and C correspond to those in Fig. 3.10(a), respectively.



(a) Time variations of \bar{P} , Q , \tilde{u} , and \dot{m}



(b) Gas temperature and fuel droplets

(c) ri

Figure 3.16: Time variations of pressure, \bar{P} , heat release rate, Q , and streamwise velocity, \tilde{u} , and droplet evaporation rate, \dot{m} , and instantaneous distributions of gas temperature and fuel droplets, and integrand of local Rayleigh Index, ri , on the x - y plane at the center ($z = 0$) at each time step (Spray combustion, $d_{avg} = 18.1 \mu\text{m}$).

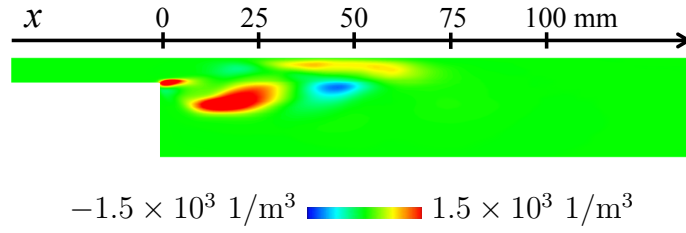


Figure 3.17: Distribution of spanwise-averaged local Rayleigh Index on the x - y plane (Spray combustion, $d_{avg} = 18.1 \mu\text{m}$).

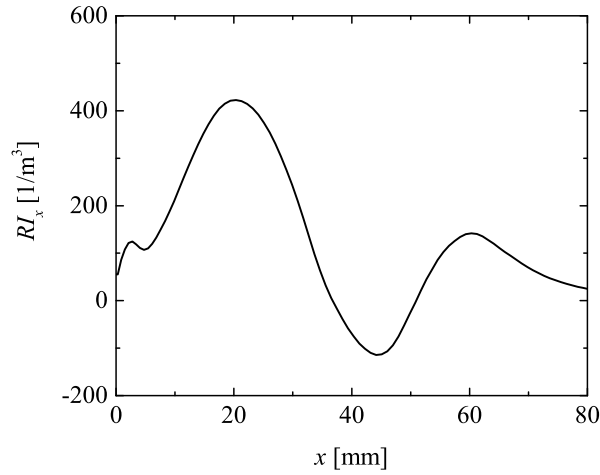


Figure 3.18: Streamwise distribution of cross-sectional (y - z)-averaged local Rayleigh Index, RI_x (Spray combustion, $d_{avg} = 18.1 \mu\text{m}$).

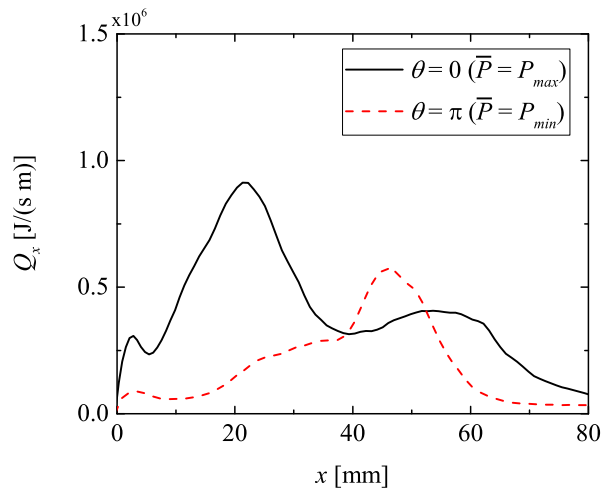


Figure 3.19: Streamwise distributions of phase- and cross-sectional (y - z)-averaged heat release rate, Q_x , at phases of $\theta = 0$ ($\bar{P} = P_{max}$) and $\theta = \pi$ ($\bar{P} = P_{min}$) (Spray combustion, $d_{avg} = 18.1 \mu\text{m}$).

3.3.2 Results and discussion

3.3.2.1 Feature of combustion instability

Figs. 3.12 and 3.13 show the instantaneous isosurface for gas temperature of 1600 K and fuel droplets in the case of $d_{avg} = 18.1 \mu\text{m}$, and the time variations of pressure, \bar{P} , heat release rate, Q , streamwise velocity, \tilde{u} , and droplet evaporation rate, \dot{m} , in the case of $d_{avg} = 18.1 \mu\text{m}$, respectively. Here \bar{P} and \tilde{u} are the values at the point on the dump plane of the combustor (Fig. 3.10), and Q and \dot{m} are the total values calculated in the whole combustor. The injected fuel droplets are found to flow downstream while dispersing as clusters and evaporating, the evaporated gas subsequently reacts with air, and a flame is formed behind the dump plane (Fig. 3.12). An oscillation in \dot{m} is also observed in addition to oscillations in \bar{P} , Q , and \tilde{u} , which are also observed in the gas combustion (Figs. 3.3 and 3.13). This implies that combustion instability is excited in the combustor, similar to the gas combustion, described above.

Figs. 3.14 and 3.15 show the spectrum of the pressure oscillation and the streamwise profiles of the amplitude of the peak frequency components of the pressure oscillation in the case of $d_{avg} = 18.1 \mu\text{m}$, respectively. Here, A, B, and C in Fig. 3.15 correspond to those indicated in Fig. 3.10(a), respectively. The sampling time and period are about 0.05 s and 0.02 ms, respectively. The same sampling time is used for other statistics of spray combustion discussed below. The spectrum has two peaks at around 1000 Hz (820 and 1060 Hz), and the peak of 1060 Hz is much larger than that of 820 Hz (Fig. 3.14). Further, the oscillation modes are the same as those in the gas combustion, namely, the higher frequency mode is the first harmonic mode (1/4-wave mode) of the combustor which has an antinode and node at B and C, respectively, and the other is the second harmonic mode of the domain including the inlet duct which has nodes at A and C.

3.3.2.2 Mechanism of combustion instability

Fig. 3.16 shows the time variations of pressure, \bar{P} , heat release rate, Q , and streamwise velocity, \tilde{u} , and droplet evaporation rate, \dot{m} , which are rescaled from Fig. 3.13, and the

instantaneous distributions of gas temperature and fuel droplets, and integrand of local Rayleigh Index, ri , at each time step of $t = t_1 - t_7$ in the case of $d_{avg} = 18.1 \mu\text{m}$. From Fig. 3.16(a), the relationship between the phases of the oscillations of \bar{P} , Q , and \tilde{u} is found to be the same as that in the gas combustion (Fig. 3.6(a)), namely, the phase of \tilde{u} leads that of \bar{P} , and the phase of Q lags that of \bar{P} . Further, the phase of \dot{m} is observed to lag that of Q . This is because a time lag exists between the increase in gas temperature surrounding the fuel droplets as a consequence of heat release and the increase in droplet evaporation rate. The behavior is different from that in the previous study [10], in which the phase of \dot{m} led that of Q . This is considered to be due to the fact that the equivalence ratio, ϕ , in the previous study ($\phi \sim 0.57$) [10] was much lower than that in the present study ($\phi = 1.0$). Whereas the reaction rate for a low equivalence ratio is dominated by droplet evaporation, for a high equivalence ratio, the rate is dominated by turbulent mixing of the evaporated fuel and oxygen. In addition, the differences in the conditions of the combustor (e.g., with or without a swirling flow and pilot burners) may cause the difference from the previous study [10]. It is found in Figs. 3.16(b) and (c) that the gas temperature and ri oscillate periodically similar to those in the gas combustion, and that the fuel droplets involved in a large vortex which is periodically generated. This periodical motion of the fuel droplets causes the oscillation of \dot{m} in Fig. 3.16(a).

Figs. 3.17, 3.18, and 3.19 show the distribution of spanwise-averaged RI in the x - y plane, the streamwise distribution of cross-sectional (y - z)-averaged RI , RI_x , and the streamwise distributions of phase- and cross-sectional (y - z)-averaged heat release rate, Q_x , at the phases of $\theta = 0$ ($\bar{P} = P_{max}$) and $\theta = \pi$ ($\bar{P} = P_{min}$) in the case of $d_{avg} = 18.1 \mu\text{m}$, respectively. RI becomes large near the dump plane at around $x < 25$ mm, where Q_x at the phases of $\theta = 0$ and $\theta = \pi$ become large and small, respectively. These results are the same as those in the gas combustion (Figs. 3.7, 3.8, and 3.9). Furthermore, the decrease in Q_x at the phase of $\theta = \pi$ is more remarkable than that in the gas combustion (Fig. 3.9). The reason is considered that, at the phase of $\theta = \pi$, the mass concentration of the fuel becomes too high to react due to the small mass flow rate of

air (Fig. 3.16(a), note that the phase of Q lags that of \tilde{u}). These results suggest that combustion instability in spray combustion is also driven by the generation of the large vortex near the dump plane as similar to that in the gas combustion, and is enhanced by the large difference in Q_x due to droplet evaporation.

3.3.2.3 Effect of initial droplet diameter

Figs. 3.20 and 3.21 show the spectra of the pressure oscillations and the streamwise profiles of the amplitude of the peak frequency components of the pressure oscillations in the cases of $d_{avg} = 10.8, 14.6, 21.9,$ and $26.1 \mu\text{m}$, respectively. Here, A, B, and C in Fig. 3.21 correspond to those indicated in Fig. 3.10(a), respectively. The spectra for all cases have peaks at around 1000 Hz, although the number of peaks differs for each (i.e., one–three peaks). The pressure oscillations in the all cases have oscillation modes of the first harmonic mode (1/4-wave mode) of the combustor which has an antinode and node at B and C, respectively, and the second harmonic mode of the domain including the inlet duct which has nodes at A and C, which are the same as those for the gas combustion. Fig. 3.22 shows the effect of the initial droplet diameter, d_{avg} , on the intensity of the pressure oscillations, P'_{rms} . It is found that P'_{rms} becomes the maximum in the case of $d_{avg} = 18.1 \mu\text{m}$. This result is consistent with the results of the RI analysis. Figs. 3.23 and 3.24 show the distribution of spanwise-averaged RI in the x – y plane and the streamwise distribution of cross-sectional (y – z)-averaged RI , RI_x , in the cases of $d_{avg} = 10.8, 14.6, 21.9,$ and $26.1 \mu\text{m}$, respectively. RI near the dump plane at around $x < 25$ mm is the largest in the case of $d_{avg} = 18.1 \mu\text{m}$.

To understand the reason for the difference in RI near the dump plane, Fig. 3.25 shows the streamwise distributions of phase- and cross-sectional (y – z)-averaged heat release rate, Q_x , at the phases of $\theta = 0$ ($\bar{P} = P_{max}$) and $\theta = \pi$ ($\bar{P} = P_{min}$) in the cases of $d_{avg} = 10.8, 14.6, 21.9,$ and $26.1 \mu\text{m}$. The differences in Q_x near the dump plane at around $x < 25$ mm between the phases of $\theta = 0$ and $\theta = \pi$ are found to be small in the cases of small and large initial droplet diameter than that in the case of $d_{avg} = 18.1 \mu\text{m}$. This can be explained as follows. In the large initial droplet diameter cases, near

the dump plane, the small evaporation rate due to the small total droplet surface area keeps mass concentration of fuel moderate even when the mass flow rate of air is small at the phase of $\theta = \pi$, and therefore, the heat release rate remains large at the phase of $\theta = \pi$. On the other hand, in the small initial droplet diameter cases, near the dump plane, the large evaporation rate due to the large total droplet surface area makes mass concentration of fuel too high to react even when the mass flow rate of air is large at the phase of $\theta = 0$, and therefore, the heat release rate remains small at the phase of $\theta = 0$. For these reasons, the difference in the heat release rate between the moments corresponding to maxima ($\theta = 0$) and minima ($\theta = \pi$) of the pressure oscillation becomes the largest in the case of $d_{avg} = 18.1 \mu\text{m}$, and the intensity of the combustion instability becomes the largest.

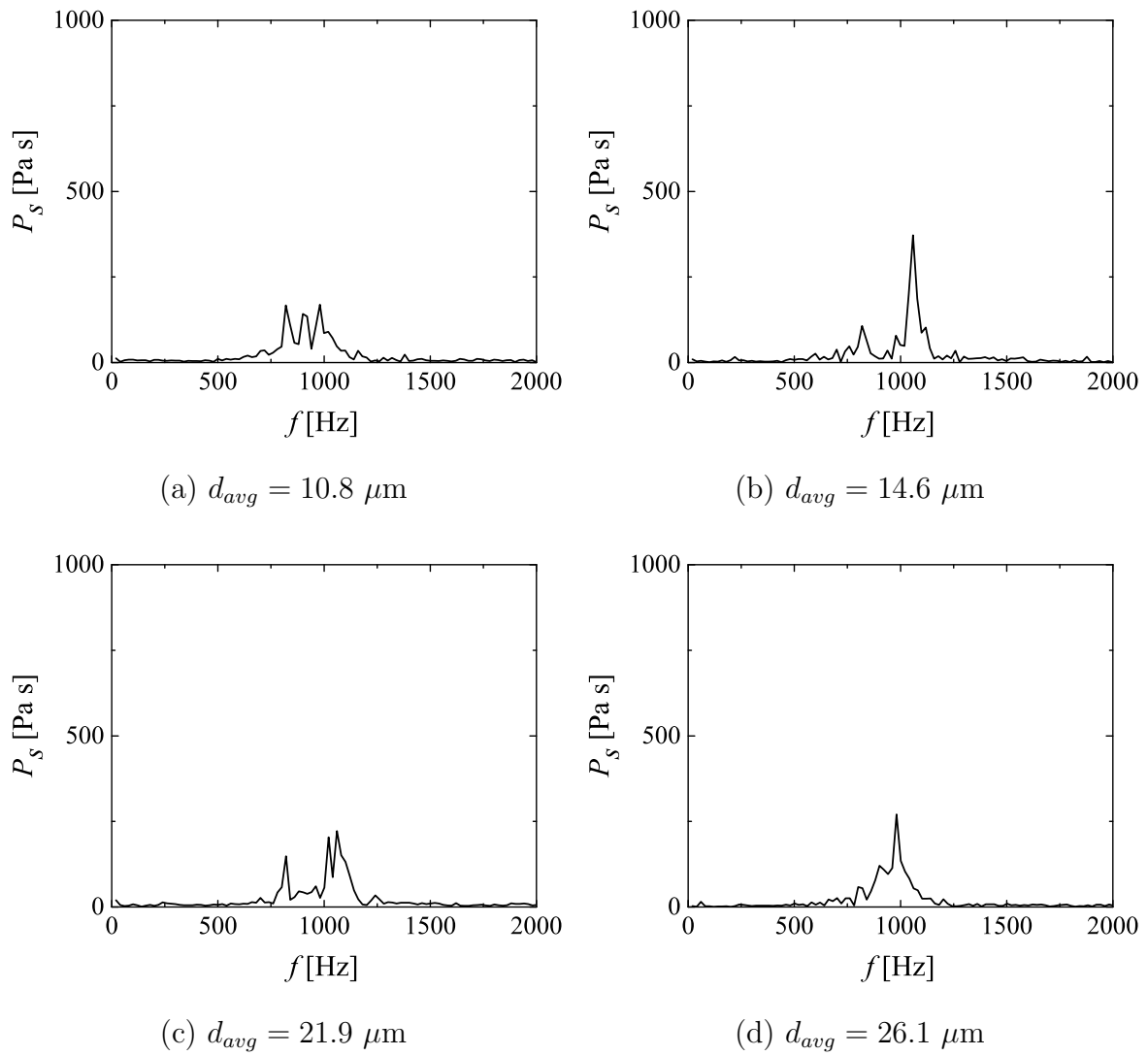


Figure 3.20: Spectra of pressure oscillations (Spray combustion, $d_{avg} = 10.8, 14.6, 21.9,$ and $26.1 \mu\text{m}$).

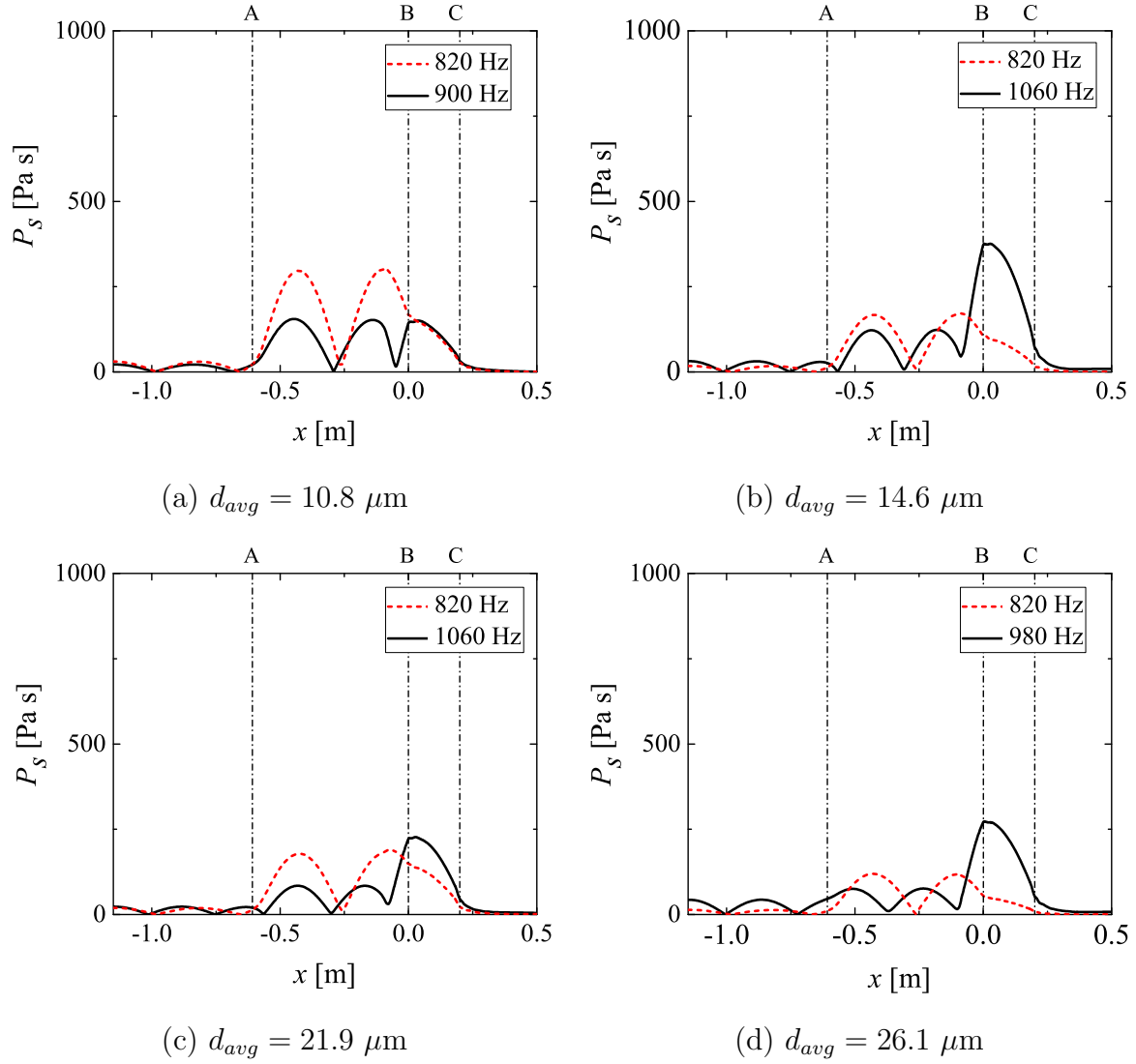


Figure 3.21: Streamwise profiles of amplitude of peak frequency components of pressure oscillation (Spray combustion, $d_{avg} = 10.8, 14.6, 21.9,$ and $26.1 \mu\text{m}$). A, B, and C correspond to those indicated in Fig. 3.10(a), respectively.

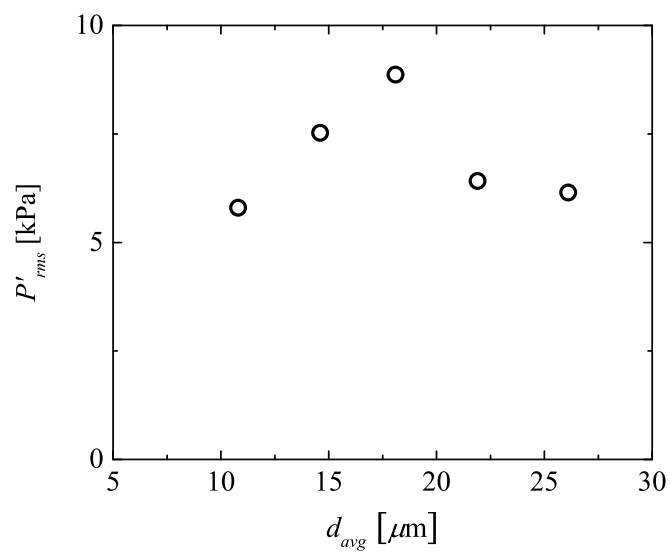


Figure 3.22: Effect of initial fuel droplet diameter, d_{avg} , on intensity of pressure oscillations, P'_{rms} .

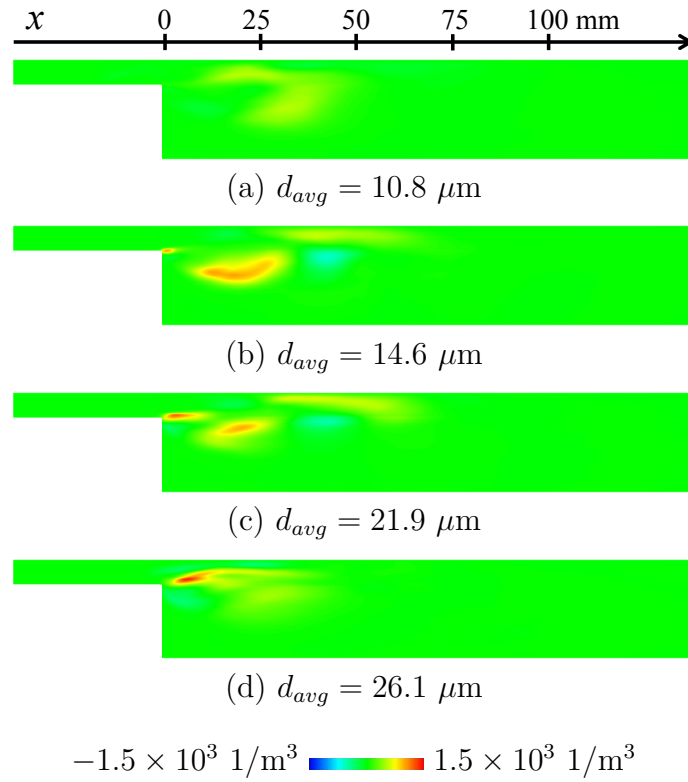


Figure 3.23: Distribution of spanwise-averaged local Rayleigh Index on the x - y plane (Spray combustion, $d_{avg} = 10.8, 14.6, 21.9,$ and $26.1 \mu\text{m}$).

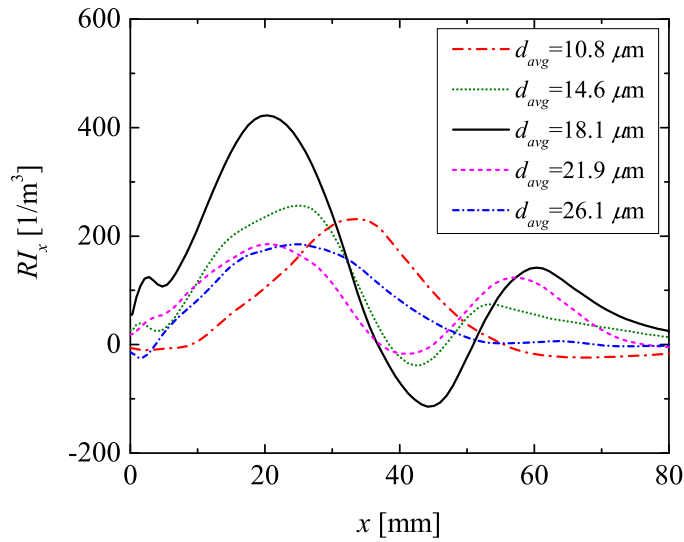
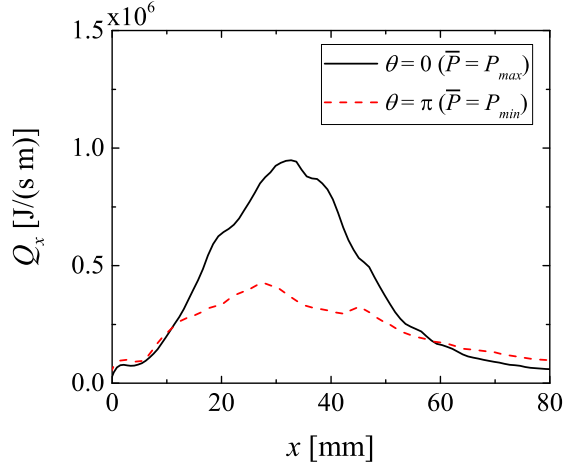
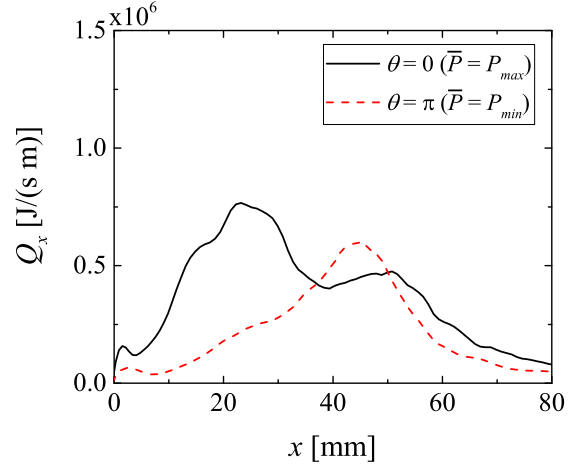


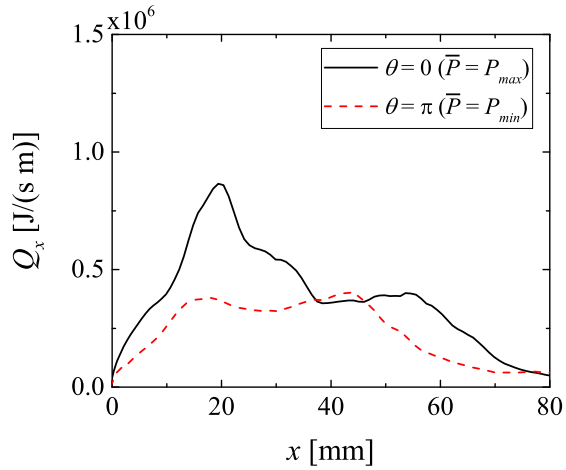
Figure 3.24: Streamwise distribution of cross-sectional (y - z)-averaged local Rayleigh Index, RI_x (Spray combustion, $d_{avg} = 10.8, 14.6, 21.9,$ and $26.1 \mu\text{m}$).



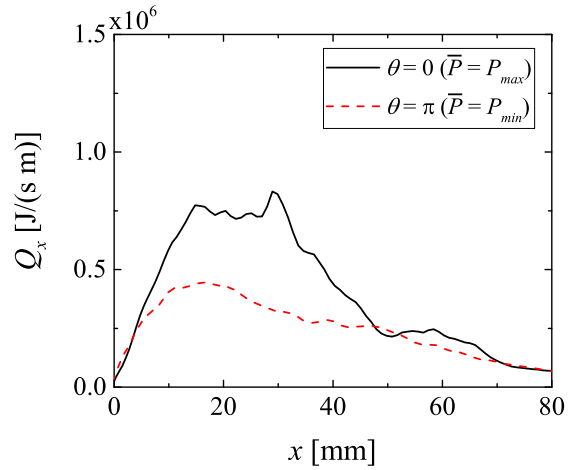
(a) $d_{avg} = 10.8 \mu\text{m}$



(b) $d_avg = 14.6 \mu\text{m}$



(c) $d_{avg} = 21.9 \mu\text{m}$



(d) $d_{avg} = 26.1 \mu\text{m}$

Figure 3.25: Streamwise distributions of phase- and cross-sectional (y - z)-averaged heat release rate, Q_x , at phases of $\theta = 0$ ($\bar{P} = P_{max}$) and $\theta = \pi$ ($\bar{P} = P_{min}$) (Spray combustion, $d_{avg} = 10.8, 14.6, 21.9,$ and $26.1 \mu\text{m}$).

3.4 Conclusions

In this chapter, LES of combustion instability in a back-step flow were performed for gas and spray combustion, and the mechanism underlying combustion instability and the effect of initial droplet diameter distributions on combustion instability were investigated. The main results obtained in this study can be summarized as follows.

1. In gas combustion, oscillations of pressure, heat release rate, and streamwise velocity with the same frequency but different phase are observed, and the spectrum of the pressure oscillation has two peaks whose frequencies agree well with those from a previous experimental study. This confirms that the present LES is capable of capturing precisely the characteristics of combustion instability. The inlet velocity oscillation periodically generates a large vortex near the dump plane and conveys it downstream, and when the large vortex exists near the dump plane, the integrand of the local Rayleigh Index becomes positive. This suggests that combustion instability is driven by the large vortex near the dump plane.
2. In spray combustion, an oscillation in droplet evaporation rate is also observed in addition to the oscillations in pressure, heat release rate, streamwise velocity, and the integrand of the local Rayleigh Index. The difference in the initial droplet diameter hardly affects the pressure oscillation mode, but strongly affects the intensity of the pressure oscillation, and the intensity of the pressure oscillation becomes the maximum for a specific initial droplet diameter. This is because, for this specific initial droplet diameter, the difference in the heat release rate near the dump plane at moments corresponding to maxima and minima in the pressure oscillation becomes the largest. The reason for this change of the behavior in the heat release rate against the pressure oscillation is that the difference in the initial droplet diameter causes the difference in the droplet evaporation rate.

References

- [1] R. Balachandran, B. O. Ayoola, C. F. Kaminski, A. P. Dowling, and E. Mastorakos. Experimental investigation of the nonlinear response of turbulent premixed flames to imposed inlet velocity oscillations. *Combustion and Flame*, 143(1):37–55, 2005.
- [2] K. Sato, E. Knudsen, and H. Pitsch. Study of combustion instabilities imposed by inlet velocity disturbance in combustor using LES. *ASME Turbo Expo 2009: Power for Land, Sea, and Air*, 87–99, 2009.
- [3] B. Franzelli, E. Riber, L. Y. M. Gicquel, and T. Poinsot. Large eddy simulation of combustion instabilities in a lean partially premixed swirled flame. *Combustion and Flame*, 159(2):621–637, 2012.
- [4] P. Wolf, G. Staffelbach, L. Y. M. Gicquel, J.-D. Müller, and T. Poinsot. Acoustic and large eddy simulation studies of azimuthal modes in annular combustion chambers. *Combustion and Flame*, 159(11):3398–3413, 2012.
- [5] S. Hermeth, G. Staffelbach, L. Y. M. Gicquel, and T. Poinsot. LES evaluation of the effects of equivalence ratio fluctuations on the dynamic flame response in a real gas turbine combustion chamber. *Proceedings of the Combustion Institute*, 34(2):3165–3173, 2013.
- [6] H. M. Altay, R. L. Speth, D. E. Hudgins, and A. F. Ghoniem. Flame–vortex interaction driven combustion dynamics in a backward-facing step combustor. *Combustion and Flame*, 156(5):1111–1125, 2009.
- [7] S. Hong, S. J. Shanbhogue, R. L. Speth, and A. F. Ghoniem. On the phase between pressure and heat release fluctuations for propane/hydrogen flames and its role in mode transitions. *Combustion and Flame*, 160(12):2827–2842, 2013.
- [8] K. Manoharan and S. Hemchandra. Absolute/convective instability transition in a backward facing step combustor: Fundamental mechanism and influence of density gradient. *Journal of Engineering for Gas Turbines and Power*, 137(2):021501, 2015.

- [9] M. de la Cruz García, E. Mastorakos, and A. P. Dowling. Investigations on the self-excited oscillations in a kerosene spray flame. *Combustion and Flame*, 156(2):374–384, 2009.
- [10] S. Tachibana, K. Saito, T. Yamamoto, M. Makida, T. Kitano, and R. Kurose. Experimental and numerical investigation of thermo-acoustic instability in a liquid-fuel aero-engine combustor at elevated pressure: Validity of large-eddy simulation of spray combustion. *Combustion and Flame*, 162(6):2621–2637, 2015.
- [11] B. Franzelli, E. Riber, M. Sanjosé, and T. Poinsot. A two-step chemical scheme for kerosene–air premixed flames. *Combustion and Flame*, 157(7):1364–1373, 2010.
- [12] P. A. Strakey and G. Eggenpieler. Development and validation of a thickened flame modeling approach for large eddy simulation of premixed combustion. *Journal of Engineering for Gas Turbines and Power*, 132(7):071501, 2010.
- [13] F. Charlette, C. Meneveau, and D. Veynante. A power-law flame wrinkling model for LES of premixed turbulent combustion Part I: non-dynamic formulation and initial tests. *Combustion and Flame*, 131(1):159–180, 2002.
- [14] J.-P. L egier, T. Poinsot, and D. Veynante. Dynamically thickened flame LES model for premixed and non-premixed turbulent combustion. *Proceedings of the summer program*, 157–168, 2000.
- [15] P. Moin, K. D. Squires, W. H. Cabot, and S. Lee. A dynamic subgrid-scale model for compressible turbulence and scalar transport. *Physics of Fluids*, 3(11):2746–2757, 1991.
- [16] C. D. Pierce and P. Moin. A dynamic model for subgrid-scale variance and dissipation rate of a conserved scalar. *Physics of Fluids*, 10(12):3041–3044, 1998.
- [17] F. Proch and A. M. Kempf. Numerical analysis of the Cambridge stratified flame series using artificial thickened flame LES with tabulated premixed flame chemistry. *Combustion and Flame*, 161(10):2627–2646, 2014.

- [18] A. Rittler, F. Proch, and A. M. Kempf. LES of the Sydney piloted spray flame series with the PFGM/ATF approach and different sub-filter models. *Combustion and Flame*, 162(4):1575–1598, 2015.
- [19] D. A. Smith and E. E. Zukoski. Combustion instability sustained by unsteady vortex combustion. *AIAA Paper*, AIAA 85:1248, 1985.
- [20] V. Moureau, C. Bérat, and H. Pitsch. An efficient semi-implicit compressible solver for large-eddy simulations. *Journal of Computational Physics*, 226(2):1256–1270, 2007.
- [21] X.-D. Liu, S. Osher, and T. Chan. Weighted essentially non-oscillatory schemes. *Journal of Computational Physics*, 115(1):200–212, 1994.
- [22] R. J. Kee, G. Dixon-Lewis, J. Warnatz, M. E. Coltrin, J. A. Miller, and H. K. Moffat. A fortran computer code package for evaluation of gas-phase multi-component transport properties. *Sandia Report*, SAND86:8246, 1986.
- [23] R. J. Kee, G. Dixon-Lewis, J. Warnatz, M. E. Coltrin, J. A. Miller, and H. K. Moffat. A fortran chemical kinetic package for the analysis of gas phase chemical kinetic. *Sandia Report*, SAND89:8009B, 1989.
- [24] A. F. Ghoniem, S. Park, A. Wachsman, A. Annaswamy, D. Wee, and H. M. Altay. Mechanism of combustion dynamics in a backward-facing step stabilized premixed flame. *Proceedings of the Combustion Institute*, 30(2):1783–1790, 2005.
- [25] C. T. Crowe, M. P. Sharma, and D. E. Stock. The particle-source-in cell (PSI-CELL) model for gas-droplet flows. *Journal of Fluids Engineering*, 99(2):325–332, 1977.
- [26] H. Moriai, R. Kurose, H. Watanabe, Y. Yano, F. Akamatsu, and S. Komori. Large-eddy simulation of turbulent spray combustion in a subscale aircraft jet engine combustor—predictions of NO and soot concentrations. *Journal of Engineering for Gas Turbines and Power*, 135(9):091503, 2013.

Nomenclature

<p>A : Pre-exponential factor</p> <p>c_p : Specific heat capacity [J/(K kg)]</p> <p>D : Diffusion coefficient [m²/s]</p> <p>E : Efficiency function [-]</p> <p>E_a : Activation energy [J/mol]</p> <p>F : Flame thickening factor [-]</p> <p>f : Correction function [-]</p> <p>G° : Gibbs free energy [J/kg]</p> <p>h : Enthalpy [J/kg]</p> <p>n : Reaction exponent [-]</p> <p>P : Pressure [Pa]</p> <p>Q : Heat release rate [J/s]</p> <p>q : Local heat release rate [J/(m³ s)]</p> <p>R : Gas constant [J/(K mol)]</p> <p>ri : Integrand of local Rayleigh Index [1/m³]</p> <p>RI : Local Rayleigh Index [1/m³]</p> <p>S : Source term</p> <p>T : Temperature [K]</p> <p>\mathbf{t} : Stress tensor including SGS stress [N/m²]</p> <p>\mathbf{u} : Velocity [m/s]</p> <p>W : Mole weight [kg/mol]</p> <p>Y : Mass fraction [-]</p>	<p>β : Temperature exponent [-]</p> <p>θ : Phase [rad]</p> <p>λ : Thermal conductivity [W/(m K)]</p> <p>ρ : Density [kg/m³]</p> <p>ϕ : Equivalence ratio [-]</p> <p>$\dot{\omega}$: Reaction rate [mol/s]</p> <p>Subscripts</p> <p><i>avg</i> : Averaged value</p> <p><i>comb</i> : Combustion</p> <p>k : Species k</p> <p>t : Turbulent diffusion</p>
--	---

Chapter 4

DNS of flashback in a channel flow

4.1 Introduction

In the previous chapter, the mechanism underlying combustion instability and the effect of the combustion condition on combustion instability were investigated. In this chapter, the effect of a pressure oscillation caused by combustion instability on flashback characteristics in a channel flow is investigated using DNS.

Flashback is a transient upstream propagation of a flame and often occurs in combustors using fuels that have high burning velocity such as hydrogen. Flashback has a risk of causing a serious accident, and therefore, has been studied experimentally and numerically [1–5].

Mayer et al. [1] performed experiments of flashback in a swirl burner using CH_4 , CH_4/H_2 mixtures, and pure H_2 , and investigated the conditions such as fuel components and equivalence ratio in which the flashback occurs. Eichler et al. [2] also performed experiments of flashback in a wall boundary layer and investigated the flame structures. However, it is difficult to measure a number of physical characteristics simultaneously, and detail mechanisms of flashback such as the relationship between flame and turbulence have not been sufficiently investigated. Similarly, the computational cost of numerical simulations considering detailed reactions are very high, and therefore, the underlying mechanism is still not well examined numerically, neither. Recently, Gruber et al. [3] per-

formed DNS of flashback. They discussed the flame structure in detail and investigated the effect of ambient pressure on flashback speed. In addition, they proposed a mean flame shape model by using the DNS results [4]. However, since the ambient pressure was static, the effect of a pressure oscillation often caused by combustion instability [6], which sometimes induces the flashback, was not considered.

In this chapter, the effect of a pressure oscillation that is caused by a virtual combustion instability on the flashback characteristics in a turbulent channel flow is investigated using DNS. In addition, the interaction of the flame with the turbulent flow structure is examined in detail. Hydrogen is used as the fuel, and the detailed reaction model that considers 9 chemical species and 20 reactions [7] is used for the calculation of the reaction.

4.2 Numerical simulation

4.2.1 Governing equations

The governing equations are the conservation equations of mass, momentum, energy, and mass of chemical species as

$$\frac{\partial \rho}{\partial t} + \nabla \cdot (\rho \mathbf{u}) = 0, \quad (4.1)$$

$$\frac{\partial \rho \mathbf{u}}{\partial t} + \nabla \cdot (\rho \mathbf{u} \mathbf{u}) = -\nabla P + \nabla \cdot \boldsymbol{\tau}, \quad (4.2)$$

$$\frac{\partial \rho h}{\partial t} + \nabla \cdot (\rho h \mathbf{u}) = \nabla \cdot \left[\rho D_h \left\{ \nabla h - \sum_k (h_k \nabla Y_k) \right\} - \rho \sum_k h_k Y_k \mathbf{V}_k \right] + \boldsymbol{\tau} \cdot \nabla \mathbf{u}, \quad (4.3)$$

$$\frac{\partial \rho Y_k}{\partial t} + \nabla \cdot (\rho Y_k \mathbf{u}) = -\nabla \cdot (\rho Y_k \mathbf{V}_k) + S_{comb,k}, \quad (4.4)$$

and the equation of state for ideal gas. Here ρ is the density, \mathbf{u} the velocity, P the pressure, h the enthalpy, and Y_k the mass fraction of species k . D_h is the thermal diffusivity given by $\rho D_h = \lambda/c_p$. Here λ and c_p are the heat conductivity and the specific heat capacity, respectively. $\boldsymbol{\tau}$ the stress tensor. \mathbf{V}_k is the diffusion velocity of species k calculated as

$$\nabla X_k = \sum_j \left(\frac{X_k X_j}{D_{kj}} \right) (\mathbf{V}_j - \mathbf{V}_k). \quad (4.5)$$

Here X_k is the mole fraction of species k and D_{kj} the diffusion coefficient between species k and j . $S_{comb,k}$ is the source term due to the reaction described later.

4.2.2 Reaction model

Hydrogen is used as the fuel, and for the reaction, the detailed reaction model that considers 9 chemical species and 20 reactions [7] is used.

4.2.3 Computational details

Fig. 4.1(a) shows the computational grid. The domain consists of two regions, “Channel flow region” and “Buffer region”. The flashback phenomenon is reproduced in the “Channel flow region”, and the “Buffer region” is introduced to remove the effects of outlet

boundary conditions on flashback phenomenon. As the inlet boundary of the “Channel flow region” and outlet boundary condition of the “Buffer region”, NSCBC [8, 9] is used.

Fig. 4.1(b) shows the computational conditions of “Channel flow region”. In order to reproduce a realistic flashback flame in a fully-developed wall-bounded turbulent flow, two computations using two computational domains are combined in this region. In the upstream computational domain for one computation, a fully-developed wall-bounded turbulent flow is generated by imposing a periodic boundary condition in the x -direction. In the downstream computational domain for the other computation, on the other hand, the flashback phenomenon in the fully-developed wall-bounded turbulent flow is simulated by giving the outflow characteristics of the upstream computational domain as the inflow characteristics. The no-slip iso-thermal (750 K) boundary condition is applied in the y -direction and the periodic boundary condition is applied in the z -direction. The flame is ignited at the y - z plane at the downstream end of the flashback region by imposing an artificial reaction 100 ms after the initiation of turbulent production. The Reynolds numbers based on the channel width and the mean streamwise velocity is approximately 3500, and that based on the channel half width and the friction velocity is approximately 120. The initial gas temperature, pressure, and equivalence ratio are 750 K, 0.1 MPa, and 1.5, respectively. The laminar burning velocity in this condition is estimated to be 14.0 m/s [10]. All these flow conditions are set to close to those of the previous work by Gruber et al. [3]. Table 4.1 shows the computational conditions. In this study, computations are performed for three cases: Case 1: without a pressure oscillation using fine grids, Case 2: without a pressure oscillation using coarse grids, and Case 3: with a pressure oscillation (given by a sine-wave from the outlet side) using coarse grids. The intensity of the pressure oscillation is 1.5 kPa (1.5% of the average pressure). This magnitude is chosen based on that caused by combustion instability in a real combustor [11], and the sine-wave is given as a fundamental wave, which is generally used in previous studies of combustion instability [12].

The staggered grid is used for the computational grid. The grid resolutions of the flashback region for Case 1 are 50 μm in the x -, y -, and z -directions (Δx^+ , Δy^+ , Δz^+ =

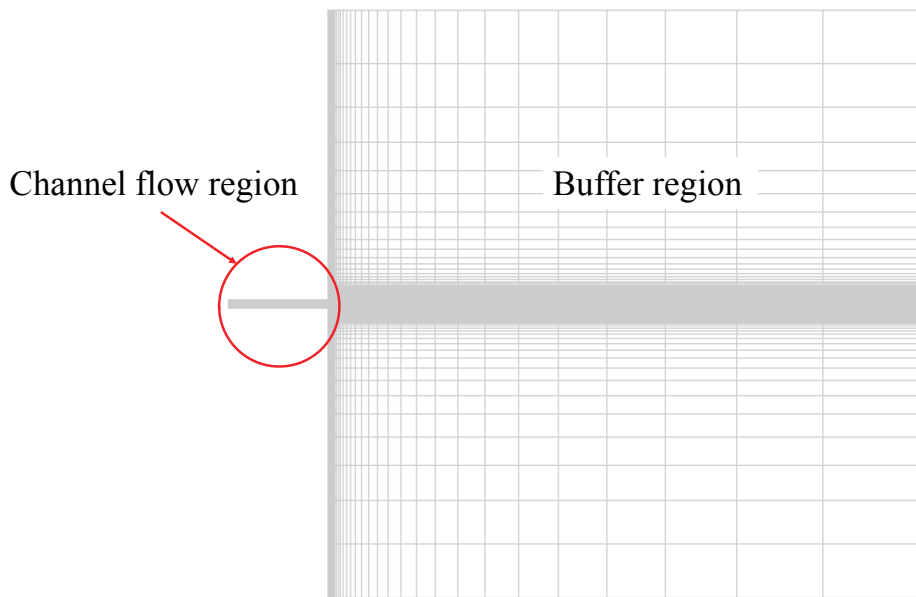
Table 4.1: Computational conditions.

Cases	Number of computational grids	Pressure oscillation
1	0.4 billion	–
2	0.1 billion	–
3	0.1 billion	1.5 %, 1000 Hz

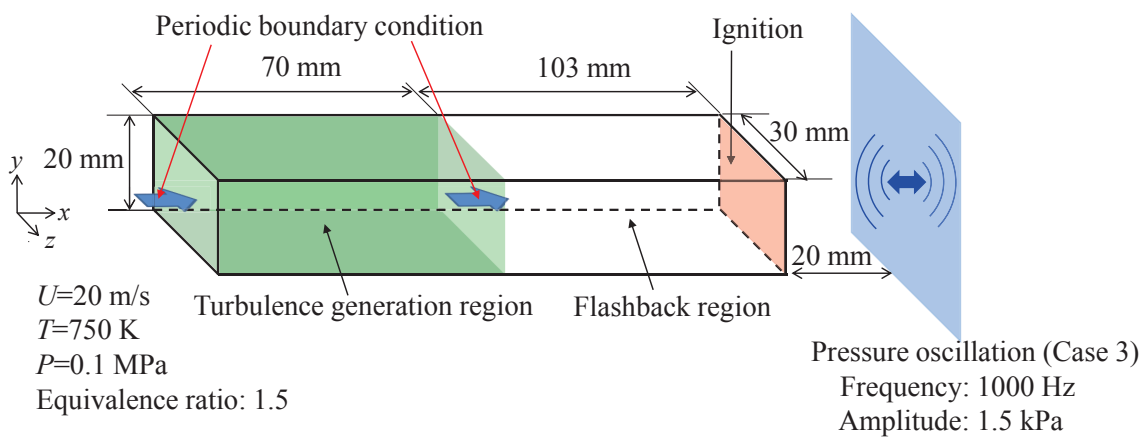
0.6), while those for Cases 2 and 3 are $100 \mu\text{m}$ in the x - and z -directions ($\Delta x^+, \Delta z^+ = 1.2$), and $50\text{--}100 \mu\text{m}$ from the wall to the center of the channel in the y -direction ($\Delta y^+ = 0.6\text{--}1.2$). The wall-unit lengths in the flashback region in the x -, y -, and z -directions are approximately $800 \times 320 \times 480$ for all cases. For the turbulence generation region, the grid resolution in the x -direction is $700 \mu\text{m}$ ($\Delta x^+ = 8$) for all cases. The total number of grid points for Case 1 is approximately 0.4 billion, and for Cases 2 and 3 is approximately 0.1 billion. The time resolution for Case 1 is approximately 4.5×10^{-8} , and for Cases 2 and 3 is approximately 9×10^{-8} s. The chemical reactions are calculated by using Multi-timescale (MTS) method [13] in every time step with a minimum time resolution of 1×10^{-9} s for all cases.

The spatial derivatives of the momentum equation are approximated by the fourth-order accurate central difference scheme. For the convection terms of energy and mass fractions of chemical species, the QUICK scheme is employed. The second-order accurate central difference scheme is used for the other terms. The fractional-step method for compressible flows is used as the computational algorithm [14], and the third-order explicit Runge–Kutta method is used for the time-advancement computation of the convection terms. The thermo physical properties and transport coefficients are obtained from CHEMKIN [15, 16].

The CPU time for Case 1 is about 5.3 million h (520 h on the wall-clock time) on K computer (Fujitsu SPARC64TM VIIIfx processor, 10240 cores).



(a) Computational grid



(b) Computational conditions (Channel flow region)

Figure 4.1: Computational grid and conditions.

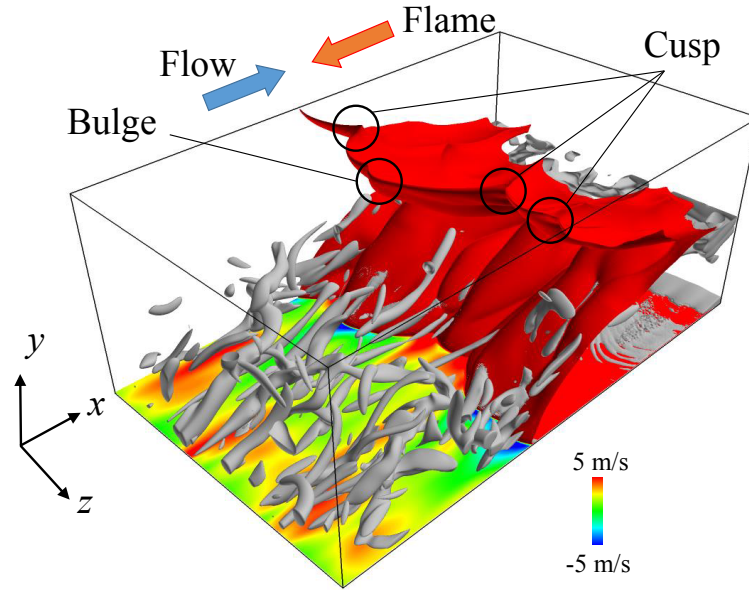
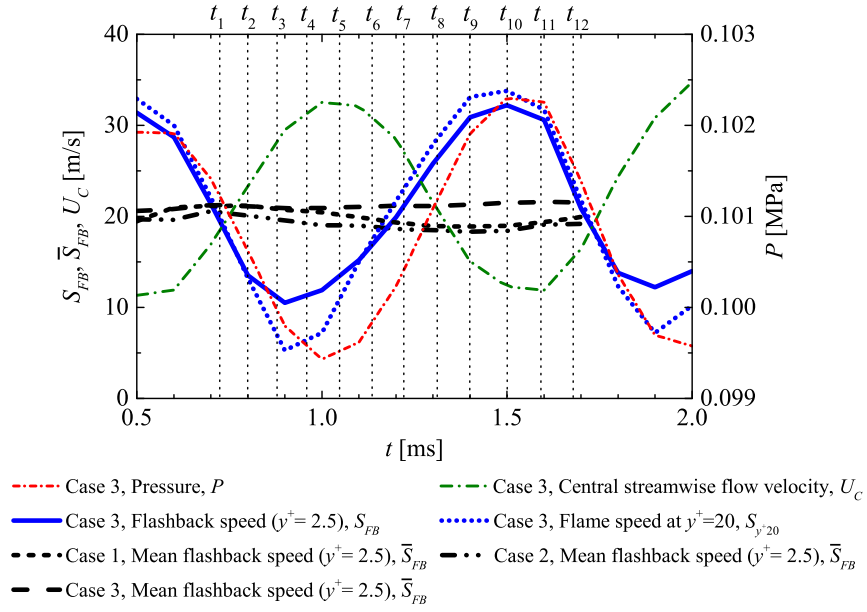


Figure 4.2: Instantaneous distributions of iso-surfaces of temperature at 1200 K and second invariant of velocity gradient tensor, and streamwise flow velocity on the x - z plane at $y^+ = 2.5$, U_{wall} ($t = 1.75$ ms, Case 2).

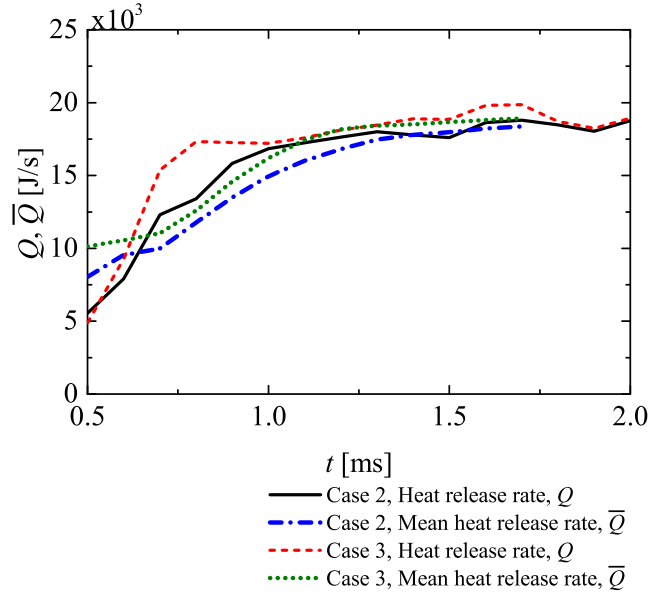
4.3 Results and discussion

4.3.1 Effect of a pressure oscillation

Fig. 4.2 shows the instantaneous distributions of iso-surfaces of temperature at 1200 K and second invariant of velocity gradient tensor, and streamwise flow velocity on the x - z plane at $y^+ = 2.5$, U_{wall} , for Case 2. It is observed that the flame surface is wrinkled by the streak structure in the wall turbulence, and flame bulge and cusp have formed. This feature of the flashback was also observed in the previous study [3]. It was confirmed that the approaching value of the flashback speed for Case 2 (coarse grids) agreed well with those for Case 1 (fine grids) and the previous study [3] (see Fig. 4.3 described below). Therefore, the discussion below is conducted with the results for Cases 2 and 3 (coarse grids) to save the computational cost. Here the flashback speed is defined by the propagation speed of flame at $y^+ = 2.5$. This value is calculated by detecting the



(a) P , U_C , S_{FB} , \bar{S}_{FB}



(b) Q , \bar{Q}

Figure 4.3: Time variations of pressure, P , central streamwise flow velocity, U_C , and flashback speed, S_{FB} , for Case 3, mean flashback speeds, \bar{S}_{FB} , for Cases 1–3, and heat release rate, Q , and mean heat release rate, \bar{Q} , for Cases 2 and 3.

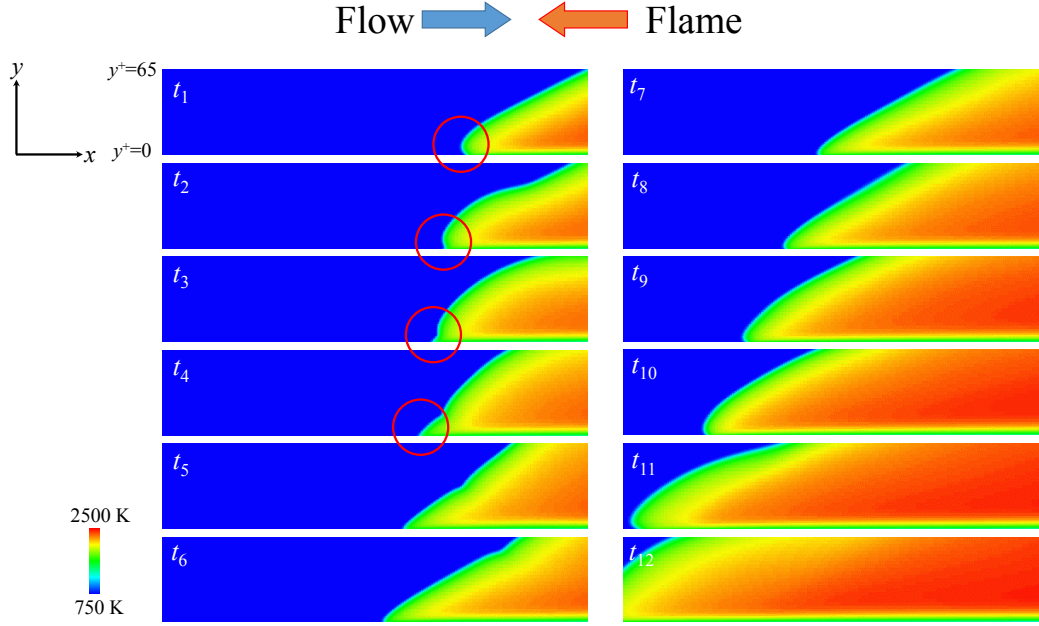


Figure 4.4: Time variation of instantaneous temperature distribution on the x - y plane at $z = 15$ mm at $t = t_1$ - t_{12} in Fig .3 (Case 3).

spanwise (z -direction) mean position of the iso-surface of gas temperature (1200 K) at $y^+ = 2.5$ in each time step.

Fig. 4.3 shows the time variations of pressure, P , central streamwise flow velocity, U_C , and flashback speed evaluated at $y^+ = 2.5$, S_{FB} , for Case 3, mean flashback speeds, \bar{S}_{FB} , for Cases 1-3 and heat release rate, Q , and mean heat release rate, \bar{Q} , for Cases 2 and 3. In this figure, the time variation of flame speed at an upper location of $y^+ = 20$, $S_{y^+=20}$, for Case 3 is also shown. Here the flame speed is defined by the propagation speed of flame at $y^+ = 20$. This value is calculated by detecting the spanwise (z -direction) mean position of the iso-surface of gas temperature (1200 K) at $y^+ = 20$ in each time step. The heat release rate is the global value of the whole domain. Mean values are calculated by taking an average over one cycle of the pressure oscillation (1.0 ms) at each time step (e.g., the value at $t = 1.0$ ms is calculated by taking the average from $t = 0.5$ to 1.5 ms, and the value at $t = 1.1$ ms is calculated by taking the average from $t = 0.6$ to 1.6 ms). P and U_C are the values at the center of the inlet plane of the

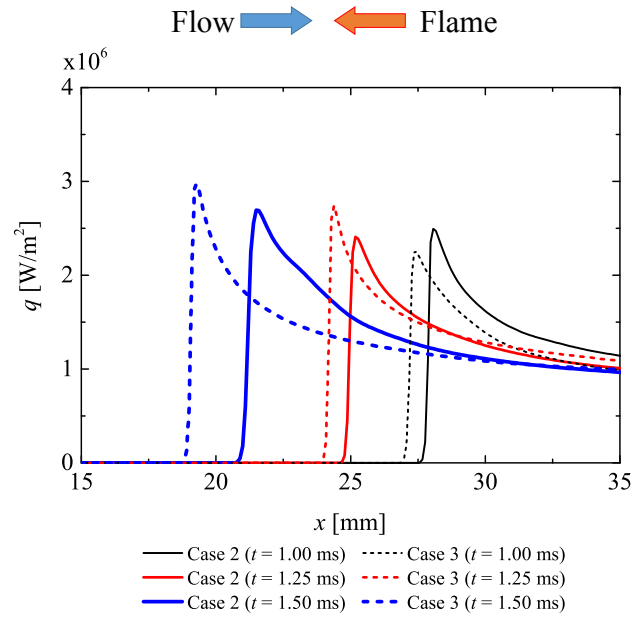


Figure 4.5: Time variation of instantaneous heat flux, q , on the x - y plane at $z = 15$ mm at $t = 1.00$, 1.25 , and 1.50 ms (Cases 2 and 3).

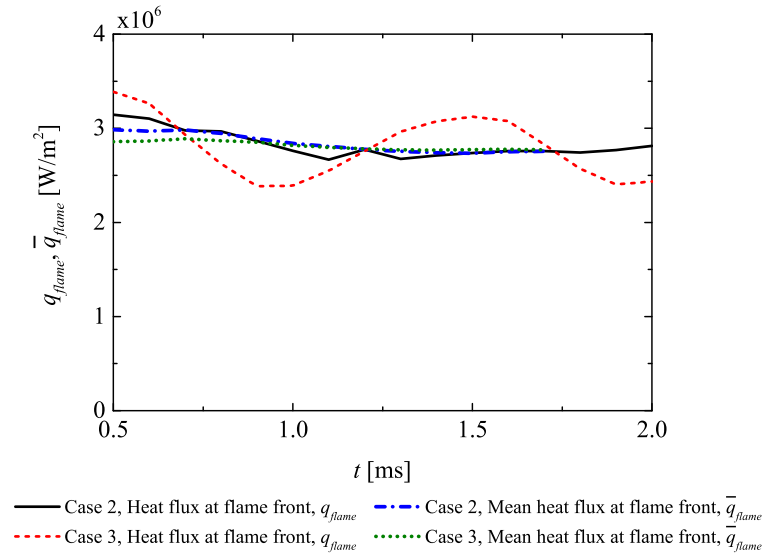


Figure 4.6: Time variation of space-averaged (along flame front) heat flux, \bar{q} , (Cases 2 and 3).

flashback region. It is found that the pressure oscillation generates the oscillations of U_C , S_{FB} , and Q , and tends to increase \bar{S}_{FB} and \bar{Q} . This increase in \bar{S}_{FB} is due to the fact that, in the region close to the wall at $y^+ = 2.5$, S_{FB} is easily accelerated by the rise in pressure, but largely unaffected by the subsequent fall in pressure. This phenomenon is explained as follows. In the flashback deceleration period ($t = t_1-t_6$), S_{FB} is clearly higher than S_{y+20} . This is due to the fact that the increase in U_{wall} caused by the drop in pressure is smaller than that of U_C . This is because the change of the velocity near the wall is suppressed by the viscous friction drag, and therefore, S_{FB} in the flashback deceleration period is unaffected by U_C . In the flashback acceleration period ($t = t_7-t_{12}$), in contrast, the difference between S_{FB} and S_{y+20} is smaller than that in the flashback deceleration period ($t = t_1-t_6$), though S_{y+20} is a little higher than S_{FB} . This is because the flame close to the wall is accelerated by the heat diffused from the flame much more accelerated in the upper region. The above analysis of deceleration period is supported by Fig. 4.4, which shows the time variation of instantaneous temperature distribution on the x - y plane. As shown by the red circle markers, the flame top away from the wall at $t = t_1-t_2$ comes to touch the wall at $t = t_3-t_4$ as the pressure decreases.

Fig. 4.5 shows the comparison of the time variation of instantaneous heat flux, q , on the x - y pane at $z = 15$ mm at $t = 1.00, 1.25,$ and 1.50 ms between Cases 2 and 3. The heat flux is defined as

$$q = -\lambda \left. \frac{\partial T}{\partial y} \right|_{wall}. \quad (4.6)$$

Here λ is the thermal conductivity. The temperature gradient at the wall is obtained by using the values of the grid points at the wall and their immediate neighbors in the vertical (y -) direction. Independent of the time, q dramatically increases towards the flame front, where it reaches the maximum value, and then gradually decreases towards downstream end. Furthermore, compared to Case 2, the maximum value of q at the flame front tends to markedly oscillate in time for Case 3. In order to clarify the interaction between the q and pressure oscillations, the time variation of the heat flux averaged along the flame front indicating the peak heat flux, q_{flame} , for Cases 2 and 3 are compared in Fig. 4.6. In the figure, the mean heat flux at flame front, \bar{q}_{flame} , calculated

by the same method with mean flashback speed in Fig. 4.3 is also shown. It is evident that q_{flame} for Case 3 is strongly affected by the pressure oscillation, but \bar{q}_{flame} is almost the same as that of Case 2. The comparison of Figs. 4.3 and 4.6 shows that q_{flame} , P , and S_{FB} become the maxima in the same time period (see at $t = 1.5$ ms in Fig. 4.3). This is considered to be due to the fact that at this time, the flame temperature close to the wall is increased by the heat diffused from the flame in the upper region (see at $t = t_{10}$ in Fig. 4.4), as described above.

4.3.2 Interaction of flame with turbulent flow structure

Fig. 4.7 shows the instantaneous distributions of iso-surfaces of temperature at 1200 K and secondary invariant of velocity gradient tensor in side and bottom views at $t = 1.75$ ms for Case 2. Here in the bottom view, the iso-surfaces of temperature close to the wall are removed to show more clearly the secondary invariant of velocity gradient tensor. The instantaneous distributions of streamlines (black line) and iso-lines of temperature at 1200 K (red line) on the x - y plane at $z = 21$ mm, the y - z plane at $x = 26$ mm, and the x - z plane at $y = 4.5$ mm at the same time as Fig. 4.7 are shown in Fig. 4.8. The x - y plane is located at the top of a bulge. In front of the flame surfaces in the unburned region, the turbulent eddies and streamlines are observed to be bent along the flame surfaces. This is attributed to the fact that the thermal expansion in the flame induces a flow towards the center of the channel. Furthermore, it is found that whereas most of the turbulent eddies are suppressed and vanished behind the flame as reported in previous studies for turbulent premixed flame [17, 18], other turbulent eddies are generated again in a form of longitudinal eddies behind the flame only at the cusps and center of the channel where the upper and lower flames meet. In order to clarify the mechanism, following transport equation for the turbulent kinetic energy is introduced [19].

$$\frac{\partial \bar{\rho} \tilde{K}}{\partial t} = -\frac{\partial}{\partial x_j} \bar{\rho} \tilde{u}_j \tilde{K} - \overline{u_k'' \frac{\partial p}{\partial x_k}} - \overline{\rho u_j'' u_k'' \frac{\partial \tilde{u}_k}{\partial x_j}} - \frac{1}{2} \frac{\partial}{\partial x_j} \overline{\rho u_j'' u_k''^2} + \overline{u_k'' \frac{\partial \tau_{kj}}{\partial x_j}}. \quad (4.7)$$

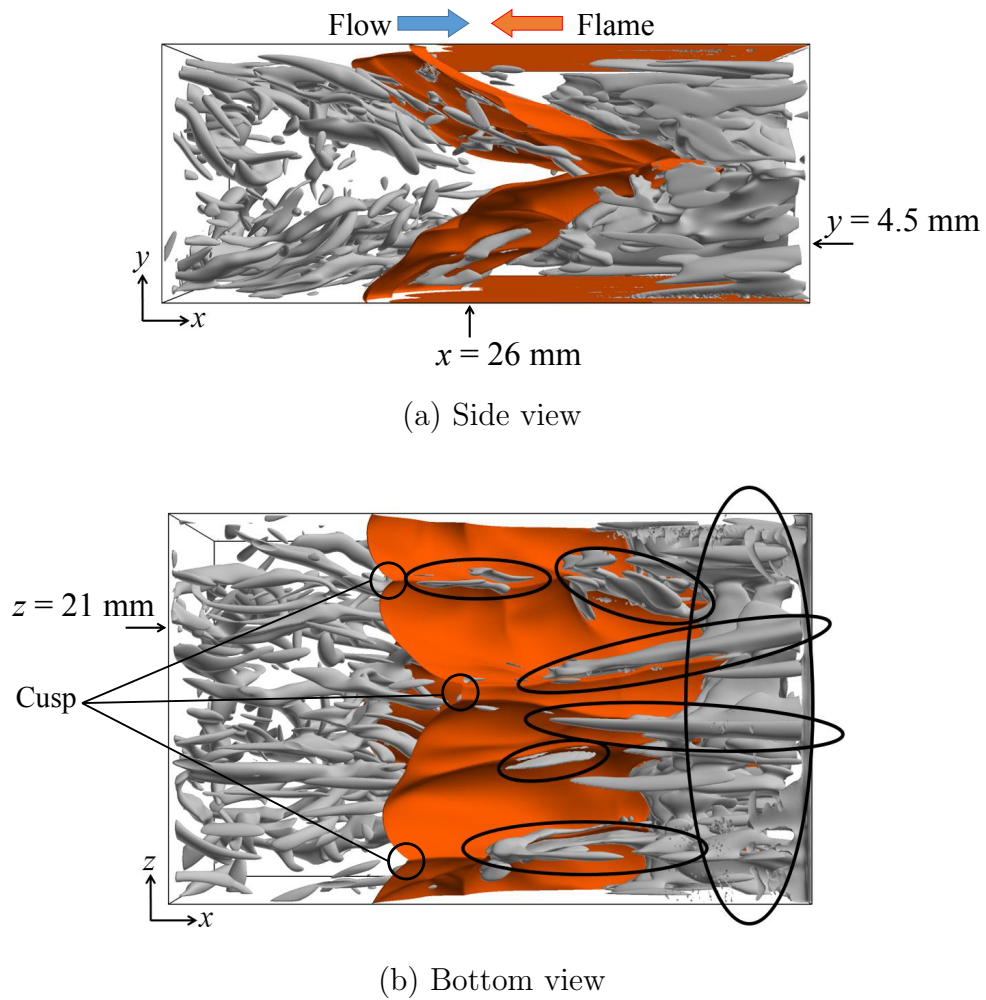
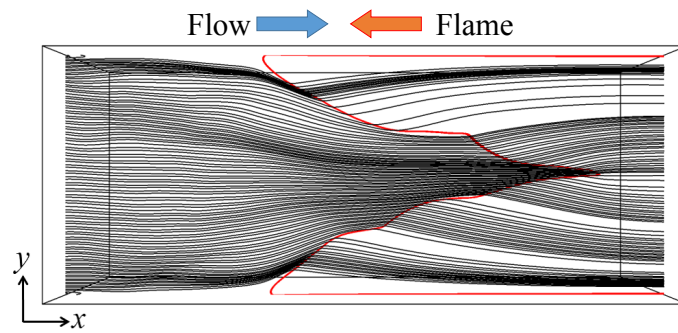
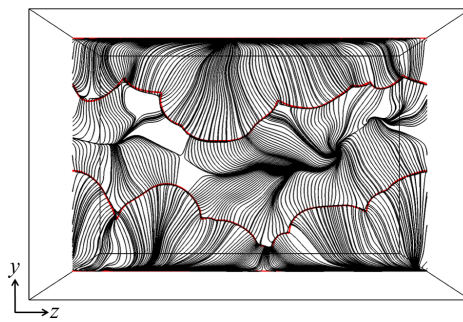


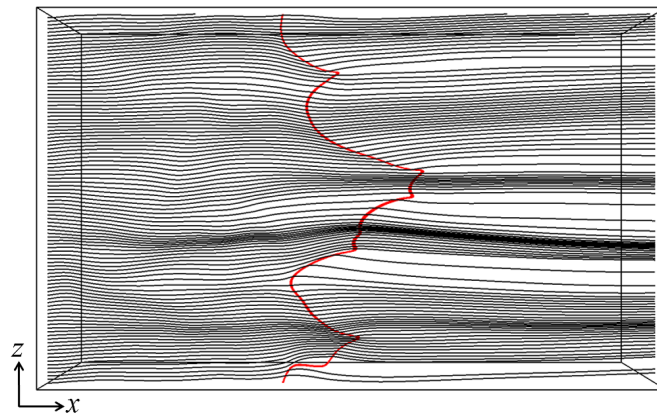
Figure 4.7: Instantaneous distributions of iso-surfaces of temperature at 1200 K and second invariant of velocity gradient tensor in side and bottom views ($t = 1.75$ ms, Case 2).



(a) On the x - y plane at $z = 21$ mm



(b) On the y - z plane at $x = 26$ mm



(c) On the x - z plane at $y = 4.5$ mm

Figure 4.8: Instantaneous distributions of streamlines (black line) and iso-lines of temperature at 1200 K (red line) ($t = 1.75$ ms, Case 2).

Here the overbar, $\bar{\cdot}$, and, $\widetilde{\cdot}$, donate the Reynolds- and Favre-averaged values, respectively, and $''$ indicates the variation from the Favre-averaged value. K is the turbulent kinetic energy given as

$$K = \sum_j \frac{1}{2} \widetilde{u_j''^2}. \quad (4.8)$$

The third term on the right-hand side,

$$\begin{aligned} \dot{k} = & -\overline{\rho u_j'' u_k''} \frac{\partial \widetilde{u_k}}{\partial x_j} = -\overline{\rho u'' u''} \frac{\partial \widetilde{u}}{\partial x} - \overline{\rho v'' u''} \frac{\partial \widetilde{v}}{\partial x} - \overline{\rho w'' u''} \frac{\partial \widetilde{w}}{\partial x} \\ & - \overline{\rho u'' v''} \frac{\partial \widetilde{u}}{\partial y} - \overline{\rho v'' v''} \frac{\partial \widetilde{v}}{\partial y} - \overline{\rho w'' v''} \frac{\partial \widetilde{w}}{\partial y} \\ & - \overline{\rho u'' w''} \frac{\partial \widetilde{u}}{\partial z} - \overline{\rho v'' w''} \frac{\partial \widetilde{v}}{\partial z} - \overline{\rho w'' w''} \frac{\partial \widetilde{w}}{\partial z}, \end{aligned} \quad (4.9)$$

represents the turbulent production term.

Fig. 4.9 shows the distribution of magnitude of the turbulent production term on the x - y plane at $z = 21$ mm, and Fig. 4.10 shows the distributions of magnitudes of each term in the turbulent production term on the same x - y plane. Here the black lines indicate the iso-lines of averaged temperature at 1200 K. The Favre- and Reynolds-averaged terms are calculated by taking time-average for 0.2 ms and space-average for 1 mm in spanwise (z -) direction at each position. The turbulent production is negative in the wide region behind the flame but is locally positive at the center of the channel where the upper and lower flames meet (the circle A in Fig. 4.9). These negative and positive regions appear to correspond, respectively, to the regions where the turbulent eddies are suppressed and generated in Fig. 4.7(a). Furthermore, it is clear that the negative and positive turbulent productions are attributed to the variations of the $-\overline{\rho u'' u''} \frac{\partial \widetilde{u}}{\partial x}$ and $-\overline{\rho u'' v''} \frac{\partial \widetilde{u}}{\partial y}$ in \dot{k} , respectively. Fig. 4.11, which shows the distributions of Favre-averaged velocities in the x -, y -, and z -directions, suggests that the acceleration of the streamwise velocity owing to the thermal expansion is extremely remarkable. Therefore, it is considered that the negative and positive values for the \dot{k} are attributed to the remarkable acceleration of the streamwise velocity (i.e., the increase in $\frac{\partial \widetilde{u}}{\partial x}$) and the strong fluid shear on the x - y plane caused by this accelerated streamwise velocity (i.e., the increase in the absolute value of $-\overline{\rho u'' v''}$), respectively.

On the other hand, the generation of the turbulent eddies behind the cusps are similarly explained by the distributions of magnitudes of the turbulent production term, and each term in the turbulent production term on the $x-z$ plane at $y = 4.5$ mm in Figs. 4.12 and 4.13. Here the black lines indicate the iso-lines of averaged temperature at 1200 K. The comparison to Fig. 4.7(b) illustrates that the locations of the generated turbulent eddies behind the cusps roughly correspond to those of the high values of the $-\overline{\rho u'' v''} \frac{\partial \tilde{u}}{\partial y}$ in \dot{k} (the circle B in Fig. 4.13), suggesting that similar to the turbulent eddies generated behind the flame at the center of the channel where the upper and lower flames meet, the turbulent eddies behind flame at the cusps are generated by the strong fluid shear on the $x-y$ plane caused by the thermal expansion.

This interaction of the flame with the turbulent flow structure was also observed for the case with the pressure oscillation (Case 3).

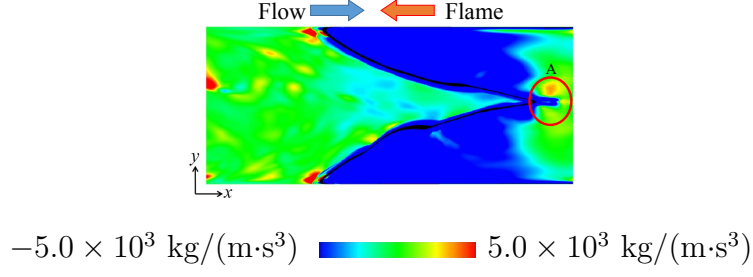


Figure 4.9: Distribution of magnitude of turbulent production term (third term on right-hand side in Eq. (4.7)) on the x - y plane at $z = 21 \text{ mm}$ ($t = 1.75 \text{ ms}$, Case 2). Black lines indicate iso-lines of averaged temperature at 1200 K.

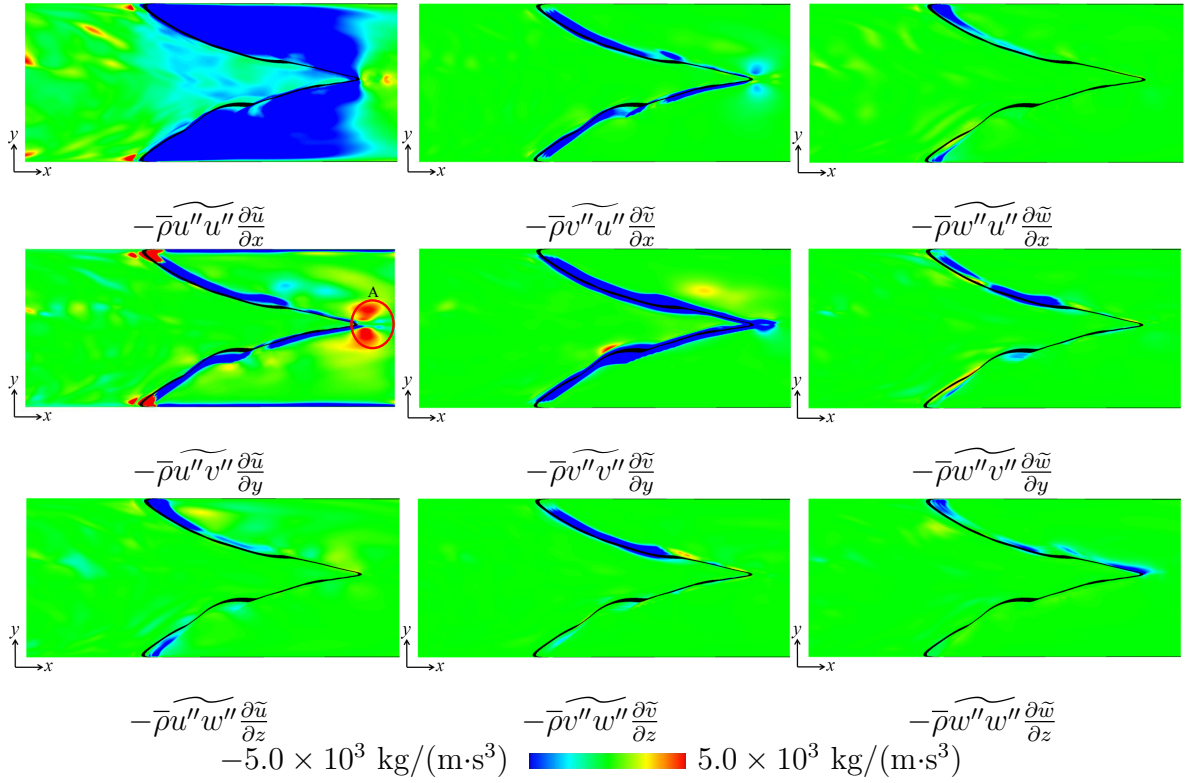
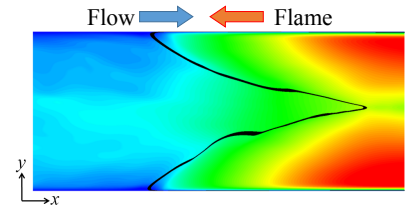
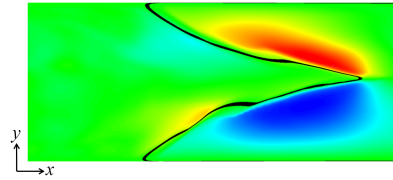


Figure 4.10: Distributions of magnitudes of each term in turbulent production term on the x - y plane at $z = 21 \text{ mm}$ ($t = 1.75 \text{ ms}$, Case 2). Black lines indicate iso-lines of averaged temperature at 1200 K.



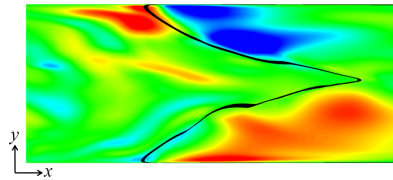
0 m/s 100 m/s

(a) x -direction



-15 m/s 15 m/s

(b) y -direction



-5 m/s 5 m/s

(c) z -direction

Figure 4.11: Distributions of Favre-averaged velocities in the x -, y -, and z -directions on the x - y plane at $z = 21$ mm ($t = 1.75$ ms, Case 2). Black lines indicate iso-lines of averaged temperature at 1200 K.

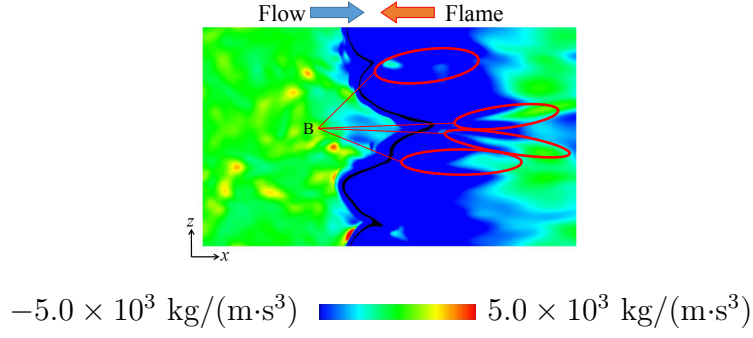


Figure 4.12: Distribution of magnitude of turbulent production term (third term on right-hand side in Eq. (4.7)) on the x - z plane at $y = 4.5$ mm ($t = 1.75$ ms, Case 2). Black lines indicate iso-lines of averaged temperature at 1200 K.

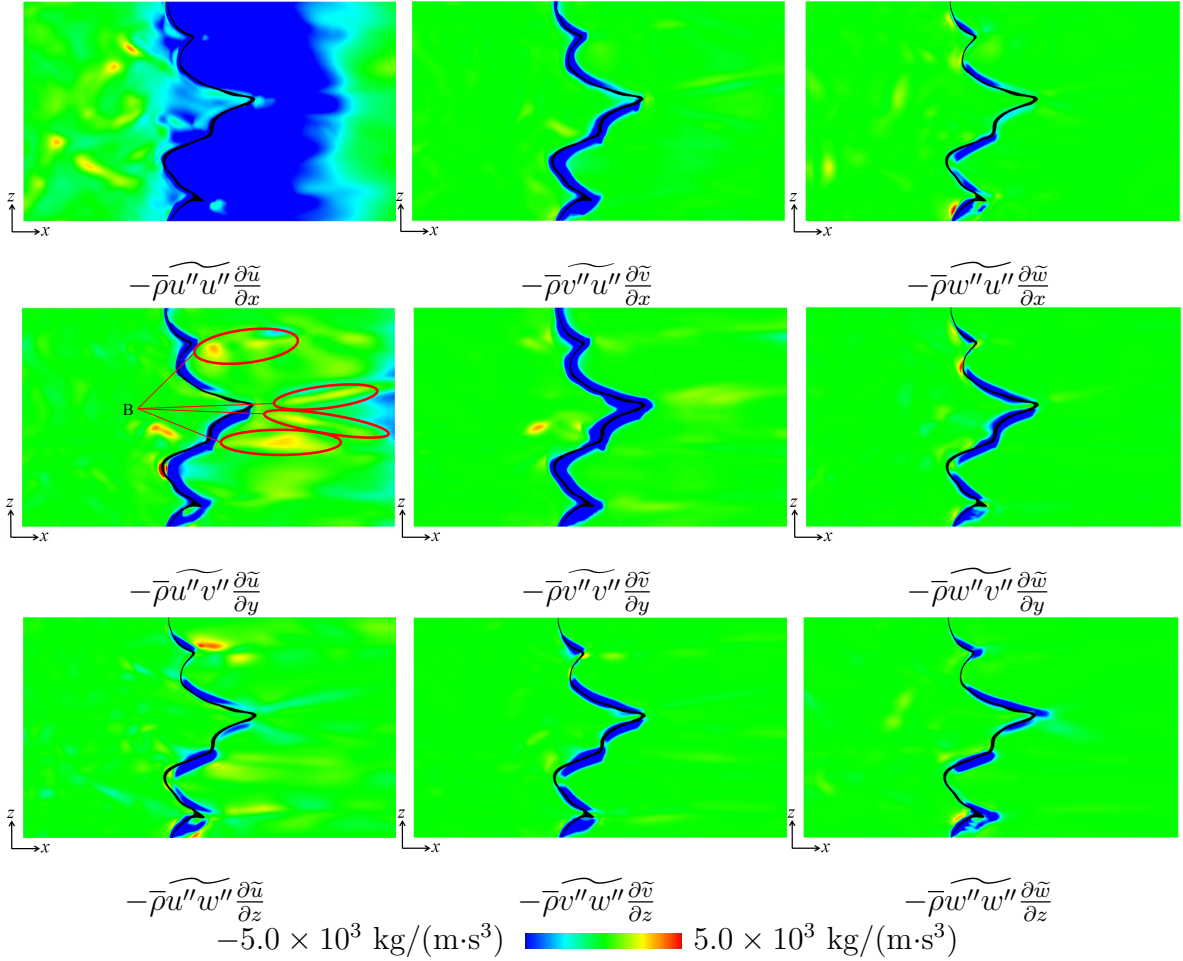


Figure 4.13: Distributions of magnitudes of each term in turbulent production term on the x - z plane at $y = 4.5$ mm ($t = 1.75$ ms, Case 2). Black lines indicate iso-lines of averaged temperature at 1200 K.

4.4 Conclusions

In this chapter, a flashback phenomenon in a turbulent channel flow was reproduced using DNS, and the effect of the pressure oscillation that was caused by a virtual combustion instability on the flashback characteristics was investigated. In addition, the interaction of the flame and the turbulent flow structure was examined in detail. The main results obtained in this study can be summarized as follows.

1. The pressure oscillation strongly affects the flashback characteristics such as flashback speed and heat transfer on the wall, and increases the mean flashback speed because the acceleration of the flashback speed due to the pressure oscillation is greater than its deceleration. This fact indicates that the combustion instability, which often generates a large pressure oscillation in combustors, increases the risk of flashback.
2. Independent of the pressure oscillation, the turbulent eddies passing through the flame tends to be suppressed and vanish due to the acceleration of the streamwise flow caused by thermal expansion. However, other turbulent eddies are generated again in the form of longitudinal eddies behind the flame only at the cusps and the center of the channel where the upper and lower flames meet, because of the strong fluid shear owing to the thermal expansion.

References

- [1] C. Mayer, J. Sangl, T. Sattelmayer, T. Lachaux, and S. Bernero. Study on the operational window of a swirl stabilized syngas burner under atmospheric and high pressure conditions. *Journal of Engineering for Gas Turbines and Power*, 134(3):031506, 2012.
- [2] C. Eichler, G. Baumgartner, and T. Sattelmayer. Experimental investigation of turbulent boundary layer flashback limits for premixed hydrogen-air flames confined in ducts. *Journal of Engineering for Gas Turbines and Power*, 134(1):011502, 2012.
- [3] A. Gruber, J. H. Chen, D. Valiev, and C. K. Law. Direct numerical simulation of premixed flame boundary layer flashback in turbulent channel flow. *Journal of Fluid Mechanics*, 709:516–542, 2012.
- [4] A. Gruber, A. R. Kerstein, D. Valiev, C. K. Law, H. Kolla, and J. H. Chen. Modeling of mean flame shape during premixed flame flashback in turbulent boundary layers. *Proceedings of the Combustion Institute*, 35(2):1485–1492, 2015.
- [5] Y. Lee, S. A. Korpela, and R. N. Horne. Structure of multi-cellular natural convection in a tall vertical annulus. *Proceedings of 7th International Heat Transfer Conference*, 2:221–226, 1982.
- [6] S. Tachibana, K. Saito, T. Yamamoto, M. Makida, T. Kitano, and R. Kurose. Experimental and numerical investigation of thermo-acoustic instability in a liquid-fuel aero-engine combustor at elevated pressure: Validity of large-eddy simulation of spray combustion. *Combustion and Flame*, 162(6):2621–2637, 2015.
- [7] J. A. Miller and C. T. Bowman. Mechanism and modeling of nitrogen chemistry in combustion. *Progress in Energy and Combustion Science*, 15(4):287–338, 1989.
- [8] T. Poinso and D. Veynante. *Theoretical and numerical combustion*. R. T. Edwards, Inc., 2005.

- [9] T. Poinso and S. K. Lele. Boundary conditions for direct simulations of compressible viscous flows. *Journal of Computational Physics*, 101(1):104–129, 1992.
- [10] H. Pitsch. A C++ computer program for 0D combustion and 1D laminar flame calculations.
- [11] B. Franzelli, E. Riber, L. Y. M. Gicquel, and T. Poinso. Large eddy simulation of combustion instabilities in a lean partially premixed swirled flame. *Combustion and Flame*, 159(2):621–637, 2012.
- [12] K. Sato, E. Knudsen, and H. Pitsch. Study of combustion instabilities imposed by inlet velocity disturbance in combustor using LES. *ASME Turbo Expo 2009: Power for Land, Sea, and Air*, 87–99, 2009.
- [13] X. Gou, W. Sun, Z. Chen, and Y. Ju. A dynamic multi-timescale method for combustion modeling with detailed and reduced chemical kinetic mechanisms. *Combustion and Flame*, 157(6):1111–1121, 2010.
- [14] V. Moureau, C. Bérat, and H. Pitsch. An efficient semi-implicit compressible solver for large-eddy simulations. *Journal of Computational Physics*, 226(2):1256–1270, 2007.
- [15] R. J. Kee, G. Dixon-Lewis, J. Warnatz, M. E. Coltrin, J. A. Miller, and H. K. Moffat. A fortran computer code package for evaluation of gas-phase multi-component transport properties. *Sandia Report*, SAND86:8246, 1986.
- [16] R. J. Kee, G. Dixon-Lewis, J. Warnatz, M. E. Coltrin, J. A. Miller, and H. K. Moffat. A fortran chemical kinetic package for the analysis of gas phase chemical kinetic. *Sandia Report*, SAND89:8009B, 1989.
- [17] M. Tanahashi, M. Fujimura, and T. Miyauchi. Coherent fine-scale eddies in turbulent premixed flames. *Proceedings of the Combustion Institute*, 28(1):529–535, 2000.

- [18] B. Yenerdag, N. Fukushima, M. Shimura, M. Tanahashi, and T. Miyauchi. Turbulence–flame interaction and fractal characteristics of H₂–air premixed flame under pressure rising condition. *Proceedings of the Combustion Institute*, 35(2):1277–1285, 2015.
- [19] N. Swaminathan and K. N. C. Bray. *Turbulent premixed flames*. Cambridge University Press, 2011.

Nomenclature

c_p : Specific heat capacity [J/(K kg)]	λ : Thermal conductivity [W/(m K)]
D : Diffusion coefficient [m ² /s]	ρ : Density [kg/m ³]
h : Enthalpy [J/kg]	$\boldsymbol{\tau}$: Stress tensor [N/m ²]
K : Turbulent kinetic energy [J/kg]	
\dot{k} : Source term of K [J/(m ³ s)]	Subscripts
P : Pressure [N/m ²]	C : Center of channel
q : Heat flux [W/m ²]	$comb$: Combustion
Q : Heat release rate [J/s]	FB : Flashback
S : Flashback or flame speed [m/s]	k : Species k
T : Temperature [K]	y^{+20} : Vertical position of $y^{+} = 20$
\mathbf{u} : Velocity [m/s]	
\mathbf{V} : Diffusion velocity [m/s]	
X : Mole fraction [-]	
Y : Mass fraction [-]	

Chapter 5

Conclusions

5.1 Summary and conclusions

To investigate the mechanism of droplet evaporation and combustion instability, DNS of the evaporation and combustion of fuel droplets, and LES of gas and spray combustion in a back-step flow were performed. In addition, DNS of flashback, which is a transient upstream propagation of a flame often caused by combustion instability, was performed.

In Chapter 2, the characteristics of the evaporation and combustion of fuel droplets for single- and multi-component fuels in a static fluid were described. The effects of ambient pressure, initial gas temperature, and differences in fuel components and combustion reaction on the evaporation characteristics were investigated using DNS for a single and multiple fuel droplets. For the single-component fuels, *n*-heptane and *n*-decane were used, and the one-step global reaction model was used for the calculation of the reaction of *n*-decane. For the multi-component fuels, on the other hand, surrogate fuels of Jet-A (one-component fuel: *n*-decane, two-component fuel: *n*-decane and 1,2,4-trimethylbenzene, three-component fuel: *n*-dodecane, *iso*-octane and toluene) were used. For the calculations of the reactions, the detailed reaction models that considered 113 chemical species and 891 reactions for the one- and two-component fuels, and 273 chemical species and 2322 reactions for the three-component fuel were used, respectively.

In Chapter 3, the characteristics of combustion instability in a back-step flow were

described. LES of gas and spray combustion were performed, and the mechanism underlying combustion instability and the effect of initial droplet diameter on combustion instability were investigated. Methane and kerosene were used as the fuel for gas and spray combustion, respectively. For the calculations of the reactions, the two-step global reaction models were used with the dynamic thickened flame model to incorporate the effects of SGS turbulence on the reactions.

In Chapter 4, the characteristics of flashback in a channel flow were described. The effect of a pressure oscillation that was caused by a virtual combustion instability on the flashback characteristics was investigated using DNS. Hydrogen was used as the fuel, and the detailed reaction model that considered 9 chemical species and 20 reactions was used for the calculation of the reaction.

The main results obtained in this study can be summarized as follows.

1. For droplet evaporation in a static fluid, under the conditions without combustion reaction, the droplet lifetime increases with increasing ambient pressure at lower initial gas temperature but decreases at higher initial gas temperature. This is attributed to a balance of the increase and decrease in droplet evaporation rate in higher ambient pressure conditions. On the other hand, under the conditions with combustion reaction, the effects of ambient pressure, initial gas temperature and the droplet mass loading ratio on the droplet lifetime are similar to those under the conditions without combustion reaction, although the droplet lifetime becomes shorter due to the combustion reaction. However, the droplet lifetime is often shortened by enhanced combustion reaction in the conditions of high ambient pressure and moderately high droplet mass loading ratio.
2. For droplet evaporation and combustion in the static fluid, evaporation of the three-component surrogate fuel of Jet-A becomes faster and slower than those of the one- and two-component surrogate fuels in the initial and subsequent evaporating periods, respectively. This is due to the fact that compared to *n*-decane and 1,2,4-trimethyl-benzene, *iso*-octane and toluene included in the three-component

surrogate fuel have higher volatilities, whereas *n*-dodecane included in the three-component fuel has lower volatility. Differences in the gas temperature evolution among three different surrogate fuels are remarkable right after the ignition, but they become small with time.

3. For gas combustion in the back-step flow, oscillations of pressure, heat release rate and streamwise velocity with the same frequency but different phase are observed, and the spectrum of the pressure oscillation has two peaks whose frequencies agree well with those from a previous experimental study. This confirms that the present LES is capable of capturing precisely the characteristics of combustion instability. The inlet velocity oscillation periodically generates a large vortex near the dump plane and conveys it downstream, and when the large vortex exists near the dump plane, the integrand of the local Rayleigh Index becomes positive. This suggests that combustion instability is driven by the large vortex near the dump plane.
4. For spray combustion in the back-step flow, an oscillation of droplet evaporation rate is also observed in addition to the oscillations in pressure, heat release rate, streamwise velocity and the integrand of the local Rayleigh Index. The difference in the initial droplet diameter hardly affects the pressure oscillation mode, but strongly affects the intensity of the pressure oscillation, and the intensity of the pressure oscillation becomes the maximum for a specific initial droplet diameter. This arises from the difference in the initial droplet diameter causing a difference in the droplet evaporation rate, which alters the relationship between the oscillations of the heat release rate and pressure near the dump plane.
5. For gas combustion in the channel flow, the pressure oscillation strongly affects the flashback characteristics such as flashback speed and heat transfer on the wall, and increases the mean flashback speed. This is because the acceleration of the flashback speed due to the pressure oscillation is greater than its deceleration. This fact indicates that the combustion instability, which often generates a large pressure oscillations in combustors, increases the risk of flashback.

5.2 Suggestions for future research

Conducting research into the following areas could extend the progress made in the current study.

1. In Chapter 2, droplet evaporation and combustion were investigated in various conditions using DNS with laminar flow field and flame conditions. For a further understanding of droplet evaporation in an actual combustor, it is important to investigate the interactions between droplet evaporation and a turbulent flame including phenomena such as the propagation and extinctions of the flame.
2. In Chapter 3, the effect of initial droplet diameter on combustion instability was investigated using LES, and it was shown that the intensity of the combustion instability became largest for a specific initial droplet diameter. However, LES were performed only in the conditions in which combustion instability was clearly excited. Therefore, the critical conditions that trigger combustion instability remain unclear. Further investigations focusing on the transitions from stable to unstable combustion are essential for predicting and controlling combustion instability. In addition, the geometry of combustor was limited to a simple back-step flow; this meant that a number of factors important in actual combustors, such as swirling flow and interactions between multiple burners, were not discussed. Numerical simulations for complex geometries of actual combustors are important to support the development and design of combustors across industrial fields.
3. In Chapter 4, the effect of combustion instability on flashback characteristics was investigated using DNS by employing an artificial pressure oscillation. It was shown that the flashback speed and heat flux at the wall were strongly affected by combustion instability. However, only a few conditions were studied. To fully develop discussions around the effects of combustion instability on flashback characteristics requires further investigations for different fuels, equivalence ratios and pressure oscillations of different intensities and frequencies.